Optimization of Digital Coherent Transceivers for Optical Communication Systems

Pavel Skvortcov

Doctor of Philosophy

School of Engineering and Applied Science
Aston University

September 2020

Aston University

Optimization of Digital Coherent Transceivers for Optical Communication Systems

Pavel Skvortcov

Doctor of Philosophy

September 2020

Thesis Summary

Coherent transceivers are the key elements of fibre-optical communication systems enabling high-speed transmission. These transceivers utilize state-of-the-art electrical and optical components, digital signal processing (DSP), and advanced coded modulation (CM) schemes. This thesis focuses on transceiver performance optimization techniques — in particular, two aspects are covered.

The first aspect is related to transceiver impairments characterization and mitigation via application of advanced DSP techniques. Transceiver performance can be detrimentally affected by various imperfections in its optical and electrical components and, therefore, it is important to mitigate the impact of those imperfections. Two techniques for characterization and compensation of transceiver skews were proposed and investigated — calibration techniques based on the Gardner timing error detector and signal image spectrum measurement. Also, the impact of various transmitter in-phase/quadrature (IQ) impairments was considered — specifically, modulation impairments, skews, electrical IQ cross-talk and frequency response mismatch. Post-compensation based on advanced post-equalizer and multiple-input multiple-output (MIMO) pre-emphasis approaches were proposed and investigated.

The second aspect is related to application of advanced CM techniques and optimization of the signaling scheme. Conventional uniform signaling based on quadrature amplitude modulation (QAM) is a sub-optimal solution in terms of linear and nonlinear performance, and advanced signaling schemes can be used to improve the overall system performance. Finite-length probabilistic constellation shaping, specifically, sphere shaping architecture was considered and optimized for improved linear and nonlinear performance of the system. The performance of the system employing finite-length sphere shaping architecture was extensively studied in comparison with uniform signaling and infinite-length Maxwell–Boltzmann (MB) shaping. Optimal shaping regimes were identified for long-haul multi-span and extended-reach single-span transmission links.

Keywords: Coherent fibre-optical communication systems, digital signal processing, transceiver impairments mitigation, probabilistic constellation shaping, nonlinearities mitigation

Acknowledgements

First of all, I would like to express my sincere gratitude to my supervisor Prof. Wladek Forysiak for his continuous support, created opportunities and kind relationships throughout my Ph.D studies. Also, I would like to thank the head of Aston Institute of Photonic Technologies (AIPT) Prof. Sergei Turitsyn for giving me an opportunity to intern at AIPT prior the start of my Ph.D program and introducing me to my supervisor; and also my associate supervisor Dr. Paul Harper for general discussions on the topic of fibre-optical communications and providing guidance on thesis writing.

Among my colleagues at AIPT, I am especially grateful to my former colleague Dr. Christian Sànchez-Costa, who initially introduced to the field of digital signal processing (DSP) for fibre-optical communications and provided help and guidance at early stages of my Ph.D path. Also, I express my appreciation to Dr. Tingting Zhang and Dr. Thanh Tu Nguyen for valuable discussions and suggestions on DSP development.

I would like to thank Lumentum, UK for my studentship support and, especially, Dr. Robert Griffin and Dr. Donald Govan for their valuable suggestions and discussions on transceiver performance optimization topic. These discussions helped me to develop some ideas presented in this thesis.

I would like to thank Mitsubishi Electric Research Laboratories (MERL), USA for the opportunity to have an internship with them. That was a truly excellent opportunity to work with world-leading experts in the field, gain knowledge and produce new research ideas. My special gratitude goes to Dr. David Millar and Dr. Kieran Parsons for their kind patience, shared knowledge and thorough guidance. Under their supervision I discovered some new exciting topics related to advanced coded modulation and probabilistic constellation shaping. Significant part of this thesis is based on the work initially started at MERL.

Table of Contents

List of Abbreviations

1D   One-dimensional

2D   Two-dimensional

4D   Four-dimensional

ACO   Analog coherent optics

ADC   Analog-to-digital converter

AIR   Achievable information rate

ASE   Amplified spontaneous emission

ASK   Amplitude-shift keying

AWGN   Additive white Gaussian noise

BCH   Bose–Chaudhuri-–Hocquenghem

BER   Bit error ratio

BICM   Bit-interleaved coded modulation

BPS   Blind phase search

CCDM   Constrant-composition distribution matcher

CD   Chromatic dispersion

CMA   Constant modulus algorithm

CM   Coded modulation

CPR   Carrier phase recovery

CR   Carrier recovery

CTA   Clock tone amplitude

CUT   Channel-under-test

CW	Continuous wave
DAC	Digital-to-analog converter
DD	Decision directed
DGD	Differential group delay
DM	Distribution matcher
DP	Dual-polarization
DPSK	Differential phase-shift keying
DSCM	Digital sub-carrier multiplexing
DSP	Digital signal processing
EDFA	Erbium-doped fiber amplifier
ENOB	Effective number of bits
ESS	Enumerative sphere shaping
FD-TED	Frequency-domain timing error detector
FEC	Forward error correction
FFT	Fast Fourier transform
FIR	Finite-impulse response
FWM	Four-wave mixing
GMI	Generalized mutual information
GSOP	Gram-Schmidt orthogonalization procedure
GVD	Group-velocity dispersion
HCSS	Huffman-coded sphere shaping
HD	Hard-decision
IM-DD	Intensity modulation with direct-detection
InP	Indium phosphide
IQ	In-phase/quadrature
ISI	Inter-symbol interference

LDPC	Low-density parity-check
LiNbO$_3$	Lithium niobate
LLR	Log-likelihood ratio
LMS	Least mean squares
LO	Local oscillator
LUT	Look-up table
MB	Maxwell–Boltzmann
MI	Mutual information
MIMO	Multiple-input multiple-output
ML	Maximum likelihood
MPDM	Multiset-partition distribution matcher
MSE	Mean squared error
MZM	Mach-Zehnder modulator
nGMI	Normalized generalized mutual information
OSA	Optical spectrum analyzer
OSNR	Optical signal-to-noise ratio
PAM	Pulse amplitude modulation
PAS	Probabilistic amplitude shaping
PBS	Polarization beam splitter
PMD	Polarization mode dispersion
PMF	Probability mass function
PSK	Phase-shift keying
QAM	Quadrature amplitude modulation
QPSK	Quadrature phase-shift keying
RC	Raised cosine
RF	Radio frequency

ROSNR	Required optical signal-to-noise ratio
RRC	Root-raised cosine
RV	Real-valued
SDM	Spatial-division multiplexing
SD	Soft-decision
SiP	Silicon photonics
SMF	Single-mode fiber
SM	Shell mapping
SNR	Signal-to-noise ratio
SOA	Semiconductor optical amplifier
SOP	State of polarization
SPM	Self-phase modulation
SSFM	Split-step Fourier method
SSMF	Standard single-mode fiber
TED	Timing error detector
TIA	Transimpedance amplifier
VCO	Voltage control oscillator
VOA	Variable optical attenuator
WDM	Wavelength-division multiplexing
WL	Widely linear
WSS	Wavelength-selective switch
XPM	Cross-phase modulation
XY	x-polarization/y-polarization

List of Figures

List of Tables

Chapter 1

Introduction

1.1 Background

Nowadays, fibre-optical communication systems form the backbone of the internet — over 95 % of all internet data is transmitted via an optical fibre and developments in fibre-optical technologies underpins the rapid growth of internet traffic all over the world. This growth is driven by a continuously emerging market of digital services and applications — internet of things, mobile devices and services, cloud storage and computing, high-definition video and audio content generate the internet traffic and stimulate its growth.

Some research studies suggest that the global data traffic increases with an average rate of 45% per year [1], [2]. According to the latest Cisco report, the average broadband and mobile connection speeds for customers are going to triple between 2018 and 2023 worldwide [3]. This growth has to be supported by advancements in backbone networks.

In general, there are two main paths to increase the overall throughput of fibre-optical communication systems. One path is via increasing the available bandwidth of the fibre and deploying more channels using wavelength-division multiplexing (WDM) and spatial-division multiplexing (SDM) technologies. The major development in WDM is associated with facilitation of advanced wide-band amplification techniques, which allow to broaden the operational optical bandwidth of single-mode fibers (SMF) [4]–[6]. The recent developments in SDM (i.e. multi-mode and multi-core fibers, as well as related amplification techniques and components) also pave the way for increasing the bandwidth of the fibre and, hence, the overall throughput per fibre in next-generation systems [7]–[9].

Concurrently, the system throughput can be improved by utilizing the available bandwidth of the fibre more efficiently — i.e. by increasing data rates per channel. The main focus in this direction is associated with the development of high-speed transceivers employing

the most advanced modulation and coding techniques, as well as digital signal processing (DSP). Today, transceivers employing coherent technology supported by high-speed DSP are a de-facto standard for long-haul and metro area transmission systems. The latter is in the scope of this Thesis.

Transceiver Technologies

In the mid-90s, when the low-loss fibers and WDM technology were already commercially available, transceivers employed intensity modulation with direct-detection (IM-DD) and were able to deliver the data rate of 2.5 Gb/s per optical channel. Within the next decade, transceivers data rates evolved to 10 Gb/s using IM-DD [10] followed by 40 Gb/s with differential phase-shift keying (DPSK) [11]. However, for data rates beyond 10 Gb/s those systems became very sensitive to some fibre impairments, such as chromatic dispersion (CD) and polarization mode dispersion (PMD), and therefore were unsuccessful in practical applications.

In the last decade, coherent detection has been a key enabling technology for high-throughput optical fiber communication systems. The coherent technology allows utilization of all four dimensions of the optical field for modulation (namely, amplitude, phase and polarization) and subsequent compensation of transmission impairments (e.g. CD and PMD). Initially, the adoption of coherent technology with high-speed DSP provided an immediate four-fold improvement in spectral efficiency compared to IM-DD systems [12]. The first coherent 40 Gb/s transmission systems using dual-polarization (DP) quadrature phase-shift keying (QPSK) [12] were therefore able to operate without significant increase in bandwidth compared with legacy 10 Gb/s IM-DD systems, while maintaining the same or even superior transmission reach. Another significant advantage was the simplification of transmission systems by removing the need for in-line dispersion compensation. DP-QPSK 100 Gb/s systems were subsequently introduced [13] and widely deployed in commercial long-haul networks [2]. In the presence of increasingly stringent bandwidth constraints, Nyquist pulse shaping and multi-level quadrature amplitude modulation (QAM) were employed in the next generations of coherent systems to increase spectral efficiency, and achieve the required growth in per-wavelength bit rates [14].

Nowadays, modern commercial coherent systems can operate at data rates of up to 800 Gb/s [15]. Systems operating at such high transmission rates are enabled by sophisticated DSP, and require state-of-the-art optical and electrical components, as well as advanced coded modulation (CM) schemes to deal with reduced sensitivity (e.g. in terms of tolerance to noise) due to multi-level modulation and high symbol rates. CM can be considered as the joint design of a signaling scheme, forward error correction (FEC) coding and multi-

level modulation. The key transceiver components are digital-to-analog converters (DACs), narrow linewidth lasers and high-speed optical modulators residing at the transmitter-side; 90° optical hybrids, high-speed photo-detectors and analog-to-digital converters (ADCs) residing at the receiver-side; application-specific integrated circuits (ASICs) designed for both transmitter and receiver DSP. To facilitate the widespread deployment of coherent technology, these transceiver components are typically packed into increasingly compact integrated transmitter and receiver assemblies, which are then can be used in highly compact energy efficient transceivers [16].

1.2 Thesis Outline

The work presented in this thesis primarily focuses on investigation of technologies and architectures for modern high-speed coherent transceivers, which can optimize the overall performance of the transmission system. In particular, two aspects of transceiver performance optimization are covered.

- The first part is related to characterization and compensation of various transceiver impairments by utilizing on-board DSP. When a system operates at very high data rates, it becomes highly susceptible to various impairments in optical and electrical components within the transceiver. Therefore, it is crucial to be able to characterize and compensate for those impairments.

  First, two techniques for transceiver skew calibration are proposed. These techniques offer good calibration accuracy and can be considered as low-complexity DSP-based solutions, which should be applied prior to normal operation of the transceiver. Then, an advanced receiver-based impairments mitigation technique using adaptive filters is proposed, which offers significant improvement to the overall transceiver tolerance to various impairments. A key advantage of receiver-based compensation is real-time operation, the potential to relax calibration, and to remove the need for periodic re-calibration due to drifting over temperature and aging. Finally, the application of an efficient low-complexity transceiver pre-emphasis technique based on estimation of the impairments using receiver-side adaptive filters is considered for the case of severe impairments.

- The second part is related to application of advanced CM techniques. The conventional uniform multi-level QAM signaling scheme represents sub-optimal solution in terms of both linear and nonlinear performance of the system. Hence, optimized signaling schemes can be used to improve the sensitivity of the system. Specifically,

practical finite-length probabilistic constellation shaping architectures are considered and tailored for improved linear and nonlinear performance of the system.

First, a conventional sphere shaping, which is theoretically optimal in terms of energy efficiency in the finite-length shaping regime, is considered as the signaling scheme for the application in multi-span long-haul and extended-reach single-span links. The impact of various shaping parameters on the nonlinear performance of the system is studied and optimal shaping parameters, which maximize the performance of the system in the considered links, are identified. Then, a Huffman-coded sphere shaping (HCSS) architecture, which closely approximates the spherical structure and offers efficient hardware implementation, is investigated for application in extended-reach single-span links and optimal shaping parameters are also identified. Overall, the advantage of finite-length shaping in terms of nonlinear performance over infinite-length shaping (optimal for a linear channel) for application in a nonlinear channel is demonstrated.

More detailed introductions including literature reviews for the topics under consideration will be given in the corresponding Chapters of the Thesis.

Thesis Structure

The thesis is organized as follows:

- **Chapter 2** gives an overview of modern coherent fibre-optical communication systems and related sub-systems: fibre-optical transmission links and key transmission impairments, a coherent transceiver and its key building blocks and related impairments, modulation formats and coding schemes, a DSP framework and metrics for system performance evaluation.

  This Chapter serves as the introduction to the main topics and results presented in the following Chapters.

- **Chapter 3** presents transceiver impairments characterization and mitigation techniques based on DSP. First, transceiver impairments characterization techniques are demonstrated: skew calibration based on the Gardner timing error detector and signal image suppression. Then, mitigation techniques for transmitter in-phase/quadrature (IQ) impairments are demonstrated: a receiver-side advanced post-equalizer for mitigation of transmitter modulation impairments, skews and electrical IQ cross-talk; and transmitter multiple-input multiple-output (MIMO) pre-emphasis for generalized frequency-dependent IQ imbalance.

The work in this Chapter is based on the original published material: [**P.1**], [**P.2**], [**P.3**], [**P.4**], [**P.5**].

- **Chapter 4** demonstrates the applications of probabilistic constellation techniques for improved linear and nonlinear performance of the transmission system. First, the concept of probabilistic amplitude shaping (PAS) is reviewed and a finite-length sphere shaping architecture with associated parameters and characteristics is introduced. Then, linear and nonlinear performance of the system employing the conventional sphere shaping architecture is extensively studied in long-haul multi-span and extended-reach single-span links via numerical simulations. Finally, the application of Huffman-coded sphere shaping (HCSS) was investigated experimentally in an extended-reach single-span link.

  The work in this Chapter is based on the original published material: [**P.6**], [**P.7**]. Also, original unpublished material is included.

- **Chapter 5** summarizes the work presented in the thesis, draws conclusions and gives an outlook for future work.

1.3   List of Publications

Publications included in the thesis

This thesis is based on the following publications (published as first author):

[**P.1**] **P. Skvortcov**, C. Sanchez-Costa, I. Phillips, and W. Forysiak, "Transmitter IQ skew calibration in coherent transceivers based on DSP," in *Proceedings of OSA Advanced Photonics Congress: Signal Processing in Photonic Communications (SPPCom)*, 2018

[**P.2**] **P. Skvortcov**, C. Sanchez-Costa, I. Phillips, and W. Forysiak, "Joint Tx and Rx skew calibration in coherent transceivers based on Rx-side DSP," in *Proceedings of IEEE Photonics Conference (IPC)*, 2018

[**P.3**] **P. Skvortcov**, C. Sanchez-Costa, I. Phillips, and W. Forysiak, "Receiver DSP highly tolerant to transmitter IQ impairments," in *Proceedings of Optical Fiber Communications Conference (OFC)*, 2019

[**P.4**] **P. Skvortcov**, I. Phillips, and W. Forysiak, "Transmitter I/Q cross-talk post-compensation using receiver DSP," in *Proceedings of 45th European Conference on Optical Communication (ECOC)*, 2019

[P.5] **P. Skvortcov**, I. Phillips, and W. Forysiak, "Transmitter frequency-dependent IQ imbalance characterization and pre-emphasis," in *Proceedings of OSA Advanced Photonics Congress: Signal Processing in Photonic Communications (SPPCom)*, 2018

[P.6] **P. Skvortcov**, I. Phillips, W. Forysiak, T. Koike-Akino, K. Kojima, K. Parsons, and D. S. Millar, "Nonlinearity tolerant LUT-based probabilistic shaping for extended-reach single-span links," *IEEE Photonics Technology Letters*, vol. 32, no. 16, pp. 967–970, 2020.

[P.7] **P. Skvortcov**, I. Phillips, W. Forysiak, T. Koike-Akino, K. Kojima, K. Parsons, and D. S. Millar, "Huffman-coded sphere shaping for extended-reach single-span links," *IEEE Journal of Journal of Selected Topics in Quantum Electronics* (available as pre-print: JSTQE Early Access and arXiv:2008.02313), 2021.

Publications not included in the thesis

The following publications were produced in co-authorship and do not directly contribute to the material presented in the thesis.

[C.1] M. A. Iqbal, M. Tan, L. Krzczanowicz, **P. Skvortcov**, A. El-Taher, I. D. Philips, W. Forysiak, J. D. Ania-Castañón, P. Harper, "Performance characterization of high gain, high output power and low noise cascaded broadband discrete Raman amplifiers," in *Proceedings of 19th International Conference on Transparent Optical Networks (ICTON)*, 2017

[C.2] L. Krzczanowicz, M. A. Iqbal, I. Phillips, M. Tan, **P. Skvortcov**, P. Harper, W. Forysiak, "Low Penalty, Dual Stage, Broadband Discrete Raman Amplifier for High Capacity WDM Metro Networks," in *Proceedings of Optical Fiber Communications Conference (OFC)*, 2018

[C.3] L. Krzczanowicz, M. A. Iqbal, I. Phillips, M. Tan, **P. Skvortcov**, P. Harper, W. Forysiak, "Low transmission penalty dual-stage broadband discrete Raman amplifier," *Optics Express*, vol. 26, no. 6, pp. 7091-7097, 2018

[C.4] T. Zhang, C. Sanchez, M. Al-Khateeb, A. Ali, M. Tan, **P. Skvortcov**, I. Phillips, S. Sygletos, A. Ellis, "224-Gb/s Carrier-Recovery-Free Doubly Differential 2ASK-8PSK for Short-Reach Optical Networks," *IEEE Photonics Technology Letters*, vol. 30, no. 16, pp. 1463 - 1466, 2018

[**C.**5] C. Sánchez, M. A. Z. A-Khateeb, T. Zhang, F. Ferreira, **P. Skvortcov**, J. L. Wei, S. Sygletos, A. D. Ellis, "Mitigation of Optical Fiber Nonlinearities in OFDM Systems Using FWM-Aware Constellation Modulation Technique," in *Proceedings of 44th European Conference on Optical Communication (ECOC)*, 2018

[**C.**6] T. Zhang, C. Sanchez, **P. Skvortcov**, F. Ferreira, S. Sygletos, I. Phillips, W. Forysiak, A. Ellis, "86-GBaud subcarrier multiplexed 16QAM signal generation using an electrical 90 degree hybrid and IQ mixers," *Optics Express*, vol. 27, no. 8, pp. 11819-11829, 2019

[**C.**7] M Abu-Romoh, **P. Skvortcov**, T. Zhang, T. Nguyen, I. Phillips, W. Forysiak, "Experimental study of the effect of integral nonlinearity in 8-bits resolution DACs on 256-QAM," in *Proceedings of OSA Advanced Photonics Congress: Signal Processing in Photonic Communications (SPPCom)*, 2020

Chapter 2

Modern Coherent Fibre-Optical Communication Systems: Fundamentals

This Chapter gives a brief overview of fundamentals and key concepts of modern coherent fibre-optical transmission systems. It serves as the introduction to the main topics and results presented in the following Chapters.

2.1 Introduction

Modern high-speed fiber-optical communication systems employ coherent detection in combination with advanced modulation formats and complex digital signal processing (DSP). Firstly, at the transmitter-side coherent technology allows the signal to be modulated into all orthogonal dimensions of the optical field (in-phase and quadrature components in two polarizations), which gives the freedom to use advanced modulation formats and coding schemes. Secondly, at the receiver-side coherent detection allows full reconstruction of the optical field, hence, various transmission and transceiver impairments can be efficiently compensated by the means of DSP.

In Section 2.2, the fibre-optical transmission link employing wavelength-division multiplexing is introduced and key transmission impairments are discussed. Then, in Section 2.3, the coherent transceiver concept is introduced and transceiver key building blocks and impairments are described, followed by the overview of modulation formats and coding schemes. Further, in Section 2.4, the DSP framework for coherent systems is briefly described. Finally, in Section 2.5, metrics for system performance evaluation are introduced.

2.2   Fibre-Optical Transmission Link

In this Section, the transmission link employing wavelength-division multiplexing is introduced and key transmission impairments are described.

2.2.1   Transmission System

A schematic of dispersion-uncompensated multi-span fibre-optical link is shown in Fig. 2.1. Signals from multiple transmitters (channels) at different wavelengths are combined through an optical multiplexer into a wavelength-division-multiplexed (WDM) signal and then transmitted over an optical fiber. After each span the WDM signal is optically amplified to compensate for the span loss (signal power attenuation). Typical span length is 70–100 km. At the receiver side, the WDM signal is demultiplexed and subsequently each channel is received independently. Note that, this is a simplified point-to-point link, while practical deployed systems may include optical routing (some WDM channels may be routed to a different destination).
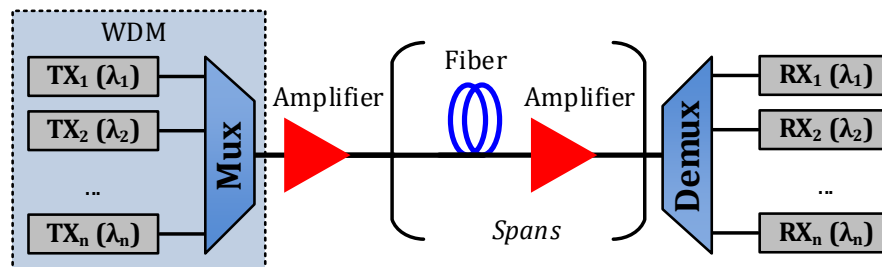
Fig. 2.1. Transmission system employing wavelength-division-multiplexing (WDM).

There are multiple technologies for optical amplification. The most widely used is erbium-doped fiber amplifiers (EDFAs) [17], [18], which operate in C-band or L-band of the optical fibre. Also, other available technologies are Raman amplifiers [19] and semiconductor optical amplifiers (SOAs) [20]. Raman amplifiers offer lower noise figure (due to the distributed nature of the amplification process) and wider/different operational bands (e.g. S-, C-, L-bands). SOAs offer operation in different operational bands and the possibility of compact integration within transceiver assemblies.

2.2.2 Transmission Impairments

For coherent optical communication systems, the optical single-mode fiber (SMF) serves as the medium for signal propagation. Various linear and nonlinear effects occur in the fibre, which can degrade the quality of the signal.

Fibre Attenuation

When the signal propagates through an optical fibre, it exhibits attenuation due to Rayleigh scattering and material absorption [21]. The evolution of signal power can be expressed as

$$P_s(z) = P_s(0) \cdot e^{-\alpha z}, \tag{2.1}$$

where α is the attenuation (loss) coefficient in linear units and z is the transmission distance.

Typically, the attenuation coefficient is specified in logarithmic units (dB/km) as

$$\alpha[\text{dB/km}] = -\frac{10}{z}\log\left(\frac{P_s(z)}{P_s(0)}\right) = 4.343\alpha[1/\text{km}]. \tag{2.2}$$

Fiber loss depends on the wavelength of propagating signal. For standard SMF, the loss is around 0.2 dB/km within the C-band.

Amplified Spontaneous Emission Noise

As mentioned previously, optical amplification is used to compensate for the fiber attenuation and recover the signal power after each transmission span. Optical amplifiers inherently produce amplified spontaneous emission (ASE) noise, which can be viewed as additive white Gaussian noise (AWGN) [22]. The key parameter of the optical amplifier, which quantifies the amount of generated ASE noise, is the noise figure. The noise power produced by the optical amplifier per transmission span can be expressed as [23]

$$P_{\text{ASE}}^{\text{span}} = (FG - 1)hf\Delta f, \tag{2.3}$$

where F is the noise figure (in linear units), G is the gain factor (in linear units), h is the Planck's constant, f is the operating optical frequency and Δf (also, denoted by BW_{ref}) is the reference bandwidth. Typically, the noise figure is specified in dB (in that case, it is denoted by NF). For the EDFA, the noise figure can vary within $4-6$ dB.

The degradation of signal-to-noise ratio (SNR) by the optical noise (ASE noise from amplifiers) is expressed in terms of optical SNR (OSNR). OSNR is defined as the ratio of the signal power to the optical noise power in a reference bandwidth of 12.5 GHz (equivalent

to 0.1 nm). For a transmission link consisting of multiple spans (with the same length), the OSNR can be expressed (in linear units) as

$$\text{OSNR} = \frac{P_s}{P_n} = \frac{P_s}{P_{\text{ASE}}^{\text{span}} \cdot N_{\text{span}}}, \tag{2.4}$$

where P_n is the total optical noise power accumulated during transmission (measured within 12.5 GHz reference bandwidth), which is the sum of ASE noise contributions from N_{span} spans.

Chromatic Dispersion

Chromatic dispersion is the phenomenon when the group-velocity of the optical field propagating through the fibre depends on its frequency [21], due to the corresponding frequency dependence of the fibre refractive index. In other words, different frequency components of the signal propagate at different speed. In the time domain it can be viewed as a pulse broadening.

The propagation constant of a mode in SMF is defined as

$$\beta(\omega) = n(\omega)\frac{\omega}{c}, \tag{2.5}$$

where ω is the angular frequency, $n(\omega)$ is the frequency-dependent refractive index, c is the speed of light in vacuum. Using Taylor series it can be represented as

$$\beta(\omega) = \beta_0 + \beta_1(\omega - \omega_0) + \frac{1}{2}\beta_2(\omega - \omega_0)^2 + \frac{1}{6}\beta_3(\omega - \omega_0)^3 + \ldots, \tag{2.6}$$

where ω_0 is the central frequency of the pulse. β_0 is the reference propagation constant, β_1 is the inverse group velocity, β_2 is responsible for group-velocity dispersion (GVD) and describes the dominant effect of pulse broadening, β_3 is responsible for the slope of dispersion and can be neglected when considering propagation of a single channel. Higher-order components can also be neglected.

The impact of chromatic dispersion on the signal can be represented by the frequency-domain transfer function as

$$H_{\text{CD}}(\omega, z) = e^{-i\frac{\beta_2}{2}\omega^2 z}, \tag{2.7}$$

where ω is the angular frequency of the optical field.

Typically, for optical fibers dispersion is specified in terms of dispersion parameter D at the fixed wavelength, which is given by

$$D = -\frac{2\pi c}{\lambda^2}\beta_2,$$ (2.8)

where λ is the wavelength. For SMF, D is around $16 - 17$ ps/nm/km in the C-band near 1550 nm.

Dispersion can be compensated optically using dispersion compensators (fibre based or fibre Brag gratings). However, for coherent transmission systems, dispersion is compensated electronically by the means of receiver-side DSP, which will be described in details in Section 2.4.

Polarization Mode Dispersion

The SMF fiber can support propagation of two degenerative modes in two orthogonal polarizations [21], [24]. In practical fibers, there is always some asymmetry in the core shape (i.e. not ideal cylindrical structure) along the fiber length due to manufacturing imperfections and external stress (e.g. bending, stretching, heating etc.). This may break the mode degeneracy, lead to mixing of the two polarization states and cause modal birefringence.

Modal birefringence can be described by the difference in refractive indexes for the modes polarized in x- and y-directions and expressed as

$$B_m = |n_x - n_y| = \frac{|\beta_x - \beta_y|}{\omega/c}.$$ (2.9)

As can be seen from Eq. 2.9, due to birefringence, propagation constants for the modes become different, hence, the light polarized in x- and y-directions propagates at different speeds. The axis with lower refractive index is referred to as the fast axis, while the axis with larger refractive index is referred to as the slow axis.

In an ideal case, when the birefringence is constant, the time shift between two polarizations, which is referred to as differential group delay (DGD), occurring during propagating in the optical fiber of length L can be expressed as

$$\Delta T = L|\beta_{1,x} - \beta_{1,y}|.$$ (2.10)

Due to random variations in fibre core shape and external stress, birefringence randomly varies along the length of the fiber. Also, a light launched in the fiber with a certain state of polarization (SOP) during propagation changes its SOP. Hence, in practical case, the fiber

may be considered as a composition of multiple birefringence sections. The expectation of the DGD resulting from multiple birefringence sections is refereed to as first-order polarization mode dispersion (PMD)

$$\sigma_T = \mathrm{E}[\Delta T] = D_p \sqrt{L}, \tag{2.11}$$

where $\mathrm{E}[\cdot]$ is the expectation operator, D_p is the PMD parameter expressed in ps/$\sqrt{\mathrm{km}}$. Note that average PMD scales with the square root of the transmission distance. The typical mean D_p value for SMF is around 0.1 ps/$\sqrt{\mathrm{km}}$.

The instantaneous PMD values can deviate from the average value due dynamic environmental perturbations. The variation of first-order PMD, which is represented by DGD, typically follow Maxwellian distribution over time and wavelength [24]. Fast variations may be caused by vibrations (in the order of krad/s) [25], [26], lightnings (in the order of Mrad/s) [27].

PMD can be a limiting factor in long-haul transmission for high symbol rate systems. In case of coherent transmission systems, PMD can also be compensated electronically by the means of receiver-side DSP.

Nonlinear Effects

Silica fibre is a nonlinear propagation medium — the response of the dielectric medium becomes nonlinear for electromagnetic fields with high intensity [21], [22]. The dominant nonlinear phenomenon which impacts the signal quality during transmission is the Kerr effect. Kerr effect can be described as the dependence of the refractive index on the instantaneous intensity (power) of the optical field. The dependence of the propagation constant on the power can be expressed as

$$\beta' = \beta + \gamma P, \tag{2.12}$$

where γ is the fiber nonlinear parameter. For SMF, the typical value is around 1.3 W^{-1}/km.

Due to power dependence of the propagation constant, nonlinear phase modulation of the optical field may be induced. It has the detrimental effect on the signal quality. The nonlinear phase shift can be expressed as

$$\phi_{NL} = \int_0^L (\beta'(z) - \beta) dz = \gamma \int_0^L P(z) dz. \tag{2.13}$$

Nonlinear interference can be categorized into intra-channel and inter-channel interactions (occurring in case of WDM transmission). Intra-channel nonlinearities include self-phase modulation (SPM), cross-phase modulation (XPM) and four-wave mixing (FWM). Inter-channel nonlinearities include XPM and FWM.

It is important to note that in long-haul dispersion uncompensated transmission, CD significantly decorrelates the nonlinearities in time – the nonlinear fiber interference can be seen as in-band AWGN noise [28]. The nonlinear noise power demonstrates a cubic dependence on the launch signal power, i.e. $P_{\mathrm{NLI}} \propto P_s^3$.

Nonlinear interference is the significant performance limiting factor for high-speed coherent communication systems. Despite its deterministic nature, the compensation of this impairments is very challenging in practical systems due to high-complexity of required DSP [29]–[31]. In Chapter 4, a signaling scheme, which is able to suppress nonlinear impairments, will be proposed and discussed.

2.3 Coherent Transceiver

In this Section, the concept of the coherent transceiver is introduced. First, the operation of the transmitter and receiver are described including main building components. Then, transceiver impairments are discussed, followed by the brief introduction on modulation formats and coding.

2.3.1 Transmitter

The transmitter diagram is shown in Fig. 2.2. Transmitter DSP is responsible for encoding binary data, mapping data into multi-dimensional symbols of a certain modulation format and preparing a digital base-band signal. A digital-to-analog converter (DAC) converts digital data into analog electrical driving signals. Electrical driving signals are pre-amplified by drivers and then passed to an optical dual-polarization (DP) in-phase/quadrature (IQ) modulator, where base-band electrical signal is modulated onto an optical carrier. Both amplitude and phase of the optical field are modulated in two orthogonal polarizations, which allows to utilize multi-level four-dimensional (4D) modulation formats.

The key element in electrical-to-optical conversion is a Mach-Zehnder modulator (MZM) shown in Fig. 2.3(a). Continuous wave (CW) optical field emitted from a narrow linewidth laser is split equally into two arms of the MZM, the phase of the optical field is modulated by an electrical driving signal in each arm, and then the optical field is recombined. When differential driving signal is applied introducing positive and negative phase shift of the same amplitude in two MZM arms (push-pull mode), chirp-free (in ideal case) amplitude modulation of the CW optical field can be achieved.

In order to modulate both in-phase and quadrature components of the optical field, a nested structure of MZMs is used (IQ modulator), where the output of the I branch is phase-
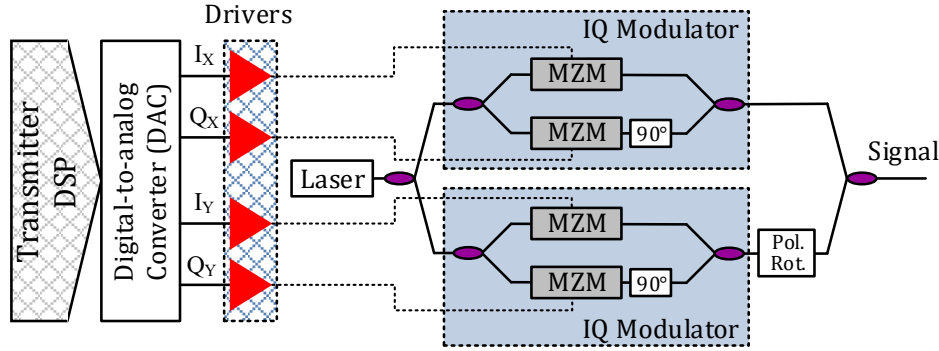
Fig. 2.2. Dual-polarization coherent transmitter.

(a) Push-pull MZM (b) Transfer function
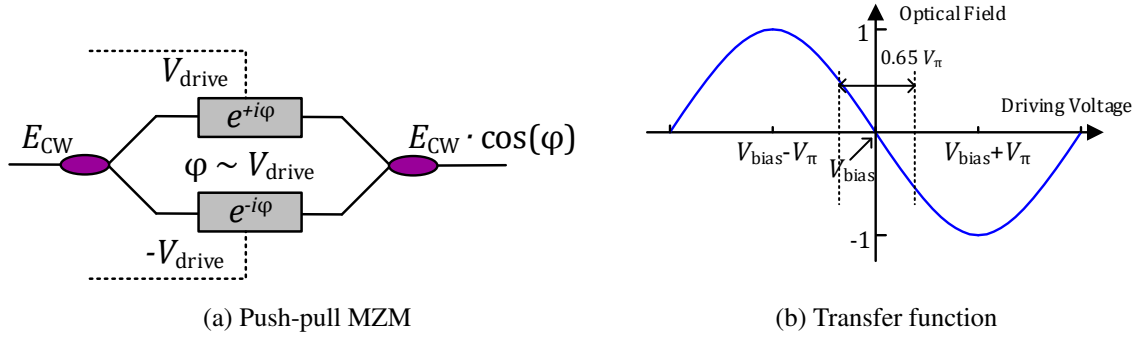
Fig. 2.3. Mach-Zehnder modulator (MZM).

shifted by 90° before I and Q branches are recombined. Dual-polarization (DP) signal is generated by using two IQ modulators, where the polarization state of the output of one branch is rotated into orthogonal state in relation to another branch.

The optical output in two orthogonal polarizations can be expressed as

$$
\begin{aligned}
S_x &\propto E_{\text{CW,x}} \cdot \left[\cos \frac{\pi(V_{\text{Ix}} + V_{\text{bias}})}{2V_\pi} + e^{i\frac{\pi}{2}} \cdot \cos \frac{\pi(V_{\text{Qx}} + V_{\text{bias}})}{2V_\pi} \right], \\
S_y &\propto E_{\text{CW,y}} \cdot \left[\cos \frac{\pi(V_{\text{Iy}} + V_{\text{bias}})}{2V_\pi} + e^{i\frac{\pi}{2}} \cdot \cos \frac{\pi(V_{\text{Qy}} + V_{\text{bias}})}{2V_\pi} \right],
\end{aligned}
\tag{2.14}
$$

where subscripts x and y denote orthogonal polarizations, $E_{\text{CW,x}}$ and $E_{\text{CW,y}}$ are the CW optical fields projected to each polarization, V_{Ix}, V_{Qx}, V_{Iy}, V_{Qy} are driving voltages corresponding to I and Q components in each polarization, V_π is the required voltage to achieve a relative phase difference of π between MZM arms, V_{bias} is the bias voltage for each MZM. Note that, as shown in Fig. 2.3(b), the transfer function of the MZM is sinusoidal. It is important to bias MZMs at the null point and operate within the linear part of the transfer function. For the

driving voltage range of $\sim 0.65V_\pi$, the transfer function can be considered well approximated by the linear shape (the deviation is negligible).

Modulator platforms

There are three main modulator platforms: lithium niobate (LiNbO$_3$), indium phosphide (InP) and silicon photonics (SiP) [32]. Each material uses different physical effects to enable phase modulation — LiNbO$_3$ modulators are based on electro-optic (Pockel's) effect, InP modulators are primarily based on quantum-confined Stark effect and SiP modulators are based on carrier depletion. LiNbO$_3$ was been widely used in previous generations of coherent systems. While it provides the great optical performance, long-length MZMs are required to achieve reasonably low driving voltage levels and power consumption, which makes it not suitable for modern highly compact transceivers. In contrast, InP [33] and SiP [34] technologies offer compact size and low drive voltage (which leads to power consumption reduction), as well as the possibility for high-density photonic integration with other active and passive optical components [35], [36]. Thus, it enables highly compact transceiver form-factors (e.g. CFP2 [37], [38]).

2.3.2   Receiver

Modern coherent receivers are based on intradyne reception, when the signal is down-shifted from the carrier to the base-band (but not precisely) — the incoming signal is interfered with a free-running local oscillator (LO) laser, which is tuned to a frequency close to the carrier of the signal [39]. Since the polarization of the incoming signal is arbitrary, a DP coherent receiver is used as illustrated in Fig. 2.4.
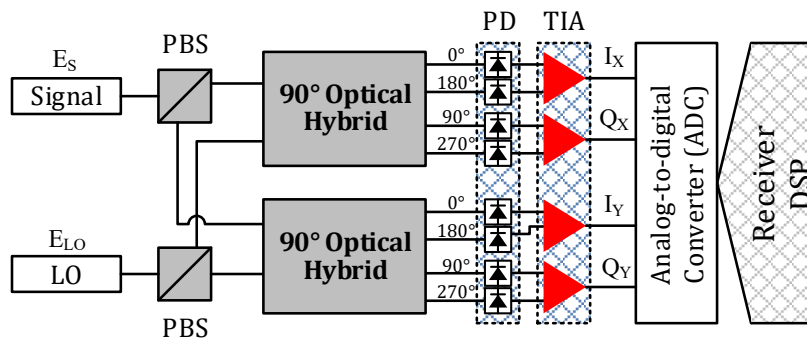
Fig. 2.4. Dual-polarization coherent receiver.

In the optical part, both an incoming signal and a local oscillator (LO) are split into two orthogonal polarizations by polarization beam splitters (PBSs) and then passed into

90° optical hybrids. Within the optical hybrid the signal is coupled with LO, such that at the outputs we have the sum of the signal optical field with LO phase-shifted by 0°, 180°, 90°, 270°. Then, the optical signals are detected by the photodiodes, where the beating of the signal and LO occurs. Photodiodes are paired into a balanced architecture — each two outputs (which correspond to the LO components with 180° phase difference) are fed to differential transimpedance amplifiers (TIAs) where the common mode (individual optical field intensities) is rejected and only the differential component (doubled beat signal) is amplified [40]. Balanced detection provides improved power dynamic range compared to single-ended detection.

The pre-amplified electrical signals corresponding to I and Q components in both orthogonal polarizations can be expressed as

$$
\begin{aligned}
V_{\text{Ix}} &\propto |E_{\text{S,x}} + E_{\text{LO,x}}|^2 - |E_{\text{S,x}} - E_{\text{LO,x}}|^2 = 4 \cdot \text{Re}\{E_{\text{S,x}} E_{\text{LO,x}}^*\}, \\
V_{\text{Qx}} &\propto |E_{\text{S,x}} + iE_{\text{LO,x}}|^2 - |E_{\text{S,x}} - iE_{\text{LO,x}}|^2 = 4 \cdot \text{Im}\{E_{\text{S,x}} E_{\text{LO,x}}^*\}, \\
V_{\text{Iy}} &\propto |E_{\text{S,y}} + E_{\text{LO,y}}|^2 - |E_{\text{S,y}} - E_{\text{LO,y}}|^2 = 4 \cdot \text{Re}\{E_{\text{S,y}} E_{\text{LO,y}}^*\}, \\
V_{\text{Qy}} &\propto |E_{\text{S,y}} + iE_{\text{LO,y}}|^2 - |E_{\text{S,y}} - iE_{\text{LO,y}}|^2 = 4 \cdot \text{Im}\{E_{\text{S,y}} E_{\text{LO,y}}^*\},
\end{aligned}
\tag{2.15}
$$

where $E_{\text{S,x}}$, $E_{\text{S,y}}$ and $E_{\text{LO,x}}$, $E_{\text{LO,y}}$ denote signal and local oscillator optical fields in each polarization, respectively. Note that by using the balanced architecture, direct-detected terms (individual optical field intensities) are cancelled and amplitudes of beat terms are doubled.

The coherent receiver gives access to the full optical field (i.e. phase and amplitude in two orthogonal polarizations). Hence, multi-level 4D modulation formats can be detected. Also, it provides frequency selectivity and increased sensitivity (low signal power can be compensated by the high power of the local oscillator).

Finally, the electrical signals are sampled and digitized by an analog-to-digital converter (ADC) and then the digital signal is passed to the receiver-side DSP, which is responsible for linear transmission impairments compensation and recovery of transmitted information.

2.3.3 Transceiver Impairments

Bandwidth Limitation

The transceiver electrical components (DAC/ADC, driver amplifiers, modulator, photodiodes, TIAs) inherently have a bandwidth limitation (frequency response roll-off), which can significantly degrade the performance of the transceiver [41], [42]. The bandwidth limitation is one of the key design factors which define the maximum symbol rate the system can operate at.

Transceiver bandwidth limitation can be compensated by the means of DSP [43]. Note that it is especially important to compensate for transmitter bandwidth limitation, since after transmission through a noisy channel the noise for high-frequency signal components may be enhanced within receiver DSP [44].

Transceiver Noise Floor

A transceiver noise floor is one of the main limitations for high-order modulation and high baud-rate systems. Various noise sources from the transmitter and receiver components can degrade the overall quality of the signal. The quantinization noise of DAC and ADC is one of the main noise sources [45], [46]. Both DAC and ADC have limited number of resolution bits, which results in quantization noise floor represented by the effective number of bits (ENOB) [46]. Additionally, practical DACs and ADCs impose further ENOB degradation due to other noise sources (clock jitter, thermal noise, integral nonlinearity etc.) in combination with bandwidth limitation. Note that ENOB is frequency-dependent (mainly, due to jitter) and may be significantly decreased at high symbol rates.

Other noise sources are driver amplifiers and TIAs, which inherently have noise figures (typically, frequency-dependent due to bandwidth limitation) and introduce electrical noise; photodiodes, which introduce shot and thermal noise. Also, transmitter may include integrated optical amplifiers (e.g. SOAs) to compensate for insertion loss of MZMs, which introduce optical ASE noise [47].

The impact of the various transceiver noise sources can be expressed in terms of transceiver signal-to-noise ratio (SNR) as

$$\frac{1}{\text{SNR}_{\text{Trx}}} = \underbrace{\frac{1}{\text{SNR}_{\text{DAC}}} + \frac{1}{\text{SNR}_{\text{Driver}}} + \frac{1}{\text{SNR}_{\text{SOA}}}}_{1/\text{SNR}_{\text{Tx}}} + \underbrace{\frac{1}{\text{SNR}_{\text{PD}}} + \frac{1}{\text{SNR}_{\text{TIA}}} + \frac{1}{\text{SNR}_{\text{ADC}}}}_{1/\text{SNR}_{\text{Rx}}}, \quad (2.16)$$

where each term represents the SNR degradation resulting from a specific transceiver component.

It is challenging to maintain high transceiver SNR (more than 20 dB) for systems operating at baud-rates exceeding 64 GBd [48]. Limited transceiver SNR sets the upper bound on system performance and introduces significant implementation penalties [49]. Fig. 2.5 demonstrates the total received SNR as a function of OSNR under the impact of limited transceiver SNR (SNR degradation due to fiber nonlinearities is neglected), which
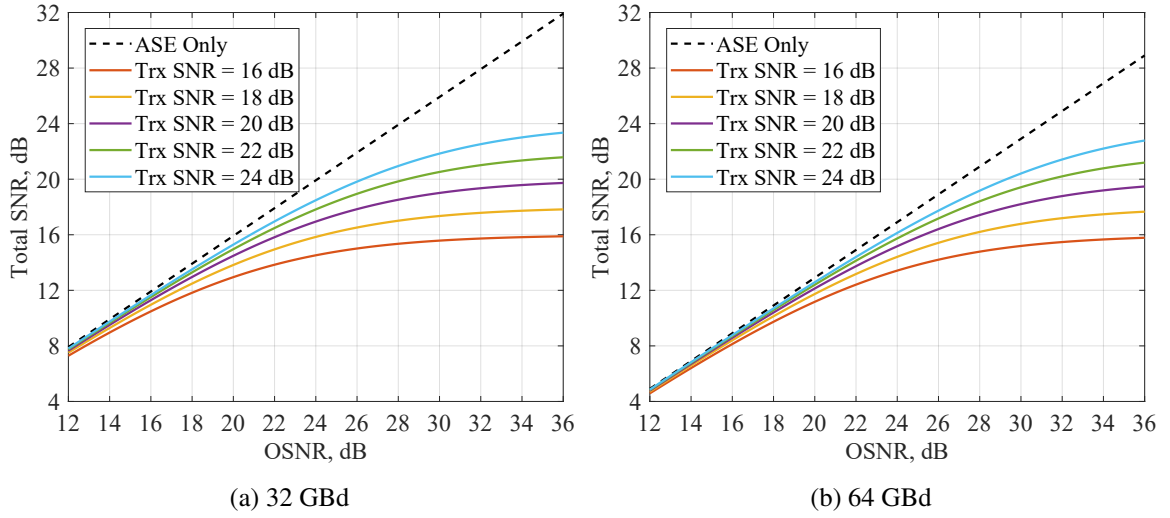
(a) 32 GBd   (b) 64 GBd

Fig. 2.5. Total SNR vs. OSNR for various limited transceiver SNR levels: (a) 32 GBd operation, (b) 64 GBd operation

can be calculated according to

$$\frac{1}{\text{SNR}_{\text{Total}}} = \frac{1}{\text{OSNR} \cdot \frac{\text{BW}_{\text{ref}}}{\text{BW}_{\text{sig}}}} + \frac{1}{\text{SNR}_{\text{Trx}}}, \tag{2.17}$$

where $\text{BW}_{\text{ref}} = 12.5$ GHz and BW_{sig} is the signal bandwidth. The implementation penalty can be described as the difference in terms of required OSNR to achieve a certain total SNR level between the ideal case (without additional transceiver SNR) and the impaired case (with transceiver SNR). Under the impact of lower transceiver SNR, stronger divergence from the ideal case can be seen and therefore implementation penalties are increased. Also, note that limited transceiver SNR sets the upper limit for the total SNR.

Skews

Another significant transceiver impairment is the skews. Skew is a timing missalignment (i.e. group delay) between different signal components/tributaries (e.g. I/Q quadratures and x/y polarizations of the signal). Skew may arise from different sampling phases of DAC/ADC, different electrical and optical path lengths, unmatched transfer functions of the components. Large uncompensated skews may significantly degrade the system performance. It is important to carefully compensate for both transmitter and receiver skews, especially for systems operation at high symbol rates.

Detailed system characterization of the system performance impaired by the skews will be discussed in Chapter 3.

Nonlinearities

Various nonlinear effects within transceiver components can deteriorate the system performance. Electrical components (driver amplifiers, TIAs, DACs and ADCs) may have nonlinear transfer functions [45], [50]. The optical modulator may also have a nonlinear electro-optical transfer function – e.g. MZM has inherently a sinusoidal transfer function. Also, imbalance between MZM arms and material nonlinearities may introduce chirp [51], which leads to nonlinear electrical-to-optical conversion. Concatenation of nonlinear transfer functions with bandwidth limitation causes nonlinear distortion of the signal with memory (the signal output depends not only on current input value, but also the previous values), which makes compensation of such effects very challenging [52].

IQ Impairments

IQ impairments may be present at both transmitter and receiver sides. At the transmitter side, modulation impairments in the form of non-ideal biasing of MZMs, imperfect phase shift (non 90°) between I and Q of the MZM branches, gain imbalance or different losses between RF driving signals may result in the distorted constellation diagram of the transmitted signal. Electrical IQ cross-talk may occur within MZMs due to the proximity of RF paths in highly compact photonic integrated circuits. Finite extinction ratio of MZMs (resulting from imperfect splitting ratios and different loses within MZMs) also may results in severe distortion of the signal constellation.

At the receiver-side, IQ imbalance (non-orthogonality and gain mismatch of I and Q components) may occur from 90° hybrid imperfections and mismatched responsivities of the photodetectors and gain factors of TIAs [53].

2.3.4   Modulation Formats and Coding

Modulation format is formed by the alphabet of possible transmission symbols. Each symbol represents the amplitude, phase and polarization state of the optical field [54]. By combining amplitude and phase modulation complex two-dimensional (2D) modulation formats can be constructed, which are represented by a set of points on a complex plane (i.e. constellation). By using polarization diversity of the optical field, four-dimensional (4D) modulation formats can be constructed (e.g. as the product of two 2D constellations).

The modulation order is given by the size of the alphabet (i.e. number of constellation points) and denoted by M. It is usually chosen to be a power of 2. The number of information bits, which can be encoded into each symbol from the alphabet of the modulation format, is

given by $m = \log_2 M$. By employing high-order modulation formats the spectral efficiency (i.e. the number of bits per transmitted symbol) of transmitted signal can be increased.

Modern coherent systems are based on M-ary quadrature amplitude modulation (M-QAM) and quadrature phase-shift keying (QPSK). For these modulation formats, constellation points are located equidistantly on a complex plane (where coordinates are represented by I and Q components of the signal). Using these modulation formats, the signal can be modulated into a single polarization (2D). 4D counterpart based on M-QAM is denoted as dual-polarization (DP) M-QAM. Note that, formally, for DP M-QAM the modulation order is $M' = M^2$.

(a) QPSK (4-QAM)

(b) 16-QAM
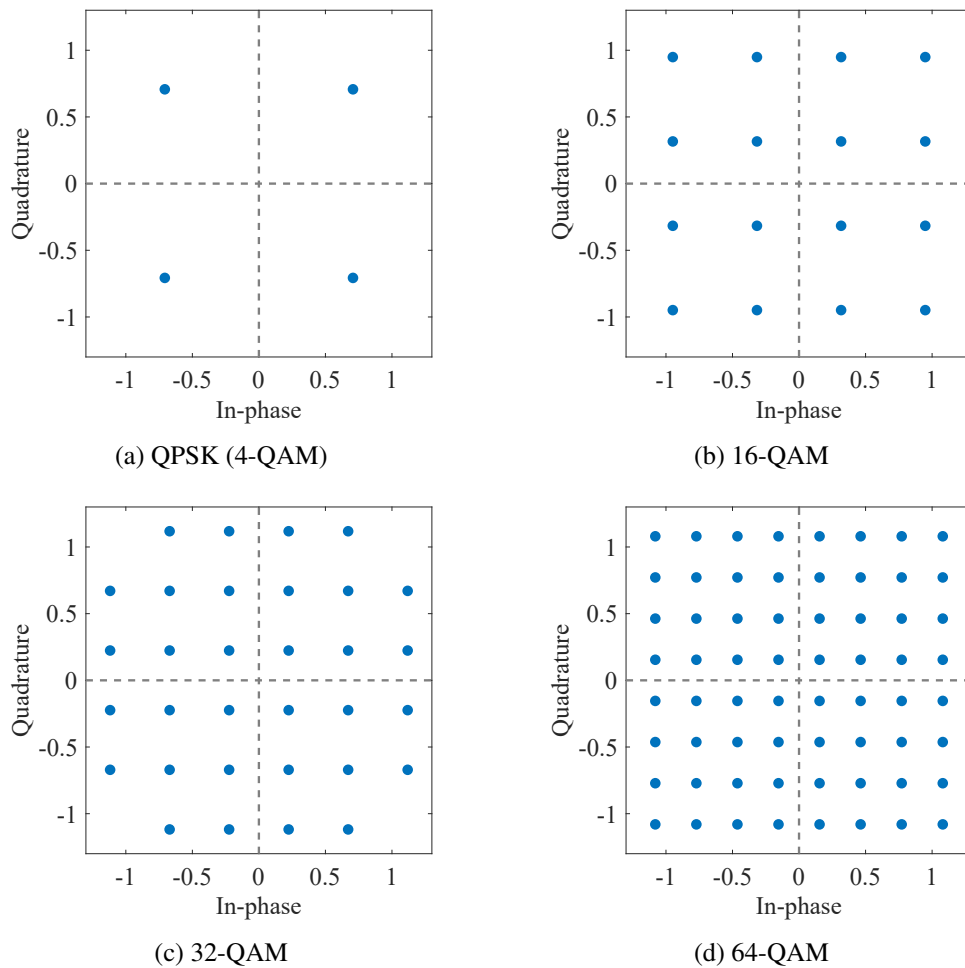
(c) 32-QAM

(d) 64-QAM

Fig. 2.6. Constellation diagrams of M-QAM formats.

Fig.2.6 (a)–(d) illustrate constellation diagrams for QPSK (can be considered as 4-QAM), 16-QAM, 32-QAM, 64-QAM formats. Note that each format is normalized to the unity power (assuming uniform probability distribution of constellation points). It can be seen that for high-order QAM formats the Euclidean distance between constellation points is reduced.

Therefore, high-order formats, while offering improved spectral efficiency, are inherently subject to reduced tolerance to noise and require higher received SNRs.

Coded Modulation

Coded modulation (CM) is the combined design of a signaling scheme, error correction coding and high-order modulation. Modern optical communication systems employ forward error correction (FEC) to increase the sensitivity of the system. The encoder at the transmitter adds redundancy (overhead) to the transmitted data, such that the decoder at the receiver is able to correct the errors occurring during transmission over a noisy fibre-optical channel.

There are several approaches for CM implementation [55]. One solution is to combine FEC with the mapping operation of information bits into modulated symbols into a single stage. This approach requires the design of non-binary FEC [56], [57]. In modern practical coherent systems, typically, binary FEC coding is adopted due to lower implementation complexity. In that case, the information bits are encoded using binary FEC and the memory-less mapping of encoded bits into symbols is performed separately. Nowadays, the most common CM approach employing binary FEC is bit-interleaved CM (BICM) [58], where bits interleaving stage may be inserted before the mapping. The important consideration for BICM schemes is the choice of the mapping rule for converting bits to symbols. Typically, binary Gray coding is used, which provides minimum Hamming distance for adjacent constellation points [59].

In general, FEC codes can be divided into two categories based on the type of information used for decoding at the receiver. For hard-decision (HD) decoding, the received symbols are demapped directly into bits based on a certain decision rule (boundaries) and then those bits are decoded. For soft-decision (SD) decoding, the soft information is extracted from the symbols in the form of bit-likelihoods (reliabilities) and then used for decoding. Originally, HD-FEC was adopted in optical communication systems [60]. Then, SD-FEC took over in coherent systems applications offering higher coding gain and reduced gap to Shannon limit [61]. Note that most modern practical systems may use concatenation of both SD-FEC (as the inner encoder/decoder) and HD-FEC (as the outer encoder/decoder) [62] to achieve the desired performance and implementation complexity.

Constellation Shaping

In addition to the FEC coding, modern CM schemes may employ advanced signaling schemes — i.e. constellation shaping, which offers additional performance gain (i.e. shaping gain) [63]. Constellation shaping can be considered as the optimization of transmitted symbols distribution (in terms of location or probability of symbols in multi-dimensional space), such

that the transmitted signal has the optimal energy efficiency for a given transmission data rate.

There are several techniques which refer to constellation shaping [64]. Two main approaches are geometric shaping and probabilistic shaping. Geometric shaping is based on the optimization of the location of constellation points on a complex plane (resulting in non-QAM constellation), where each constellation point is equiprobable [65], [66]. Probabilistic shaping is based on the optimization of the probability distribution of constellation points for standard QAM constellations [67], [68]. Probabilistic shaping is in the scope of this Thesis.
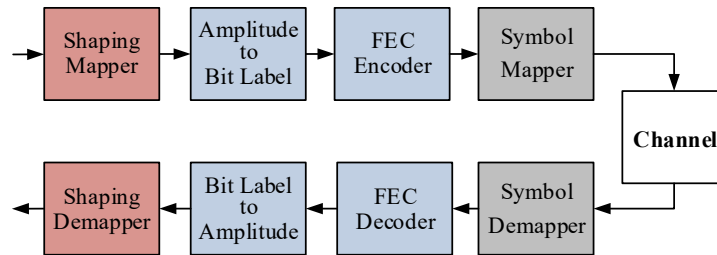
Fig. 2.7. Probabilistic amplitude shaping (PAS). Reverse concatenation of shaping stage and FEC coding.

The commonly adopted architecture for implementing probabilistic shaping into BICM systems is probabilistic amplitude shaping (PAS) [68]. This architecture is based on a reverse concatenation of the shaping stage and FEC coding (i.e. shaping precedes FEC coding) (see Fig. 2.7). The key component of the PAS architecture is the shaping mapper which maps the stream of uniform input bits into unsigned probabilistically shaped amplitudes. Systematic FEC coding is performed on the bit-labels of the shaped amplitudes and parity bits are added as signs of amplitudes. Signed amplitudes are then concatenated into symbols of a QAM format. In such a structure the transmission rate can be adapted by changing the amplitude shaping rate, while keeping the FEC code rate fixed.

More detailed overview of probabilistic constellation shaping, shaping algorithms as well as its implementations for coherent optical systems will be given in Chapter 4.

2.4   Digital Signal Processing Framework

In this Section, the overview of the generic structure of the DSP framework for coherent optical communication systems is given. This framework was developed and used to produce the key results presented in Chapters 3 and 4.

2.4.1   Transmitter
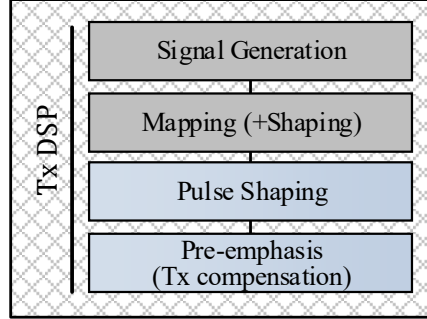
Fig. 2.8. Transmitter DSP chain.

Fig. 2.8 shows the DSP chain at the transmitter-side. In general, transmitter DSP is responsible for coding and mapping input binary data into symbols of a certain modulation format and signaling scheme (e.g. uniform or non-uniform signaling); as well as performing pulse shaping (e.g. Nyquist shaping) and digital pre-emphasis (transmitter impairments pre-compensation).

Throughout the work presented in this thesis, the randomly generated signal was used for system performance evaluation (Monte-Carlo approach). The signal was generated directly on the symbol-level skipping the FEC coding and bit-to-symbol mapping.

The detailed overview of probabilistic constellation shaping framework will be given in Chapter 4.

Pulse Shaping

The pulse shaping is employed to limit the occupied signal bandwidth and improve the spectral efficiency [69]–[71]. A raised-cosine (RC) pulse shaping can be employed for that purpose, which has the property of Nyquist zero inter-symbol interference (ISI). The frequency characteristic of RC pulse shaping is given by

$$
H_{\mathrm{RC}}(f) = \begin{cases} T, & |f| \le \frac{1-\beta}{2T}, \\ \frac{T}{2}\left\{1 + \cos\left[\frac{\pi T}{\beta}\left(|f| + \frac{1-\beta}{2T}\right)\right]\right\}, & \frac{1-\beta}{2T} \le |f| \le \frac{1+\beta}{2T}, \\ 0, & |f| > \frac{1+\beta}{2T}. \end{cases} \tag{2.18}
$$

where T is the symbol duration ($T = 1/f_b$, where f_b is the Nyquist frequency), β is the roll-off factor, which can be used to control the bandwidth occupation of the signal (within f_b and $2f_b$).

Typically, root-raised-cosine (RRC) pulse shaping filtering (which can be expressed as the square root of RC pulse shaping: $H_{\text{RRC}}(f) = \sqrt{H_{\text{RC}}(f)}$) is applied at the transmitter-side DSP. The filtering stage can be implemented either in time-domain (e.g. using a finite-impulse response (FIR) filter) or frequency domain (e.g. using fast Fourier transform (FFT) based overlap-and-save method [72]).

Note that RCC filter does not satisfy Nyquist zero ISI. However, matched RRC filtering is used at the receiver-side, which in combination with transmitter-side RRC pulse shaping achieves the desired overall RC pulse shape. Splitting the RC filtering between transmitter and receiver maximizes the output signal SNR [59].

Transmitter Pre-emphasis

Digital pre-emphasis is applied at the transmitter to pre-compensate for linear transmitter impairments (e.g. bandwidth limitation and skews). Pre-emphasis allows to relax the requirements for specifications of tranceiver components and enables the transmission of high-order modulation formats at high-symbol rates.

Pre-emphasis can be achieved by the means of digital filtering of each signal component (I and Q components in both polarizations) within the transmitter DSP chain, hence, allowing compensation of bandwidth limitation of individual RF channels and skews between them. Throughout the work in this thesis the response of the pre-emphasis filter was based on zero-forcing approach (inverting the measured transmitter response). Optimality of this approach under the impact of ENOB was not taken into account [41], [43]. In the case of zero-forcing the pre-emphasis filter response can be expressed as

$$H_{\text{Pre-emph}}(f) = \frac{1}{H_{\text{BW}}(f)}, \qquad (2.19)$$

where $H_{\text{BW}}(f)$ is the measured frequency response of the transmitter.

Also, another important linear impairment, which can be compensated by the means of digital pre-emphasis is linear frequency-dependent IQ coupling (e.g. electrical IQ cross-talk within MZM). The pre-emphasis approach for compensation of frequency-dependent IQ coupling effect will be discussed in Chapter 3.

2.4.2 Receiver

The generic DSP chain at the receiver-side is demonstrated in Fig. 2.9. The receiver DSP is responsible for compensating the linear channel impairments (e.g. chromatic dispersion,
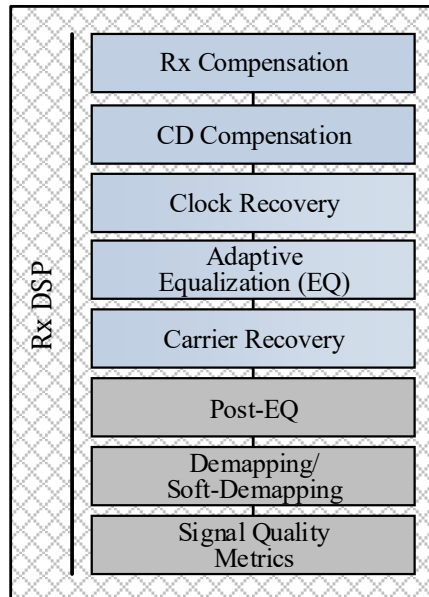
Fig. 2.9. Receiver DSP chain.

PMD, SOP) and also residual transceiver impairments (e.g. bandwidth limitation, skews, IQ imbalance).

An adaptive post-equalizer (which is responsible for compensation of residual transmitter impairments) will be introduced in Chapter 3. The overview of symbol demapping approaches and signal quality metrics used to evaluate the system performance throughout the thesis will be given in the next Section.

Receiver Compensation

The received signal may suffer from various impairments originating from the receiver front-end: IQ imbalance, skews between signal tributaries and bandwidth limitation. The receiver compensation stage is intended to compensate for these impairments.

An algorithm based on the Gram-Schmidt orthogonalization procedure (GSOP) can be employed to compensate for IQ imbalance and normalize the signal [53], [71]. For the purpose of bandwidth limitation and skews compensation, the same approach as for transmitter pre-emphasis can be used (i.e. sinverting the measured receiver response).

Dispersion Compensation

CD represents a static (time-invariant) linear impairment, which can be compensated by linear filtering with the inverse CD response [71]. The response of the ideal dispersion

compensation filter is given by (using Eq. 2.7)

$$H_{\text{CD}}^{\text{comp}}(\omega, z) = \frac{1}{H_{\text{CD}}(\omega, z)} = H_{\text{CD}}(\omega, -z). \tag{2.20}$$

The CD compensation filter represents an all-pass filter with quadratic phase response. However, since the signal is band-limited (in case of RRC pulse shaping), the filter all-pass characteristic is only required within the signal bandwidth. For the purpose of this work, an optimal CD compensation filter was designed in the time-domain using the least-squares approach [73], then filtering was performed in the frequency-domain.

Note that, in principle, receiver compensation filtering and matched filtering (not shown in Fig. 2.9 as a separate stage) can be combined with CD compensation into a single filtering stage.

Clock Recovery

The clocks at the transmitter DAC and receiver ADC side are not synchronized and operate asynchronously, hence, the clock needs to be recovered from the received signal. Clock recovery is performed to detect the clock and sampling phase from the signal and correct for the clock offset and sampling phase deviation.

There are multiple algorithms which can extract the clock information from the received sampled signal. In this thesis, the Gardner algorithm was employed to detect the sampling phase error from the complex envelope of the signal [74]. The frequency-domain Gardner sampling phase detector (alternatively, timing error detector) [75] is given by

$$\tau = \text{angle}\left[\sum_{k=0}^{N/2-1} X(k) \cdot X^*(k+N/2) \right], \tag{2.21}$$

where τ is the sampling phase error, which is given as the fraction of symbol period; $X(k)$ is the FFT of time-domain signal samples $x(i)$; N is the FFT size; angle$[\cdot]$ is the operator, which returns the angle of complex valued argument. It can be seen, that in the frequency-domain representation, the algorithm correlates the phase information of the frequency components above and below the Nyquist frequency. It is important to perform the clock recovery after CD compensation, since the CD distorts the phase information of the signal around the Nyquist frequency.

The clock offset and sampling phase can be compensated by the means of a digital interpolation (implemented in the form of fractional delay filter). In this work, the Lagrange interpolator in the form of FIR filter was used [76], [77].

Note that in the real-time system, the clock of the ADC can be adjusted by a voltage control oscillator (VCO), hence, the clock offset and sampling phase can be partially controlled in the analog domain and only fine compensation is required in the digital domain.

Adaptive Equalization

Adaptive equalization is employed to compensate for dynamic channel impairments (e.g. SOP rotation and PMD) and residual static impairments (including transceiver impairments). Since dual-polarization transmission is employed, 2×2 multiple-input multiple-output (MIMO) equalization structure, which consists of 4 FIR filters, is used [71]. 2×2 MIMO equalizer can be represented by a butterfly structure with two inputs (signal in X and Y polarizations before compensation) and two outputs (signal in X and Y polarizations after compensation) as illustrated in Fig. 2.10.
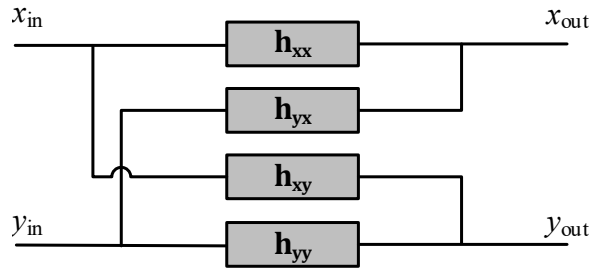
Fig. 2.10. 2x2 MIMO adaptive equalizer.

The widely adopted algorithm for FIR filter taps (coefficients) update is the least mean squares (LMS) algorithm, which represents stochastic gradient method [71], [72]. The LMS algorithm offers high stability and rapid convergence at reasonably low-complexity. The LMS algorithm updates the filter taps by calculating the instantaneous gradient, which is the derivative of the cost function with respect to the filter coefficients. The filter taps update is given by

$$\boldsymbol{h}(n+1) = \boldsymbol{h}(n) - \mu \nabla \boldsymbol{J}(n), \tag{2.22}$$

where $\boldsymbol{h}(n)$ is the filter tap vector at instant n, $\nabla \boldsymbol{J}(n)$ ($\nabla \boldsymbol{J} = \partial J / \partial \boldsymbol{h}(n)$) is the instantaneous gradient of the cost function, μ is the step-size of the update algorithm.

There are various cost functions, which can be used for LMS adaptation algorithm. The most commonly used approaches are based on the constant modulus algorithm (CMA) and decision directed (DD) algorithm. For the CMA the cost function is given by

$$\boldsymbol{J} = \mathrm{E}\left[(R - |x_{\mathrm{out}}(n)|^2)^2\right], \tag{2.23}$$

where R is the reference radius, $x_{\text{out}}(n)$ is the output signal value, $\text{E}[\cdot]$ denotes expectation operator. CMA is well suited for modulation formats with constant power symbols (e.g. QPSK) and also for initial pre-convergence for higher-order modulation formats. For DD-LMS algorithm the cost function is given by

$$\boldsymbol{J} = \text{E}\Big[(\text{D}[x_{\text{out}}(n)] - x_{\text{out}}(n))^2 \Big], \tag{2.24}$$

where $\text{D}[\cdot]$ denotes the symbol decision operator (e.g. decision can be based on minimal Euclidean distance). It is important to note that DD-LMS equalizer has to operate in conjunction with carrier recovery, which may introduce a decision and filter update feedback delay. Also, blind (i.e. when no prior knowledge of transmitted symbols is used) startup of DD-LMS may not be feasible. The typical approach is to start equalization from training mode (e.g. using pilots or training sequence) or blind CMA and then switch to blind DD-LMS operation. In the case of pilot-based (i.e. using known transmitted pilot symbols) or fully data-aided (i.e. using the prior knowledge of the whole transmitted signal) operation, the decided symbols in Eq. 2.24 are replaced by the known transmitted symbols.

The LMS algorithm can be generalized for the MIMO structure. After calculating the gradient of cost function, the equation for filter updates for DD-LMS 2×2 MIMO equalization can be expressed as

$$
\begin{aligned}
\boldsymbol{h}_{\text{xx}}(n+1) &= \boldsymbol{h}_{\text{xx}}(n) - \mu e_{\text{x}}(n)\boldsymbol{x}_{\text{in}}(n), \\
\boldsymbol{h}_{\text{yx}}(n+1) &= \boldsymbol{h}_{\text{yx}}(n) - \mu e_{\text{x}}(n)\boldsymbol{y}_{\text{in}}(n), \\
\boldsymbol{h}_{\text{xy}}(n+1) &= \boldsymbol{h}_{\text{xy}}(n) - \mu e_{\text{y}}(n)\boldsymbol{x}_{\text{in}}(n), \\
\boldsymbol{h}_{\text{yy}}(n+1) &= \boldsymbol{h}_{\text{yy}}(n) - \mu e_{\text{y}}(n)\boldsymbol{y}_{\text{in}}(n),
\end{aligned}
\tag{2.25}
$$

where $\boldsymbol{x}_{\text{in}}$ and $\boldsymbol{y}_{\text{in}}$ are the input signal vectors corresponding to x and y polarizations, e_{x} and e_{x} are DD error functions given by

$$
\begin{aligned}
e_{\text{x}}(n) &= \text{D}[x_{\text{out}}(n)] - x_{\text{out}}(n), \\
e_{\text{y}}(n) &= \text{D}[y_{\text{out}}(n)] - y_{\text{out}}(n),
\end{aligned}
\tag{2.26}
$$

where x_{out} and y_{out} are the filter outputs corresponding to x and y polarizations.

Carrier Recovery

As discussed previously, the coherent receiver uses intradyne detection using the free-running LO (i.e. transmitter and receiver lasers are not frequency and phase locked), hence, frequency and phase synchronization of the carrier should be performed by the means of DSP [78].

Throughout the thesis this DSP stage is refereed to as carrier recovery (CR) or carrier phase recovery (CPR).

The impact of the frequency offset and phase noise on the signal can be expressed as (continuous-time representation)

$$x'(t) = x(t) \cdot e^{i(2\pi\Delta f t + \phi(t))}, \tag{2.27}$$

where Δf is the frequency offset, $\phi(t)$ is the time-dependent phase noise. The phase noise evolution can be described by a Wiener process (random walk) and expressed as (discrete-time representation for sampled signal)

$$\phi(n+1) = \phi(n) + \Delta\phi(n), \tag{2.28}$$

where the phase noise $\Delta\phi$ has Gaussian distribution with variance $\sigma_\phi^2 = 2\pi\Delta\nu T$ (where $\Delta\nu$ is the combined linewidth of transmitter and receiver lasers).

There are various algorithms for frequency offset estimation and phase noise tracking. As for adaptive equalization, these algorithms can be classified into blind and pilot-based. Specific algorithms used in this thesis are described below.

For frequency offset estimation, two main approaches were used in this thesis. The first one is based on blind frequency estimation using the FFT of the signal raised to 4th-power (frequency domain 4th-power algorithm) [71], [79]. The estimated frequency offset using this algorithm is given by [80]

$$\widehat{\Delta f} = \frac{1}{4} \max_f |\text{FFT}[\boldsymbol{x}^{\circ 4}]|, \tag{2.29}$$

where $\text{FFT}[\cdot]$ is the FFT operator, which takes the time domain input vector as the argument; $\boldsymbol{x}$ is the signal input vector in time domain; $(\cdot)^{\circ 4}$ denotes element-wise 4th-power operation. Note that this method has been designed for M-PSK modulation (e.g. for QPSK, raising the signal to 4th-power removes the phase modulation), however, for higher-order modulation it may also provide satisfactory frequency offset estimation.

Similarly, the FFT-based approach can be used for pilot-based frequency offset estimation [81]. In that case the modulation can be removed by correlating the received symbols with transmitted ones. The frequency offset estimation can be expressed as [80]

$$\widehat{\Delta f} = \max_f |\text{FFT}[\boldsymbol{x} \odot \boldsymbol{a}^*]|, \tag{2.30}$$

where $\boldsymbol{a}$ is the pilot or training sequence symbols vector (aligned with corresponding received symbols), $\odot$ denotes symbol-wise multiplication. The accuracy and resolution of the frequency offset estimation can be improved by increasing the FFT block size and zero-padding the signal block (zero-padding in the time-domain is equivalent to interpolation of frequency components in frequency domain).

After frequency offset estimation and compensation, phase noise tracking was performed using the blind phase search (BPS) algorithm [82] or ideal fully-data aided phase estimation [78]. The BPS algorithm performs blind phase estimation by testing phase rotations (using the finite set of test phases) and minimizing the error function, which represents the sum of squared Euclidean distances between rotated received symbols and corresponding decided symbols over a block of received symbols. The error function can be expressed as

$$J(n, \phi_b) = \sum_{i=-N/2}^{N/2-1} |\mathrm{D}[x(n+i)e^{-i\phi_b}] - x(n+i)e^{-i\phi_b}|^2 , \qquad (2.31)$$

where ϕ_b are the test phases (typically, in the range from 0 to $\pi/2$), N is the length of the symbol block size. The estimated phase is given by the test phase which minimizes the cost function. It can be expressed as

$$\widehat{\phi}(n) = \min_{\phi_b} J(n, \phi_b) . \qquad (2.32)$$

The second stage employing maximum likelihood (ML) carrier phase estimation can be applied to refine the phase estimates given by the BPS algorithm [83].

For fully data-aided operation, the prior knowledge of the whole transmitted signal is used. In that case phase can be estimated as follows

$$\widehat{\phi}(n) = \mathrm{angle}\left[\sum_{i=-N/2}^{N/2-1} x(n+i)a^*(n+i) \right] , \qquad (2.33)$$

where N is the length of an averaging window (averaging is used to filter out the signal AWGN noise). Note that it is assumed that phase variations are relatively slow (constant within the time-frame of the averaging window). The length of averaging window should be adjusted in accordance with SNR operation range to achieve optimal phase tracking performance. Alternatively, the Wiener filter can be used for optimal phase detection [78].

2.5   Performance Metrics

In this Section, performance metrics which were used for system performance evaluation throughout this thesis are described. First, the concepts of HD and SD symbol demapping are introduced, then corresponding performance metrics are discussed.

2.5.1   Hard and Soft Decision Symbol Demapping

The symbol demapper estimates the transmitted symbols using the received noisy symbols after receiver-side DSP recovery algorithms (See Fig. 2.9) [59]. The ML symbol estimation can be expressed as

$$\widehat{x} = \arg\max_{x} f_{Y|X}(y|x),$$ (2.34)

where x and y are transmitted and received symbols, $x \in \mathscr{X}$ (where $\mathscr{X}$ represents constellation), $f_{Y|X}(y|x)$ is the channel transition probability density function. For instance, for 2D AWGN channel it is given by

$$f_{Y|X}(y|x) = \frac{1}{2\pi\sigma^2} \exp\left(\frac{-|y-x|^2}{2\sigma^2}\right).$$ (2.35)

where σ^2 is the noise variance. The maximization can be simplified by taking the logarithm of Eq. 2.34. In that case symbol estimation can be expressed as

$$\widehat{x} = \arg\min_{x} |y-x|^2.$$ (2.36)

This procedure represents symbol estimation based on minimum Euclidean distance, which is the HD metric.

The HD symbol demapper makes a symbol decision based on the minimum Euclidean distance rule or, alternatively, pre-calculated HD decision boundaries may be used. In the case of bit-wise HD decoding (e.g. employing BICM scheme with binary HD-FEC), the decided symbols are demapped into bits according to chosen symbol binary labeling (e.g Gray labeling), then demapped bits can be used for HD-FEC decoding.

For SD symbol demapping, a posteriori probabilities of received symbols ($f_{Y|X}(y|x_i)$, $x_i \in \mathscr{X}$) are estimated and then used for SD decoding. In the case of bit-wise SD decoding (e.g. employing BICM scheme with binary SD-FEC), the SD symbol demapper outputs bit-wise log-likelihood ratios (LLRs), which are then fed to the SD-FEC decoder.

LLRs for binary labels B_i ($i = \{1, \ldots, m\}$, where $m = \log_2 M$) can be expressed as [84]

$$\text{LLR}_i = \log \frac{f_{Y|B}(y|B_i = 1)}{f_{Y|B}(y|B_i = 0)},$$

(2.37)

Further details regarding LLRs calculations will be given in Chapter 4.

2.5.2 Bit Error Ratio

A widely used approach for system performance evaluation is based on the measurement of bit error rate (BER) of the system. The ideal performance metric is the BER measured at the output of FEC decoder, which is referred to as post-FEC BER. However, for offline system performance evaluation (i.e. using offline DSP) this approach may not be feasible, since post-FEC BER is required to be as low as 10^{-15} and such a low value can not be reliably estimated due to limited length of the received signal. However, note that in the case of concatenation of multiple FEC codes (e.g. SD-FEC for inner and HD-FEC for outer codes) the measurement of post-FEC BER of the inner code (SD-FEC) can be feasible (typically, the BER in the order of 10^{-6}–10^{-4}).

In order to avoid the FEC implementation and measurement of low BER values, a commonly adopted approach is to measure uncoded BER (referred to as pre-FEC BER), typically, using HD symbol demapping. It is assumed that if system operates under a certain pre-FEC threshold, error-free system operation is possible after FEC decoding. This assumption is accurate for systems employing HD-FEC — pre-FEC BER provides a reliable prediction of post-FEC BER. However, for systems employing SD-FEC pre-FEC BER is not a reliable performance metric and advanced information-theoretical metrics should be used [84].

The results presented in Chapter 3 are mainly based on the pre-FEC BER performance metric, while the usage of SD-FEC was assumed in the system. As noted, pre-FEC BER is not strictly accurate predictor of the system post-FEC BER employing SD-FEC, however, it still may serve as a good metric for relative comparison of the system performance gains under different conditions, especially, if the modulation format is fixed [84].

2.5.3 Achievable Information Rate

Achievable information rates (AIR) are the information theoretic quantities which represent the maximum transmission rate at which the system can reliably operate without the loss of information. AIRs such as the mutual information (MI) and generalized mutual information

(GMI) are the realible performance metrics for systems employing SD-FEC [84], [85]. They can be used to predict the post-FEC BER and may serve as good system design metrics.

Mutual Information

MI represents the maximum amount of information (the maximum number of information bits) that can be reliably transmitted over a noisy channel and is given by [84]–[86]

$$\mathrm{MI}(X;Y) = H(X) - H(X|Y) = \mathrm{E}\left[\log \frac{f_{Y|X}(y|x)}{f_Y(y)}\right], \tag{2.38}$$

where $H(\cdot)$ denotes the entropy. To achieve the transmission rate given by MI, an ideal FEC code is assumed, which guarantees that post-FEC BER approaches zero. In other words, the MI represents the upper limit on the AIR for a given channel.

MI can be calculated using the Monte-Carlo approach as

$$\mathrm{MI}(X;Y) \approx \frac{1}{N}\sum_{i=1}^{N}\log \frac{f_{Y|X}(y_i|x_i)}{f_Y(y_i)}, \tag{2.39}$$

where N is the number of received symbols.

Note that the actual optical fibre channel (corresponding channel transition probability density function $f_{Y|X}(y|x)$) is not known, hence, the concept of mismatched decoding is used. An auxiliary channel can be used for mismatched decoding (typically, the AWGN channel – see Eq. 2.35). MI calculated using mismatched decoding represents the lower bound on the true MI and is also an AIR. The AIR given by MI is the reliable performance metric for a system employing non-binary FEC schemes.

Generalized Mutual Information

For systems employing BICM and binary FEC, the AIR is defined by GMI. GMI is the sum of bit-wise MIs and can be expressed as [84], [85]

$$\mathrm{GMI}(X;Y) = \sum_{i=1}^{m}\mathrm{MI}(B_i;Y) = H(X) - \sum_{k=i}^{m}H(B_i|Y), \tag{2.40}$$

where $\mathrm{MI}(B_i;Y)$ denotes the MI between transmitted bits and received symbols.

Using LLRs defined in Eq. 2.37 and Monte-Carlo approach, the GMI can be calculated as [84]

$$\mathrm{GMI}(X;Y) \approx H(X) - \frac{1}{N}\sum_{k=1}^{m}\sum_{i=1}^{N}\log(1+\exp((-1)^{C_{k,i}}\mathrm{LLR}_{k,i})), \tag{2.41}$$

where C is the transmitted bit sequence, index k represents bit position and index i represents the received symbol. The mismatched decoding concept can also be used to calculate the LLRs (see Eq. 2.37). It should be noted that for probabilistically shaped inputs, the AIR may be impacted by the rate loss of the shaping scheme.

The results presented in Chapter 4 are mainly based on AIRs for the BICM scheme. Further details regarding calculation of AIR (e.g. for probabilistically shaped signals in the presence of rate loss) will be given in Chapter 4.

2.6   Chapter Summary

In this Chapter, the fundamentals of modern coherent fibre-optical communications systems are covered. Specifically, the concepts introduced in the chapter include WDM transmission system, fibre-optical transmission link and its impairments; transceiver and its impairments; modulation formats and coding schemes; transceiver DSP framework and metrics for system performance evaluation.

The material discussed here constitutes the basis framework for the original results and discussions developed in further Chapters of the thesis.

Chapter 3

Transceiver Optimization: Impairments Characterization & Mitigation

As introduced in Chapter 2, various impairments may be present in the transceiver. This Chapter covers some aspects of transceiver performance optimization through impairments characterization and mitigation techniques based on DSP.

This Chapter is based on the original published contributions: [**P.1**], [**P.2**], [**P.3**], [**P.4**], [**P.5**].

3.1   Introduction

Coherent optical communication systems are moving towards highly compact pluggable transceivers with lower cost, reduced power consumption, and increased flexibility enabled by photonics integration. To maintain rapid traffic growth in present transmission systems high-order modulation formats and high symbol rates are required. For transmission rates of 600 Gb/s per carrier (e.g. employing DP 64-QAM format at $\sim$ 64 GBd) and beyond, the overall system performance becomes ultimately limited by low back-to-back performance margin, due to limited transceiver SNR and impairments in electrical and optical components (see Chapter 2, Section 2.3.3).

It is essential to accurately characterize transceiver and pre-compensate the impairments before the transceiver operation. Alternatively, advanced DSP algorithms can be used to mitigate the impairments adaptively during normal system operation (without prior characterization).

In Section 3.2, transceiver characterization techniques are discussed. Specifically, two approaches for skew calibration are demonstrated: (i) based on the Gardner timing error detector (Section 3.2.1) and (ii) signal image suppression (Section 3.2.2).

In Section 3.3, mitigation techniques for IQ impairments are demonstrated. In Section 3.3.1. a receiver-side DSP algorithm for mitigation of transmitter modulation impairments and skews is proposed. Then, in Section 3.3.2 the application of this technique is extended for compensation of electrical IQ cross-talk. Finally, in Section 3.3.3, the impact of frequency-dependent IQ imbalance is generalized and MIMO transmitter pre-emphasis is proposed.

3.2 Transceiver Impairments Characterization Techniques

The performance of high-speed transceivers can be severely degraded by uncompensated skews between in-phase/quadrature (IQ skew) and x-polarization/y-polarization (XY skew) tributaries of the signal, particularly by IQ skew. Unwanted skews at the transmitter side may originate from the DACs, electrical drivers, optical modulator and RF paths between them. Skew sources within the receiver are photodiodes, ADCs and also RF paths. Further, due to signal propagation through an optical fiber the impact of transmitter-side XY skews can be mixed with the impact of receiver-side XY skews in a complicated way because of DGD, SOP rotation and PMD effects. Therefore, it is highly desirable to have all the skews calibrated at sub-picosecond level before normal transmission operation of the transceiver.

There are a number of techniques proposed to deal with receiver-side skews. One type of solution is based on advanced adaptive equalization, either real-valued [87], [88] or widely linear [89]. These equalizer architectures are able to tolerate relatively large (i.e. in the order of ps) receiver-side skews. A calibration technique based on minimization of BER or mean squared error (MSE) and adjusting the sampling phase in the ADC for each signal tributary was proposed in [90]. Another method of receiver skew estimation and compensation is based on a Gardner frequency-domain timing error detector (FD-TED) and a time-domain bank of signal interpolators (pre-emphasis filters) [91].

To deal with transmitter-side skews various techniques have also been presented: a method based on reconfigurable interference [92]; a method based on clock tone amplitude (CTA) extraction from a direct detected signal in combination with an optimization procedure performed by the genetic algorithm [93], [94]; a digital transmitter pre-distorter based on the indirect learning architecture using feedback from the receiver-side [95], and self-calibration

based on generation and detection of arbitrary sine waves [96]. Mitigation for the impact of transmitter-side impairments at the receiver performed by DSP was investigated in [97].

In general, a desirable solution is to avoid using bulky and expensive equipment and to calibrate all the skews at once in a low complexity way. In this Section, two different skew calibration approaches are proposed, which should be applied prior to normal transceiver operation and potentially may offer low-complexity implementation (based on DSP) compared to other previously proposed techniques. The first technique offers calibration of both transmitter and receiver skews using a pair of transceivers. The second technique is limited to calibrating transmitter IQ skew only, however, requires only a single transceiver in back-to-back configuration.

3.2.1 Transceiver Skew Calibration Using Gardner Clock Detector

In the following, an algorithm for the estimation and compensation of both IQ and XY skews for the transmitter-side and receiver-side of a DP M-QAM transceiver based on receiver-side DSP is proposed. The calibration is performed in a back-to-back configuration, where requirements are (i) a small frequency offset between the transmitter and receiver (which allows separation of transmitter and receiver IQ skews) and (ii) an SOP rotation (which allows separation of transmitter and receiver XY skews).

Skew Impact

The impact of the transmitter and receiver IQ skews in the back-to-back configuration can be expressed as

$$
\begin{aligned}
I_{\mathrm{rx}}(t) &= \mathrm{Im}[\{I_{\mathrm{tx}}(t) + iQ_{\mathrm{tx}}(t) * \delta(t - \tau_{\mathrm{tx}}^{\mathrm{iq}})\}e^{-i2\pi\Delta ft + \phi(t)}], \\
Q_{\mathrm{rx}}(t) &= \mathrm{Re}[\{I_{\mathrm{tx}}(t) + iQ_{\mathrm{tx}}(t) * \delta(t - \tau_{\mathrm{tx}}^{\mathrm{iq}})\}e^{-i2\pi\Delta ft + \phi(t)}] * \delta(t - \tau_{\mathrm{rx}}^{\mathrm{iq}}),
\end{aligned}
\tag{3.1}
$$

where $I(t)$ and $Q(t)$ are the I and Q signal tributaries, subscripts tx and rx stand for transmitter-side and receiver-side; $\tau_{\mathrm{tx}}^{\mathrm{iq}}$ and $\tau_{\mathrm{rx}}^{\mathrm{iq}}$ are transmitter and receiver IQ skews; $\delta(t - \tau)$ is the delta function delayed by the skew τ; $*$ represents a convolution operation. Only the single polarization case is shown here for simplicity of formulation.

Note that the contributions of the transmitter-side and receiver-side IQ skews are separated by the frequency offset and phase noise term. Frequency offset leads to fast rotations of transmitted I and Q components of the signal, which effectively average the impact of transmitter IQ impairments. Hence, the compensation of transmitter IQ impairments (including IQ skew) is not achievable before the carrier is fully recovered.

The effect of transmitter and receiver XY skews mixing in back-to-back configuration in the presence of SOP rotation can be shown as

$$
\begin{pmatrix} S_{rx}^{x}(t) \\ S_{rx}^{y}(t) \end{pmatrix} = \begin{bmatrix} \delta(t - \tau_{rx}^{xy}) & 0 \\ 0 & 1 \end{bmatrix} * \begin{bmatrix} 1 & 0 \\ 0 & e^{-i\gamma} \end{bmatrix} \begin{bmatrix} \cos(\alpha) & \sin(\alpha) \\ -\sin(\alpha) & \cos(\alpha) \end{bmatrix} \begin{pmatrix} S_{tx}^{x}(t) * \delta(t - \tau_{tx}^{xy}) \\ S_{tx}^{y}(t) \end{pmatrix},
$$
(3.2)

where $S(t) = I(t) + iQ(t)$ is the complex-valued signal, τ_{tx}^{xy} and τ_{rx}^{xy} are transmitter and receiver XY skews, α is the SOP rotation angle, γ is the phase retardation angle. Transformation is represented by concatenation of rotation and phase retardation matrices, PMD effects are neglected in the back-to-back configuration. Note that for $\alpha = 0°$, the skews from transmitter and receiver sides are simply summed up and not distinguishable, while for $\alpha = 45°$ the skews are mixed in a complicated way.
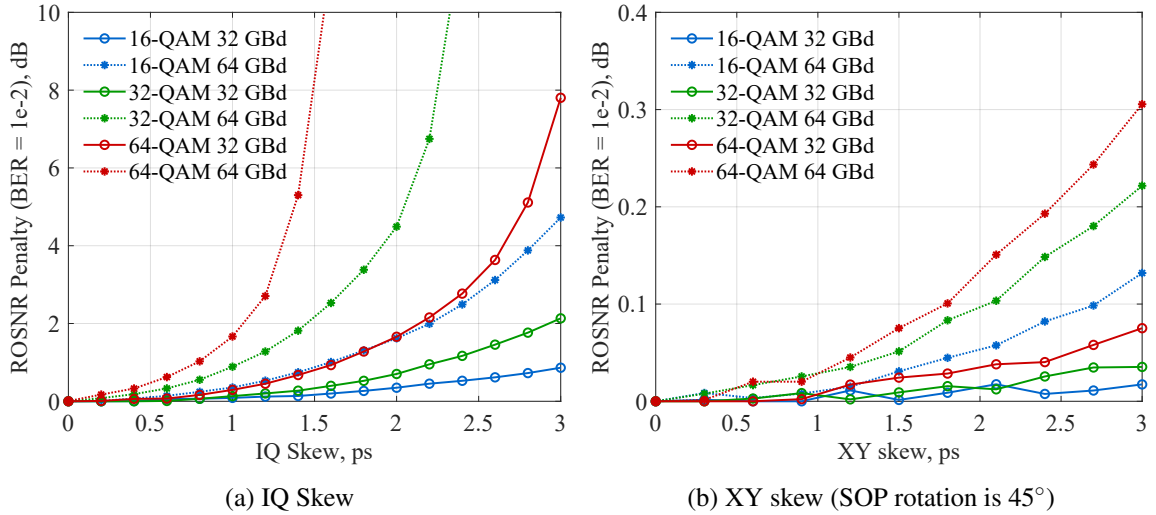
Fig. 3.1. ROSNR penalty vs. skew in back-to-back configuration: (a) IQ skew, (b) XY skew (SOP rotation is 45°).

The performance penalty due to the impact of transmitter IQ and XY skew was investigated in numerical simulations. The back-to-back configuration was simulated (only ASE noise was considered, OSNR was set to 40 dB) and performance was evaluated via a generic DSP chain according to Fig. 2.8 and Fig. 2.9. When evaluating the impact of IQ skew, XY skew was not considered, and analogously when evaluating the impact of XY skew, IQ skew was not considered. For XY skew simulations, the SOP rotation angle was set to 45°. Fig. 3.1 shows the penalty in terms of required OSNR (ROSNR) at BER of 10^{-2} in back-to-back configuration for 16-QAM, 32-QAM, 64-QAM at 32 GBd and 64 Gbd.

In the case of IQ skew (see Fig. 3.1 (a)), the ROSNR penalty significantly increases with increased modulation order and symbol rate. For 16-QAM at 32 GBaud the ROSNR penalty is less then 1 dB for 3 ps skew, while for 32-QAM and 64-QAM the penalties are 2 dB and 8 dB, respectively. At the higher symbol rate of 64 GBd, the tolerance to skew is significantly reduced. The same penalties are observed for 1.5 ps skew, which demonstrates two-fold decrease in skew tolerance compared to 32 GBd case.

In the case of XY skew (see Fig. 3.1 (b)), the ROSNR penalty follows the same relative trend as for IQ skew, however, the absolute penalty values are much smaller. For 3 ps skew the penalties for 16-QAM, 32-QAM and 64-QAM at 64 Gbd are 0.13 dB, 0.22 dB and 0.3 dB. At lower symbol rate the penalties are negligible. This is due to the different nature of the XY skews impact and ability of the clock recovery and adaptive equalization DSP stages to partially compensate for it (in case of zero SOP rotation, the XY skew can be fully compensated).

These observations suggests that IQ skews must be calibrated with sub-picosecond accuracy, while XY skews must calibrated with picosecond accuracy in order to enable the system operation employing high symbol rate and modulation order. Note that it is expected that receiver skews should result in similar performance penalties.

Calibration Algorithm

In order to perform skew calibration, timing misalignments for all signal tributaries must be estimated first. Then, skew compensation can be achieved using the banks of pre-emphasis filters residing at transmitter and receiver sides.

Previously, in Section 2.4.2 it was shown, that frequency-domain Gardner timing error detector (FD-TED) can be used for clock recovery, whereby the sampling phase of the signal is corrected (see Chapter 2, Section 2.3.2). However, FD-TED can also be used to obtain the signal characteristics to perform the skew estimation.
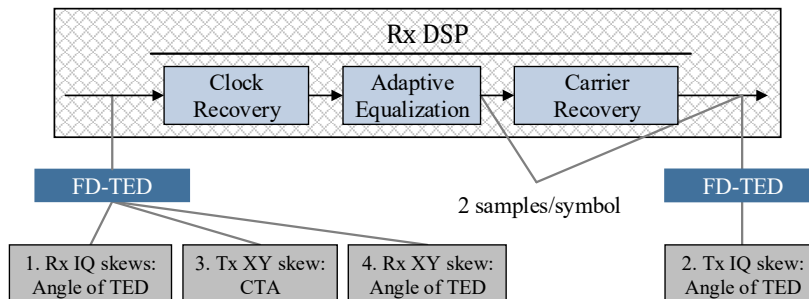
Fig. 3.2. Receiver DSP flow for skew estimation.

In Fig. 3.2 the simplified DSP chain for skew estimation is shown. An additional FD-TED is applied before the clock recovery and after CPR. The skew calibration can be done as follows:

1. *Receiver IQ skew estimation:*

   Receiver-side skews can be estimated using the skew estimation algorithm proposed in [91]. Sampling phase errors of I and Q signal tributaries are extracted using the FD-TED (which is applied to I and Q tributaries of the signal separately). Then, the difference between sampling phase errors of I and Q signals represent the skew, which can be expressed as

   $$\tau_{iq} = \text{angle}\Big[\sum_{k=0}^{N/2-1} X_I(k) \cdot X_I^*(k+N/2)\Big] - \text{angle}\Big[\sum_{k=0}^{N/2-1} X_Q(k) \cdot X_Q^*(k+N/2)\Big], \quad (3.3)$$

   where X_I and X_Q are the FFTs of I and Q signal tributaries, which can be calculated as

   $$X_I = \frac{1}{2}(X + X^*),$$
   $$X_Q = -\frac{i}{2}(X - X^*), \qquad (3.4)$$

   where X is the FFT of the complex-valued signal.

2. *Transmitter IQ skew estimation:*

   By applying the same skew estimator after adaptive equalization and CPR, transmitter IQ skews can be estimated. Once polarization tracking and CPR are complete, information about transmitter IQ impairments is available [97]. Note that the signal at the output of the adaptive equalizer is not down-sampled and CPR is performed with 2 samples/symbol in order to preserve timing information in the signal (since FD-TED uses the frequency components above Nyquist frequency to extract timing information).

3. *Transmitter XY skew estimation:*

   The technique described above can not be applied if both receiver and transmitter XY skews are present, since it may provide incorrect skew estimation due to the skews mixing effect (see Eq. 3.2). Therefore, transmitter XY skew should be calibrated first. The clock tone amplitude (CTA) extracted from both the X and Y signals using FD-TED (in that case, applied to complex-valued signal in each polarization) is degraded

by transmitter XY skew in the presence of SOP rotation [93], [94]. The CTA is given by

$$\text{CTA} = \text{abs}\left[\sum_{k=0}^{N/2-1} X(k) \cdot X^*(k+N/2)\right], \tag{3.5}$$

where $\text{abs}[\cdot]$ denotes absolute value operator.

By sweeping transmitter XY skews (using the bank of pre-emphasis filters) and maximizing CTA (averaged for both polarizations) the optimal skew value can be determined.

4. *Receiver XY skew estimation:*

   After the transmitter XY skew is compensated as described above, the first skew estimator can be re-used to estimate receiver XY skew. For that purpose, the sampling phase difference should be measured between the signal components in different polarizations.

All the calibration procedures should be done in the back-to-back configuration under high OSNR and when only SOP rotation is observed (no PMD effects). Note that the relative accuracy (in terms of the ratio of estimated skew to the symbol duration) of FD-TED does not depend on the signal symbol rate.

Numerical Simulations

To verify the proposed skew calibration procedure, the operation of a 30 GBd DP 16-QAM transceiver in the back-to-back configuration was numerically simulated (OSNR was set to 40 dB, laser linewidth was set to 100 kHz, frequency offset was set to 0, 1, 10 MHz). The calibration procedure was tested with a range of deliberately set transmitter and receiver IQ and XY skews.

For the receiver IQ skew sweep, the transmitter IQ skew was set to 3 ps, and similarly, for the transmitter IQ skew sweep, the receiver IQ skew was set to 3 ps. Fig. 3.3 shows the estimated IQ skew as a function of set IQ skew values. Without a frequency offset, IQ skew estimation (both for receiver and receiver IQ skews) is incorrect due to mixing of transmitter and receiver IQ skews. A frequency offset of 1 MHz results in smaller estimated skew deviation. However, a frequency offset in the order of tens of MHz is sufficient to fully cancel the effect of IQ skews mixing. With sufficient frequency offset, the skew estimation accuracy is better than 0.1 ps for transmitter and receiver IQ skews.

For transmitter XY skew characterization, the SOP rotation angle was set to $\alpha = 25°, 35°, 45°$. The phase retardation angle has no impact on the skew estimation. Fig. 3.4 (a)

(a) Receiver IQ skew

(b) Transmitter IQ skew
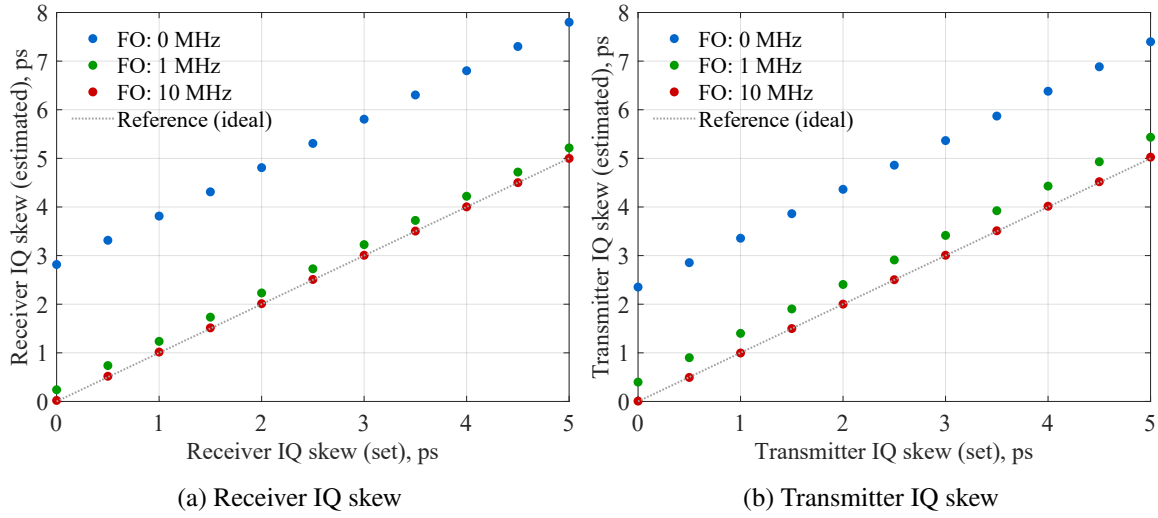
Fig. 3.3. IQ skew estimation: (a) receiver, (b) transmitter.

(a) Transmitter XY skew
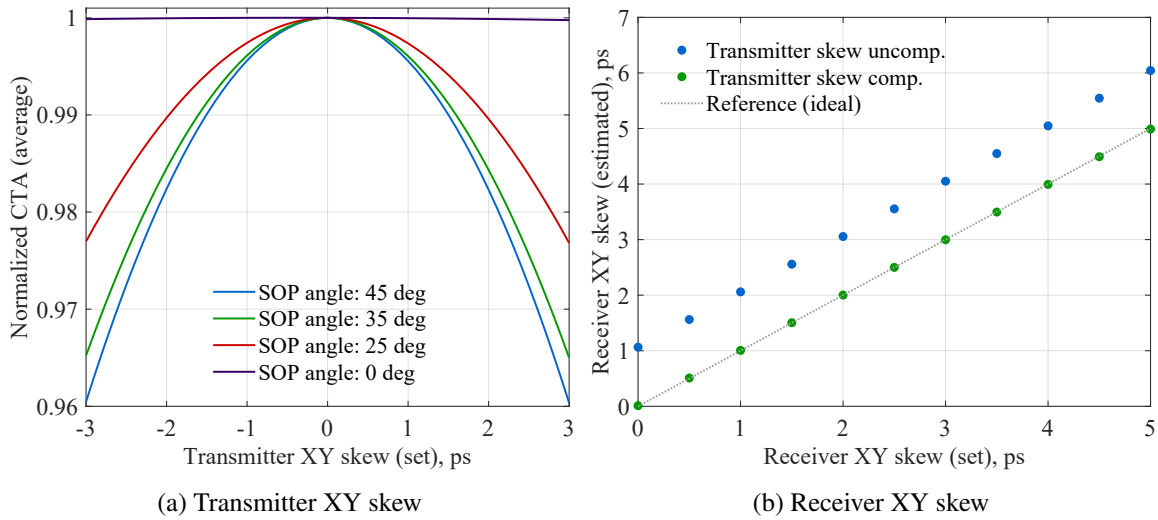
(b) Receiver XY skew

Fig. 3.4. XY skew estimation: (a) transmitter (b) receiver.

demonstrates the normalized CTA as the function of deliberately set transmitter XY skew. Without SOP rotation there is no CTA degradation caused by the introduced transmitter XY skew, while when SOP rotation is present CTA degradation is observed. The best CTA sensitivity to transmitter XY skew is observed for $\alpha = 45°$. Considering that the CTA peak is weakly pronounced, the accuracy of XY skew estimation can be identified to be within 1 ps. Note that this accuracy is sufficient to keep the ROSNR penalty negligible (see Fig. 3.1 (b)).

For the receiver XY skew sweep, two cases were considered: compensated and uncompensated transmitter XY skew, which was set to 3 ps. The SOP rotation angle was set to $\alpha = 35°$. Fig. 3.4 (a) demonstrates the estimated receiver XY skew as a function of set

receiver XY skew values. It can be observed that if transmitter XY skew is uncompensated, receiver skew estimation is incorrect due to mixing of transmitter and receiver XY skews.

Summary

By performing skew calibration of a DP M-QAM transceiver in back-to-back configuration using the proposed algorithm, both transmitter and receiver skews can be estimated and compensated with required accuracy. For successful and accurate calibration two conditions must be satisfied: sufficient frequency offset between receiver and transmitter, the SOP rotation close to $45°$. The frequency offset can be guaranteed by using a pair of transceivers, or a transceiver with two separate lasers for transmitter and receiver sides. The SOP rotation can be realized by using a polarization controller or short dedicated patch cord with a fixed SOP rotation angle (e.g. modified polarization maintaining patch cord).

3.2.2 Transmitter IQ Skew Calibration Using Signal Image Suppression

In the previous Section, it was shown that the main performance degradation is caused by the IQ skews. In the following, an alternative algorithm for transmitter IQ skews calibration of a DP M-QAM transceiver based on signal image power spectrum measurements of artificially frequency-upshifted signal is proposed. This is performed in a back-to-back configuration under high OSNR.

Calibration Technique

To perform the calibration procedure, the transmitted signal is frequency-upshifted by digitally introducing a frequency offset to the complex-valued base-band signal using transmitter-side DSP. The frequency-upshift can be expressed as $S(t)e^{i\Delta\omega t}$, where $S(t)$ is the complex-valued base-band signal and $\Delta\omega$ is the frequency offset.

The time-domain signal at the output of the transmitter is given by

$$S'(t) = \underbrace{\text{Im}[S(t)e^{i\Delta\omega t}]}_{\text{I driving signal}} + \underbrace{\text{Re}[S(t)e^{i\Delta\omega t}] * \delta(t-\tau)}_{\text{Q driving signal}}, \tag{3.6}$$

where the first term represents the I driving signal and the second term represents the Q driving signal delayed by τ.

The equivalent signal represented in the frequency domain is given by

$$S'(\omega) = \underbrace{\frac{1 + e^{i\omega\tau}}{2} S(\omega - \Delta\omega)}_{\text{Signal}} + \underbrace{\frac{1 - e^{i\omega\tau}}{2} S^*(\omega + \Delta\omega)}_{\text{Image}}, \tag{3.7}$$

where the first term represents the signal itself and the second term represents the signal image due to IQ imbalance in the form of IQ skew.

In the absence of IQ skew the total signal power is contained within the signal spectrum only, while in the presence of IQ skew some fraction of the signal power spreads out to the signal image spectrum. This consideration enables the estimation of the IQ skew by performing a power spectrum analysis by the means of receiver-side DSP, for which re-use of FFT blocks already deployed for signal recovery (e.g. CD compensation) is feasible. Note that the frequency offset $\Delta\omega$ has to be sufficient to separate signal and image spectra (to accurately measure the power leakage) and is also limited by the sampling rate of the receiver (such that the highest frequency does not exceed half of the sampling frequency). Fig. 3.5 shows the spectrum of the signal and its image (partially overlapped) in the presence of 1.5 ps IQ skew.

One of the possible metrics for the IQ skew estimation is given by the ratio between the power within the signal spectrum and the power within the combined signal and image spectrum. In logarithmic scale it can be expressed as

$$\text{Metric} = 10 \cdot \log_{10}(P_{\text{signal}}) - 10 \cdot \log_{10}(P_{\text{signal+image}}). \tag{3.8}$$

The IQ skew is swept within a desirable range using the bank of pre-emphasis filters in the transmitter-side DSP. When the metric obtained by receiver-side DSP is minimized, the IQ skew value is found. The calibration procedure should be done in the back-to-back configuration under high OSNR.

Note that, the appearance of the signal image may be also associated with other IQ impairments (e.g. gain imbalance or quadrature error), which are not reflected in Eq. 3.7. The proposed metric should be resilient to the presence of gain imbalance, however, in the presence of quadrature error the accuracy of skew estimation may be degraded. Hence, the MZMs should be accurately biased before the skew estimation.

Numerical and Experimental Results

The calibration technique has been tested for a 32 GBd DP 16-QAM transceiver in numerical simulations and experiment. In the experimental test, a lithium niobate MZM modulator with
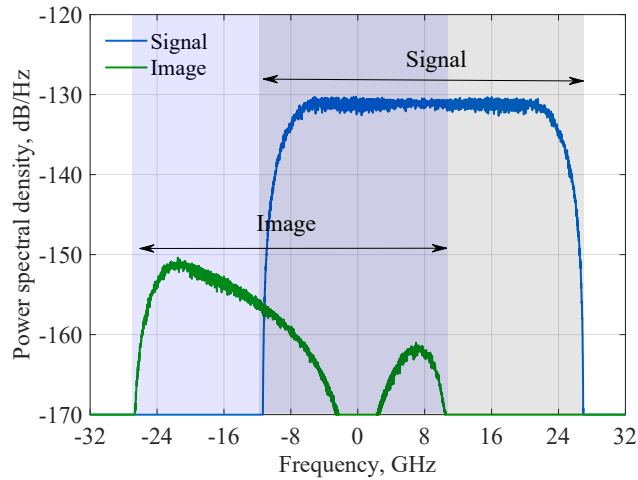
Fig. 3.5. Simulated signal and image power spectral density spectra in the presence of 1.5 ps IQ skew.

64 GSa/s DAC were used for the transmitter side, while a coherent receiver with high-speed oscilloscope (100 GSa/s ADC) were used for the receiver-side. The MZM was accurately biased before the skew measurements. To provide a suitable reference, the skew values of the experimental setup were calibrated with 0.1 ps accuracy by extensive timing misalignment measurements of arbitrary sinewaves (also, verified with the techniques presented in the previous section) prior to carrying out measurements for the technique under test.
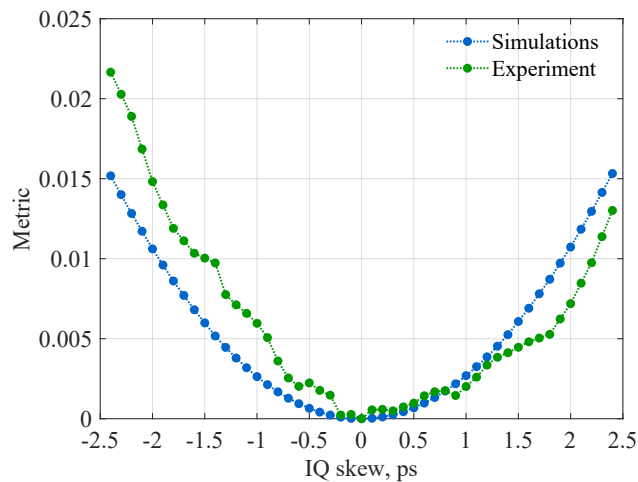
Fig. 3.6. IQ skew estimation for X polarization (Metric vs. IQ skew) in simulations and experiment.

The OSNR level was set to maximum $\sim$ 38 dB, 8 GHz frequency offset was added to the signal by DSP at the transmitter, and skew values were swept over a -2.4 ps to 2.4 ps range ($\sim$ 15% of the symbol duration) with the 0.1 ps step for the signal component in the x-polarization (for y-polarization the skew value remained constant). Power spectrum

measurements were performed using FFT blocks of the size of 512 samples and averaged over a 6 μs window for each skew value.

Fig. 3.6 shows the calculated metric as a function of transmitter IQ skew. The IQ skew value for the signal component in the x-polarization can be identified close to 0 ps as expected with an accuracy of a few tenths of ps both in numerical simulations and experiment. Note that the skew value for the signal component in the y-polarization can be estimated likewise after the x-polarization is calibrated.

Summary

The IQ skews of a DP *M*-QAM transmitter can be estimated and compensated to sub-picosecond level using the new low complexity self-calibration technique based on signal power spectrum analysis and performed by DSP. Sub-picosecond accuracy was demonstrated in numerical simulations and confirmed in experiment for 32 GBd DP 16-QAM.

3.3 Transceiver Impairments Mitigation Techniques

In the previous Section, the impact of transceiver skews on system performance was considered and two approaches for skew calibration were proposed. However, to further improve the overall robustness of transceiver operation, other IQ impairments should be taken into consideration.

In general, IQ impairments may be divided into two categories: frequency-dependent and frequency-independent. Frequency-independent impairments include gain and quadrature imbalance, while frequency-dependent impairments include IQ skew, IQ cross-talk (which represents coupling between I and Q channels) and also frequency response mismatch between I and Q channels. Note that all the mentioned impairments may be present to some extent both at the transmitter and receiver sides.

There are multiple techniques for receiver IQ imperfections compensation. Receiver gain and quadrature imbalances can be compensated by the well-know GSOP technique [53]. Receiver skews can be compensated using the technique presented in [91] (including techniques proposed in the previous section). Alternatively, IQ impairments can be compensated using 4x4 real-valued (RV) [87] or 4×2 widely linear (WL) [89] MIMO adaptive equalizers. Note that 4×4 RV or 4×2 WL MIMO approaches allow compensation for all the mentioned impairments originating from the receiver side.

Typically, transmitter IQ impairments are calibrated before system operation [95], [98], [99] (including techniques proposed in the previous section). However, the requirements for calibration accuracy are significantly increased when high symbol rate and modulation

order systems are employed and any deviation of the estimated impairments over time may lead to performance penalties. Alternatively, transmitter IQ impairments can be estimated and mitigated within receiver DSP during normal transceiver operation. A compensation technique based on a blind adaptive source separation was proposed in [100], which may compensate only transmitter gain and quadrature imbalance. A receiver-side approach for mitigation of transmitter IQ impairments based on an adaptive post-equalizer (e.g. using 2x2 or 4x4 RV MIMO after CPR) was demonstrated in [97], [101]. Also, in [101] it was confirmed that joint compensation of receiver and transmitter IQ impairments is possible at the receiver side using two adaptive equalization stages before and after CPR.

In this Section, an advanced post-equalization approach is proposed, which offers significantly improved tolerance to modulation impairments and IQ skews compared to previously proposed techniques. Then, the application of the post-equalizer is extended to compensation of transmitter electrical IQ cross-talk, which may potentially relax the requirements for IQ cross-talk levels in highly compact transceiver assemblies (such cross-talk may occur within the MZMs of photonic integrated circuits). Finally, the application of the post-equalizer is generalized for compensation of multiple frequency-dependent impairments, and also low-complexity MIMO pre-emphasis is proposed, which offers significant advantage under the impact of multiple impairments.

3.3.1 Receiver-Side Compensation of Transmitter Modulation Impairments and IQ Skews

Significant performance penalty can be caused by transmitter IQ impairments, such as gain and quadrature imbalance, bias offset, and timing skew. To maintain those impairments within acceptable penalty limits, transmitters are typically calibrated during manufacture (or, alternatively, during power-up), and high-speed control loops are deployed to automatically maintain each MZM at its optimum operation condition over wavelength, temperature and lifetime. As the modulation order and symbol rate of the system increase, requirements for the precision of calibration and control loops operation increase accordingly.

In the following, an advanced post-equalization approach in the receiver DSP is proposed, which enables highly tolerant and robust transceiver operation under severe impact of transmitter modulation impairments and IQ skew.

Equalization Structure

Signal recovery algorithms in the receiver-side DSP are highly sensitive to transmitter IQ impairments especially when using high-order modulation and high symbol rate signals. The

post-equalization approach for compensation of transmitter impairments must be applied after the carrier is fully recovered (frequency offset and phase noise are removed), since frequency offset and phase noise conceal the impact of transmitter impairments and only receiver impairments compensation is achievable (see Section 3.2.1). However, adaptive equalization and CPR which precede the post-equalization stage may exhibit severe deterioration in the presence of transmitter IQ impairments, since these algorithms typically work on a DD basis and wrong decisions are more likely to occur due to mismatch of the reference and impaired constellations.
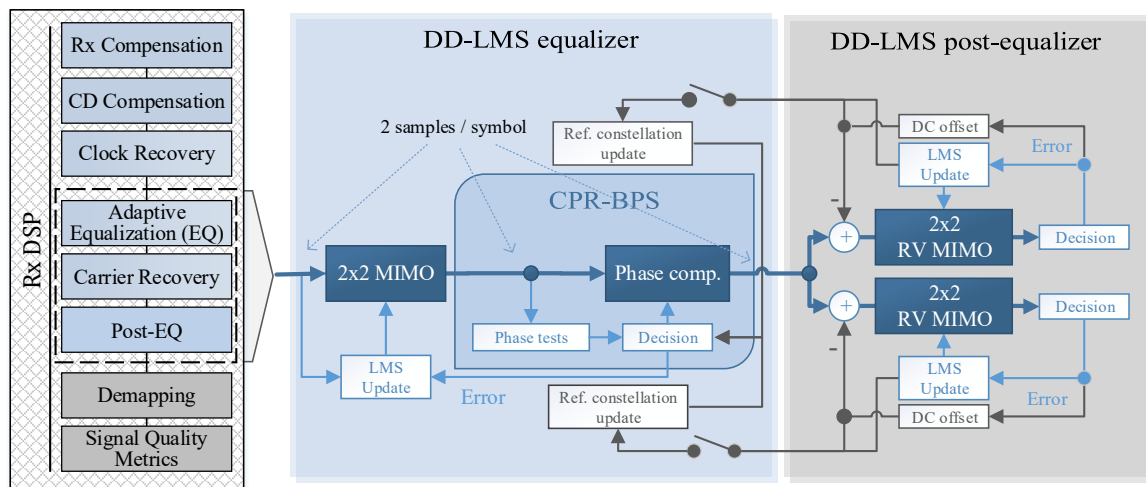
Fig. 3.7. Receiver DSP chain.

The technique described here is based on joint operation of adaptive equalization, CPR and adaptive post-equalization in a DD loop (see Fig. 3.7). First, DD-LMS 2x2 MIMO equalization is performed in conjunction with CPR based on the BPS algorithm. Note that the signal at the output of the MIMO equalizer is not down-sampled and CPR operates at 2 samples/symbol to preserve full timing information in the recovered signal. Operation of CPR at 2 samples/symbol is performed by making a decision (obtaining the phase estimate) for the BPS algorithm using the main sample (the sample which contains the information), then the same phase estimation is applied to recover the phase for both consequent samples. After polarizations are demultiplexed and the carrier is recovered, the DC offset of the signal is removed and then two DD-LMS 2x2 RV MIMO equalizers are employed for post-equalization of I and Q signal components within each polarization, which enables transmitter IQ impairments compensation. Fractionally-spaced post-equalization (i.e. 2 samples/symbol) provides more accurate IQ skew compensation with fewer taps. At the output of the post-equalizers the signal is down-sampled to 1 sample/symbol (the main sample is kept).

DC offset estimation and removal is performed using a closed loop update algorithm. DC offset estimation can be expressed as

$$DC(n) = DC(n-1) - \mu_{DC}DC^{res}(n),$$ (3.9)

where DC^{res} is the residual DC offset, which is equal to the post-equalizer LMS error function e, that is, the difference between the output equalized symbol and decided symbol (see Eq 2.26); μ_{DC} is the loop gain factor.

In order to maintain robust equalization and CPR in the first place before post-equalization, adaptive adjustment of the reference constellation is performed using the post-equalizer tap-weights and estimated signal DC offset. The reference constellation adjustment is represented by an affine class of transformations on a complex-plane and can be expressed as

$$\begin{pmatrix} z_r' \\ z_i' \end{pmatrix} = \begin{bmatrix} k_{rr} & k_{ir}' \\ k_{ri}' & k_{ii} \end{bmatrix}^{-1} \times \begin{pmatrix} z_r \\ z_i \end{pmatrix} + \begin{pmatrix} DC_r \\ DC_i \end{pmatrix},$$ (3.10)

where z and z' are constellation points before and after transformation (i.e. complex-valued coordinates), subscripts r and i stand for real and imaginary components. Coefficients k are given by

$$k_{nn} = \sum h_{nn},$$
$$k_{ir}' = k_{ri}' = (k_{ir} + k_{ri})/2,$$ (3.11)

where h_{nn} represents post-equalizer tap-weights of real-to-real (rr), imaginary-to-real (ir), real-to-imaginary (ri), imaginary-to-imaginary (ii) FIR filters. The mean value of the transformation cross-coefficients k_{ir} and k_{ri} is taken to restrict uncontrolled constellation rotation in the affine transformation. The constellation after transformation is normalized by its standard deviation to restrict uncontrolled gain of the system, which can be expressed as

$$z' = \frac{z'}{STD[z']},$$ (3.12)

where $STD[\cdot]$ denotes the standard deviation operator.

The reference constellation should be updated periodically, but not continuously (i.e. the update rate should be an order of magnitude slower compared to the equalizers) to allow both equalizers some time to re-converge to new conditions. It is expected that the considered IQ impairments do not vary rapidly. At system start-up, initial pre-convergence and reference constellation estimation are performed using QPSK pilot symbols which are embedded in the data stream. Note that the standard BPS algorithm for CPR by default

relies on $\pi/2$ constellation symmetry, however, in the presence of IQ imbalances and bias offset, the constellation is asymmetric. To take this into account, CPR is implemented as a multiple-stage BPS algorithm and the phase is searched over the whole 2π range. Cycle slips are avoided by increasing the length of the moving average filter for phase unwrapping.

Numerical Simulations

The proposed post-equalization approach was characterized both in numerical simulation and experimentally in the back-to-back configuration. Its performance was compared with the post-equalizer presented in [97] and the GSOP algorithm [53] combined with DC offset removal block applied after CPR (which replaces the post-equalizer). Note that, typically, the GSOP technique is used for the receiver IQ imbalances compensation, however, placing it after CPR allows transmitter IQ imbalances to be compensated. The post-equalizer presented in [97] is referred to as the conventional post-equalizer, while the post-equalization approach introduced here is referred to as the "advanced post-equalizer" (see Fig. 3.8).

The system employing 32-QAM and 64-QAM at 32 and 64 GBd with RRC pulse shaping (0.2 roll-off factor) was numerically simulated. Transmitter and LO laser linewidths were set to 100 kHz. The penalty in terms of ROSNR at BER of 10^{-2} was characterized for each individual IQ impairment (quadrature error, gain error, bias offsets, IQ skew).

Fig. 3.8 shows that advanced post-equalization provides approximately two-fold improvement in mitigation of all considered transmitter IQ impairments. In particular, for 64-QAM an increase in tolerance to quadrature error (see Fig. 3.8 (a)) from $8°$ to more than $18°$, gain error (see Fig. 3.8 (b)) from 1.2 dB to 2 dB, and bias offsets (see Fig. 3.8 (c)) from 3% to 8% can be seen at the ROSNR penalty level of 0.5 dB compared to conventional post-equalizer and GSOP technique. Note that conventional post-equalizer and GSOP technique demonstrate equivalent tolerance to gain error, quadrature error and bias offsets.

Fig. 3.8 (d-f) demonstrates that fractionally-spaced post-equalization significantly improves the tolerance to IQ skew. Using FIR post-equalizer filters with 3 taps, for 64-QAM at 64 GBd the skew tolerance is improved from 1.1 ps to 2 ps at the ROSNR penalty level of 0.5 dB compared to the conventional post-equalizer. Also, the advanced post-equalizer with 3 taps outperforms the conventional post-equalizer with 5 taps. Note that the GSOP technique can not provide IQ skew compensation, since it can be considered as single-tap filter.

Experimental Characterization

To verify numerical predictions experimentally, a back-to-back transmission of 16-QAM and 32-QAM signals at 40 GBd with RCC pulse shaping (0.2 roll-off factor) was investigated. A

(a) Quadrature error (32 GBd)

(b) Gain error (32 GBd)

(c) Bias offset (32 GBd)

(d) IQ skew (32 GBd, 3 taps)

(e) IQ skew (64 GBd, 3 taps)

(f) IQ skew (64 GBd, 5 taps)
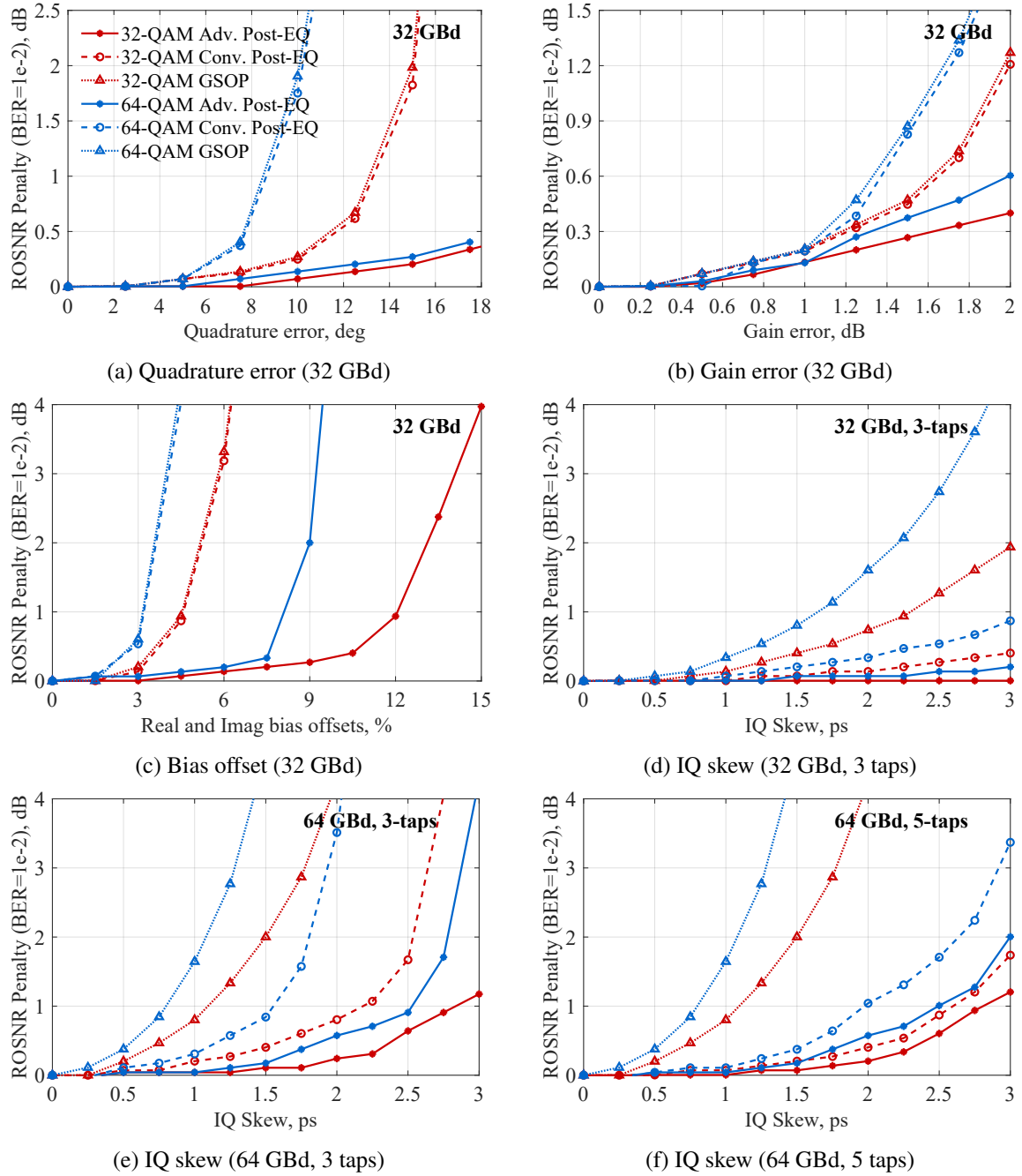
Fig. 3.8. ROSNR penalty in numerical simulations for 32/64-QAM: (a) quadrature error (32 GBd), (b) gain error (32 GBd), (c) real and imaginary biases (32 GBd), (d) IQ skew (32 GBd, 3 taps), (e) IQ skew (64 GBd, 3 taps), (e) IQ skew (64 GBd, 5 taps).

LiNbO$_3$ MZM modulator with 64 GSa/s DAC were used for the transmitter side, while a coherent receiver with high-speed oscilloscope (100 GSa/s ADC) were used for the receiver-side. Transmitter and LO laser linewidth was $\sim$ 100 kHz. The noise loading was performed
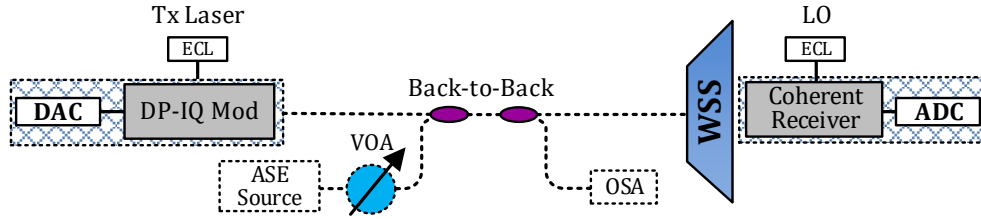
Fig. 3.9. Back-to-back experimental setup with noise loading.

as shown in Fig. 3.9. An ASE noise source and variable optical attenuator (VOA) were used for varying OSNR, while an optical spectrum analyzer (OSA) was used for OSNR measurement. A wavelength selective switch (WSS) was used to filter the ASE noise out of the signal band. DSP was performed offline according to the generic flow shown in Fig. 3.7.

To provide a suitable reference, the transmitter was first precisely calibrated and the data set referred to as "calibrated" was acquired and processed. Then the transmitter was detuned to a poorly calibrated state, which may represent a typical start-up state of a transmitter (skew of ~ 1.7 ps, gain error of ~ 0.7 dB, quadrature error of $\sim 10°$, real and imaginary bias offsets of $\sim 5\%$ in both polarizations). Then, a second data set was acquired and processed using the compensation techniques under consideration. 3-tap FIR filters were used for both conventional and advanced post-equalization.
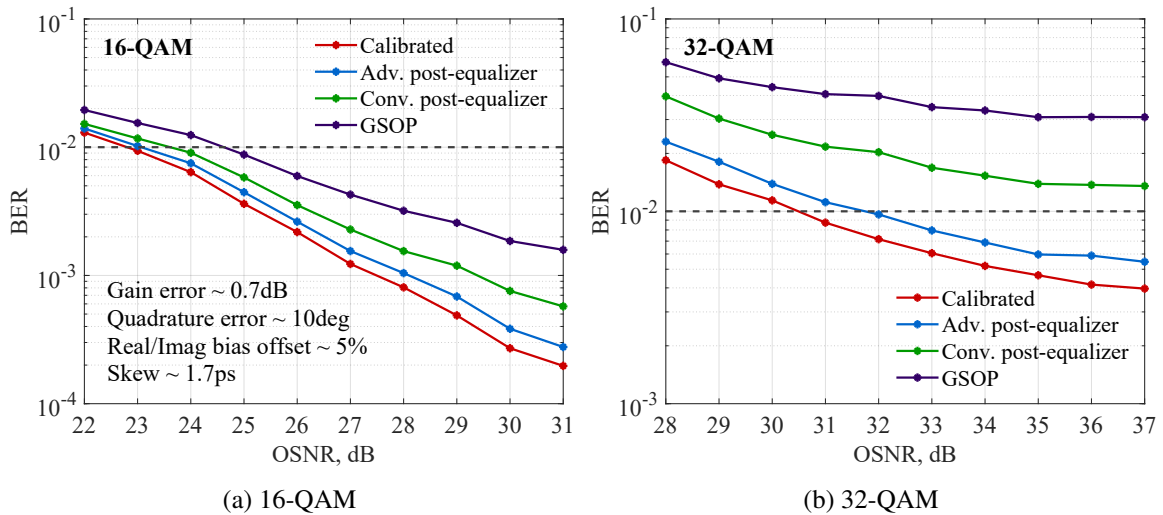
Fig. 3.10. BER vs OSNR in experiment at 40 GBd: (a) 16-QAM and (b) 32-QAM.

According to Fig. 3.10, the advanced post-equalization approach gives measurable performance improvement under the impact of multiple transmitter impairments compared to the other techniques under test. The approximate ROSNR penalty at BER=10^{-2} using advanced post-equalization is ~ 0.2 dB for 16-QAM and ~ 1.2 dB for 32-QAM. Significant

68

| | Before Post-EQ   After Post-EQ | | Before Post-EQ   After Post-EQ |

(a) Conventional post-equalizer   (b) Advanced post-equalizer
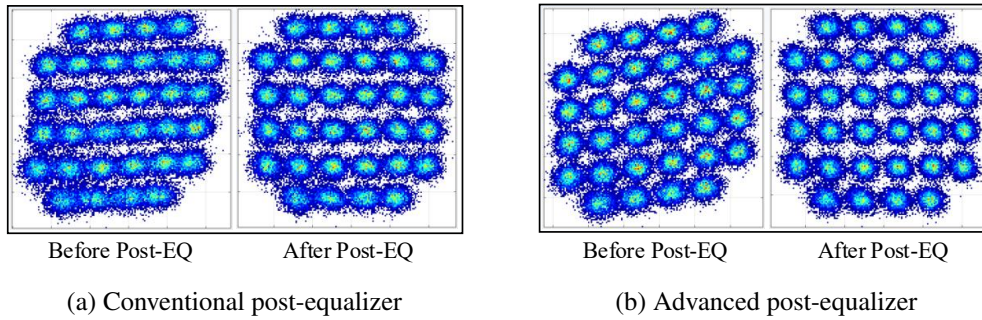
Fig. 3.11. Constellations of 32-QAM at 33 dB OSNR before and after (a) conventional post-equalizer, (b) advanced post-equalizer.

performance improvement is observed for 32-QAM where signal recovery at the desired BER threshold is only possible when advanced post-equalization is employed. Note that due to adaptive adjustment of the reference constellation for equalization and CPR, the signal quality is improved even before the post-equalizer, as shown in Fig. 3.11. It can be seen that adaptive reference constellation adjustment improves the robustness of adaptive equalization and CPR.

Summary

A receiver-side approach for mitigation of transmitter IQ impairments originating from imperfect modulation was demonstrated. Joint operation of equalizer, CPR and advanced post-equalizer provides robust recovery of signals with intrinsically impaired constellations. Performance improvement in comparison to other techniques was observed in numerical simulations and then validated experimentally for 16-QAM and 32-QAM signals at 40 GBd.

3.3.2   Receiver-Side Compensation of Transmitter IQ Cross-Talk

Electrical cross-talk between I and Q channels (IQ cross-talk) within MZMs in a transmitter due to high integration density may cause significant performance penalty, especially for systems operating at high symbol rates. Measured IQ cross-talk levels ranging from -30 dB to -20 dB for InP and SiP were reported previously in [102], [103]. Pre-compensation of IQ cross-talk at the transmitter was reported in [104], however accurate measurements of cross-talk must be obtained prior to effective compensation.

In the following, the performance degradation due to frequency-dependent electrical IQ cross-talk in a transmitter is characterized through numerical simulations for a practical case of transceiver operation. Then, the application of receiver-side post-equalization is extended for IQ cross-talk compensation and its performance is investigated. In Section 3.3.1, the

post-equalization technique was introduced to compensate for transmitter linear modulation impairments and IQ skew only.

Cross-Talk Penalty Characterization

IQ cross-talk originates from RF coupling effects due to the proximity of RF transmission paths within MZMs in highly compact photonic integrated circuits. IQ cross-talk can be described using the S-parameter formalism for four-port systems, which represents the frequency domain transfer functions for I and Q channels and coupling between them (see Fig. 3.12).
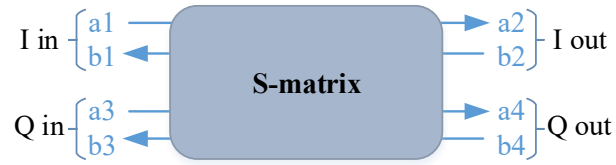
Fig. 3.12. Four-port system for IQ cross-talk representation.

Relationships between inputs and outputs of the system can be written as

$$a_2 = S_{21} \cdot a_1 + S_{23} \cdot a_3 \,, \tag{3.13}$$

$$a_4 = S_{41} \cdot a_1 + S_{43} \cdot a_3 \,. \tag{3.14}$$

The cross-talk is defined as

$$H_{\mathrm{XT}} = \frac{S_{41}}{S_{21}} = \frac{S_{23}}{S_{43}} \,. \tag{3.15}$$

Assuming a symmetrical system, Eq. 3.13 and Eq. 3.14 can be re-written using I and Q channel notation as

$$I_{\mathrm{out}} = H_{\mathrm{I}} \cdot (I_{\mathrm{in}} + H_{\mathrm{XT}} \cdot Q_{\mathrm{in}}) \,, \tag{3.16}$$

$$Q_{\mathrm{out}} = H_{\mathrm{Q}} \cdot (Q_{\mathrm{in}} + H_{\mathrm{XT}} \cdot I_{\mathrm{in}}) \,, \tag{3.17}$$

where H_{I} and H_{Q} are the transfer functions (frequency responses) of I and Q channels.

Four different levels of IQ cross-talk were considered for numerical simulations: -30 dB, -27 dB, -24 dB, -21 dB, as shown in Fig. 3.13. These levels represent integral cross-talk normalized for 64 GBd operation.

As illustrated in Fig. 3.13 (a), the magnitude response of IQ cross-talk grows rapidly from a relatively small value at low frequencies representing a logarithmic trend and saturates at

(a) Magnitude response   (b) Phase response
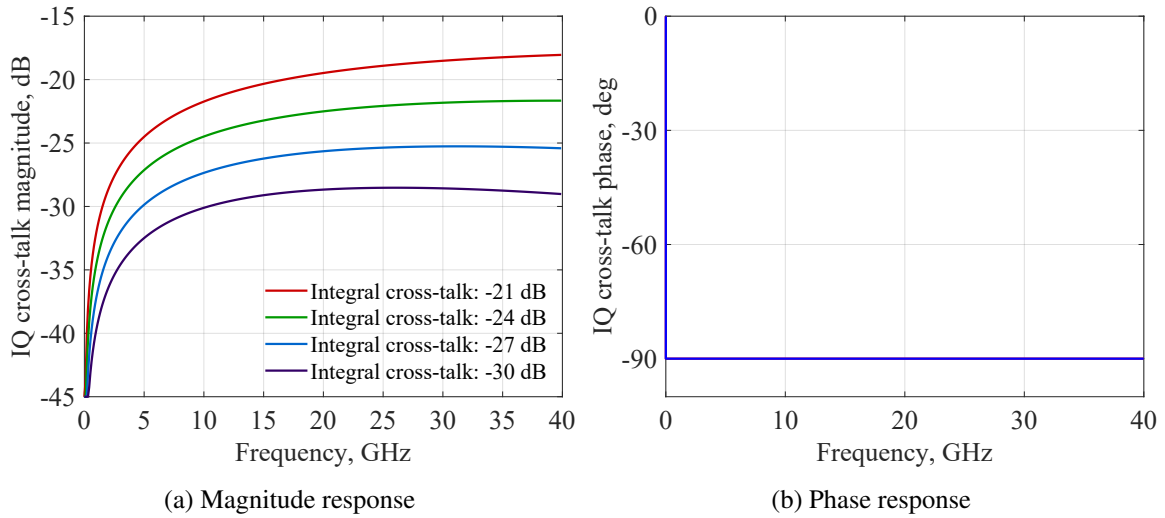
Fig. 3.13. Frequency response of IQ cross-talk used in numerical simulations (integral cross-talk levels normalized for 64 GBd operation): (a) magnitude response, (b) phase response.

high frequencies. IQ cross-talk levels and the generic shape used in our model are consistent with previously published results [102], [103]. The phase response (see Fig. 3.13 (b)) is modelled as a simplified constant 90° phase shift due to radiative coupling between transmission lines.

In the case of a 90° phase shift, the integrated IQ cross-talk acts as the additional signal noise contribution, which decreases the SNR budget of the system. Note that an actual measured phase response may deviate from a 90° shift, and depending on the shape of the phase response, cross-talk can be represented as a combination of signal noise and quadrature error.

Back-to-back transmission of DP 64-QAM and 32-QAM signals with RRC 0.2 roll-off pulse shaping at 64 GBd was numerically simulated. To consider a practical transmission case, a constant noise floor equivalent to the SNR level of 20 dB (best achievable link SNR) for 64 GBd operation was added to the system, which represents transmitter and receiver quantization noise, electrical noise and other impairments. To introduce the phase noise, the laser linewidth was set to 100 kHz for both transmitter and receiver sides. Performance was evaluated through generic DSP chain in Fig. 3.7 (without post-equalization).

Simulated BER versus OSNR curves for 64-QAM and 32-QAM in the presence of various IQ cross-talk levels without compensation are shown in Fig. 3.14. From Fig. 3.14 (a) it can be seen that for 64-QAM there is only small performance margin at the BER threshold of 2×10^{-2} (considering the practical noise floor) and performance degradation due to IQ cross-talk is substantial. IQ cross-talk of -30 dB leads to 3 dB OSNR penalty, while for higher levels of cross-talk the desired BER threshold is not achievable. For 32-QAM (see

Fig. 3.14. BER vs OSNR in numerical simulations without compensation for (a) 64-QAM and (b) 32-QAM at 64 GBd for -30, -27, -24, -21 dB IQ cross-talk levels.

Fig. 3.14 (b)), the performance degradation is less significant, being relatively negligible for -30 dB and -27 dB IQ cross-talk levels – less than 0.5 dB OSNR penalty; while for -24 dB and -21 dB IQ cross-talk levels, it is 1.5 dB and 4.5 dB penalty, respectively.

These observations suggest that in order to enable 64-QAM 64 GBd system operation, the design target would be to specify IQ cross-talk below -30 dB if no compensation is applied. For 32-QAM operation, the requirement is less stringent – IQ cross-talk should be below -30 dB to keep the performance penalty small.

Cross-Talk Post-Compensation

To compensate for transmitter IQ cross-talk at the receiver side, the post-equalization approach presented in the previous Section is employed. The DSP flow used for IQ cross-talk compensation is shown in Fig. 3.15, which represents the simplified structure presented in the previous Section (without adaptive reference constellation adjustment).

Prior to post-equalization, the signal is equalized using DD-LMS 2x2 MIMO adaptive equalizers, and the carrier is recovered using a BPS algorithm. The output of the equalizer is not down-sampled and CPR operates at 2 samples/symbol in order to enable fractionally-spaced post-equalization. Then, two DD-LMS 2×2 RV MIMO adaptive equalizers with 11 taps are used for post-equalization of I and Q signal components for each signal polarization, which allows compensation of frequency-dependent IQ cross-talk. Again, note that compensation of transmitter impairments is not achievable before the carrier is fully recovered, since transmitter I and Q signal components are mixed due to frequency offset and phase noise.
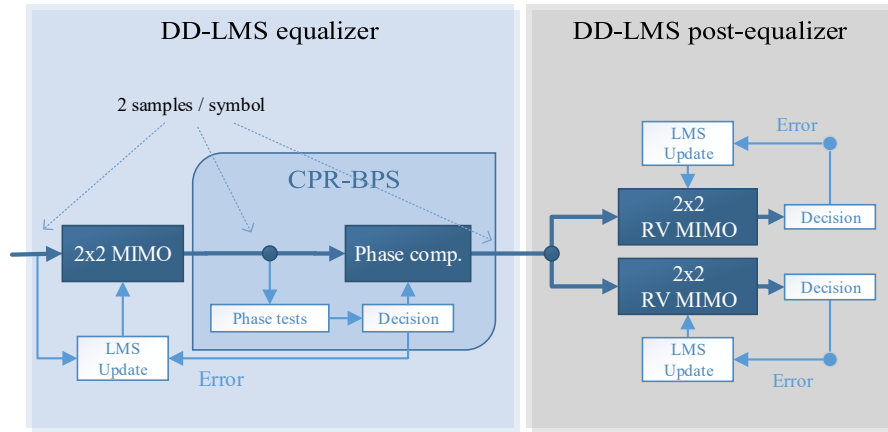
Fig. 3.15. Equalization structure for IQ cross-talk compensation.

Fig. 3.16 shows that IQ cross-talk compensation using post-equalization provides significant performance improvement. With post-compensation the tolerance to cross-talk for 64-QAM significantly increases, enabling signal recovery at the desired BER threshold of 2×10^{-2} for -27 dB, -24 dB and -21 dB IQ cross-talk levels. The OSNR penalty is less than 1 dB for -27 dB and -24 dB IQ cross-talk, and 5 dB for -21 dB IQ cross-talk. For 32-QAM, the OSNR penalty becomes negligible (less than 0.2 dB) for all cross-talk levels under consideration. The residual penalty after compensation is mainly associated with degraded performance of CPR and adaptive equalization under low SNR.
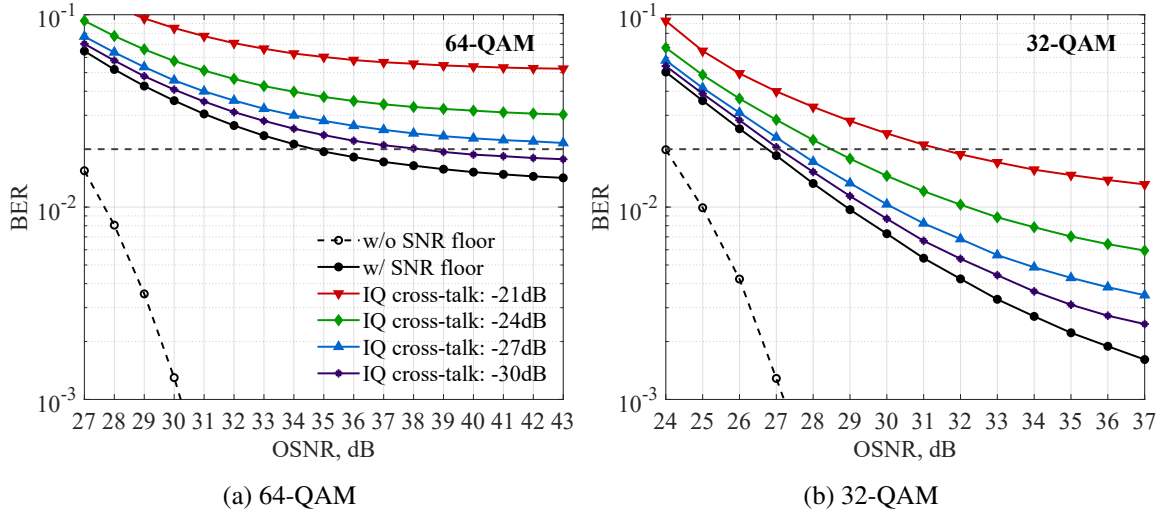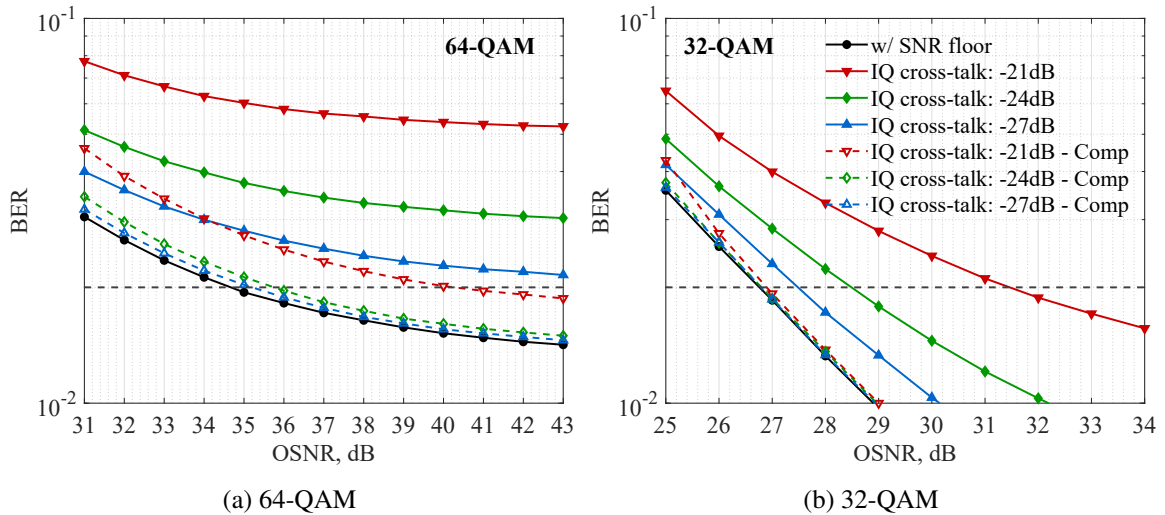

(a) 64-QAM

(b) 32-QAM

Fig. 3.16. BER vs OSNR in numerical simulations without and with compensation for (a) 64-QAM and (b) 32-QAM at -27, -24, -21 dB IQ cross-talk levels.

In order to allow adaptive equalizers to properly compensate frequency-dependent IQ cross-talk, a sufficient number of taps should be used, since the frequency resolution of

FIR filters scales accordingly. To compensate for the generic cross-talk frequency response in Fig. 3.13 only a few taps are required, as shown in Fig. 3.17, where little difference in ROSNR is seen if a filter with more than 11 taps are used. However, it should be noted that actual measured IQ cross-talk frequency responses tend to be rippled [103], [104], in which case more taps may be required.
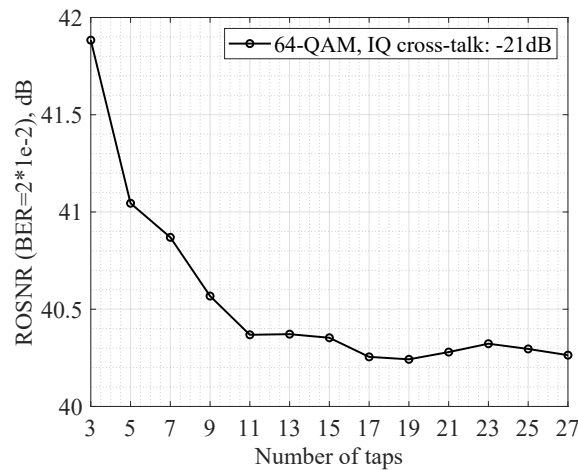
Fig. 3.17. Required OSNR at BER of 2×10^{-2} vs. number of post-equalizer filter taps for 64-QAM, IQ cross-talk of -21 dB.

A key advantage of the receiver-side post-compensation approach, as opposed to the transmitter-side pre-compensation proposed in [104] is that there is no need for IQ cross-talk measurements. FIR filters of the post-equalizer converge to the desired transfer function adaptively. Moreover, it is challenging to measure a frequency response for IQ cross-talk, since not only the magnitude response, but also the phase response must be obtained to enable accurate I/Q cross-talk compensation. Note that in [104] the phase response was tuned manually to obtain optimal cross-talk cancellation.

Summary

The combination of increased data rates and dense photonic integration makes electrical IQ cross-talk a potentially significant impairment in highly compact modern transceivers. The impact of IQ cross-talk on back-to-back system performance degradation which is, in particular, inherent for highly compact InP and SiP based transmitters, was numerically characterized. Considering practical limitations, a design target to keep the integral cross-talk below -30 dB was identified for 64-QAM 64 GBd system operation. This requirement can be relaxed by at least 6 dB with digital post-compensation, while for 32-QAM 64 GBd, the cross-talk penalty can be completely eliminated.

3.3.3 Generalization of Frequency-Dependent IQ Impairments Compensation and MIMO Pre-Emphasis

In Sections 3.3.1 and 3.3.2, the receiver-side post-equalization approach was shown to be an effective solution to mitigate transmitter IQ impairments. In particular, compensation of modulation impairments, IQ skews and electrical IQ cross-talk was considered. Another impairment which should be considered is uncompensated frequency response mismatch between I and Q channels, which can not be tolerated/recovered by conventional receiver DSP. For instance, it is expected that I and Q channels can have slightly different magnitude and phase responses, due to physical differences in RF routing paths.

In the following, the performance degradation caused by multiple frequency-dependent IQ impairments is studied and the application of receiver-side post-equalization is generalized. It is shown that under the impact of multiple severe impairments, the receiver DSP may fail to fully recover the signal, and only partial mitigation of frequency-dependent IQ imbalance is possible. Then, a MIMO pre-emphasis at the transmitter-side based on pre-trained adaptive post-equalizer filters is proposed and its advantage over a receiver-side compensation approach is demonstrated.

Performance Degradation Characterization

Transmitter IQ imbalance is simulated according to the diagram in Fig. 3.18, where $I(w)$ and $Q(w)$ are the I and Q signals in frequency domain, g_I and g_Q are the gain factors for I and Q signals, $H_I(w)$ and $H_Q(w)$ are the frequency-domain transfer functions (i.e. frequency responses) for I and Q signals, τ_I and τ_Q are the time delays for I and Q signals (the difference between them represents IQ skew), $H_{XT}(w)$ is the IQ cross-talk response, ϕ is the quadrature error. It is assumed that gain imbalance, skew and frequency response mismatch mainly originate from DACs, drivers and RF paths between them; cross-talk originates in RF paths within the inner MZM; then quadrature error occurs when I and Q signals are combined within the outer MZM.

In Section 3.3.1, it was shown that non-frequency selective imbalance (gain and quadrature error) can be effectively mitigated with negligible performance penalty by improving robustness of conventional adaptive equalization and CPR using adaptive reference constellation adjustment. Here, only frequency-dependent IQ imbalance is considered, which include IQ skew, IQ cross-talk, and frequency response mismatch between I and Q components.

To evaluate the performance degradation, back-to-back transmission of a DP 64-QAM signal with RRC 0.2 roll-off pulse shaping was numerically simulated. Transceiver back-to-back SNR of 20 dB was included to represent electrical and optical noise sources. Laser linewidth
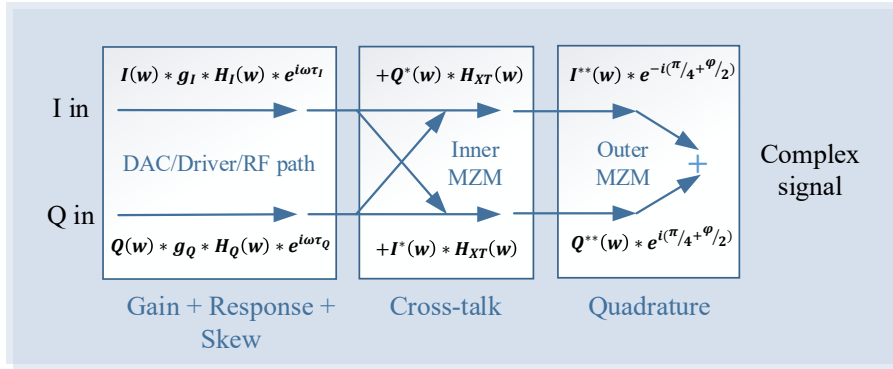
Fig. 3.18. IQ imbalance simulation diagram.

of 100 kHz was added to introduce phase noise. Signal processing was performed according to the generic DSP flow (See Fig. 3.7). Conventional complex-valued DD-LMS 2×2 MIMO equalization was performed in conjunction with CPR based on the BPS algorithm (unless otherwise stated, by default, the averaging filter is set to 75 symbols); post-equalization was done using DD-LMS 2×2 RV MIMO equalizers (the number of taps was set to 31, which is sufficient for optimal compensation of the impairments considered here).

Using the described simulation setup, first, the system performance degradation in terms of BER under the impact of the individual impairments was reviewed without any compensation. The considered impairments were IQ cross-talk of -27 dB and -24 dB (modelled according to Fig. 3.13), IQ skew of 0.5 ps and 1 ps, frequency response mismatch with integral mismatch of 0.3 dB in magnitude and $3°$ in phase. Frequency response mismatch was modelled as periodic ripples in magnitude and phase responses (see Fig. 3.21). From Fig. 3.19 (a) it can be seen that each individual impairment results in substantial performance degradation. At the BER threshold of 2×10^{-2}, IQ skew of 0.5 ps results in 2 dB OSNR penalty, frequency response mismatch results in 5 dB OSNR penalty, while under the impact of other impairments the desired performance is not achievable. These observations suggest that the transmitter must be precisely calibrated to enable 64-QAM 64 GBd operation.

Subsequently, the system performance degraded by combination of multiple impairments was studied. Here, it was considered that the impairments which may represent the typical uncompensated system condition may include IQ cross-talk of -27 dB, IQ skew of 1 ps, frequency response mismatch of 0.3 dB/$3°$. Also, the effectiveness of post-equalization compensation technique under the impact of severe impairments was investigated. Fig. 3.19 demonstrates the BER of the system as a function of OSNR under the impact of multiple impairments with and without compensation .

(a) Individual impairments without compensation

(b) Combined multiple impairments with and without receiver compensation
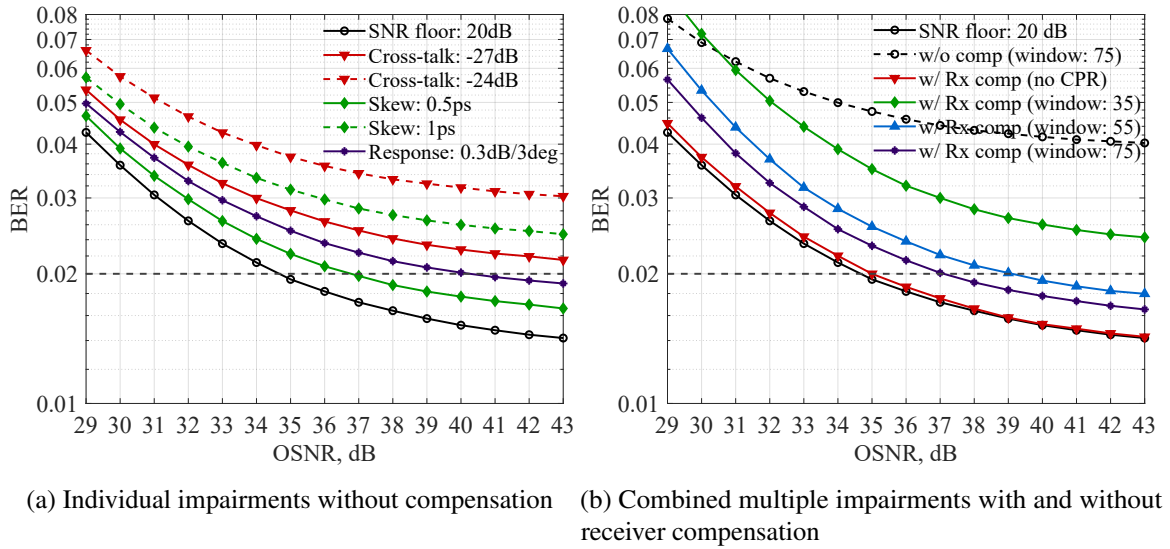
Fig. 3.19. BER vs. OSNR: (a) for individual impairments (without compensation), (b) for combined multiple impairments (IQ cross-talk: -27 dB, skew: 1 ps, response mismatch: 0.3 dB/3°) with and without receiver compensation

As discussed in the previous sections, signal recovery algorithms in the receiver DSP are highly sensitive to transmitter impairments. Since post-equalization takes place at the end of the DSP flow, it relies on the robustness of previous stages working with the uncompensated signal. One of the most critical DSP stages for high-order QAM signals is CPR. To investigate this aspect, the impact of the window length of the averaging filter for the BPS algorithm was investigated. Also, the laser phase noise (and, hence, CPR) was deliberately disabled to separate performance degradation from the impact of residual phase noise (due to imperfect CPR operation). According to Fig. 3.19 (b), when there is no phase noise in the system, after imbalance compensation the performance degradation is less than 0.5 dB at the BER of 2×10^{-2}; when phase noise is present, the penalty reduces with increased length of averaging filter —- for a filter length of 35 symbols, signal recovery is not achievable at BER threshold, while for a filter length of 75 symbols, the penalty is 2 dB. Without loss of generality, this shows that the weakest signal recovery stage is CPR - independently of the algorithm used, inferior performance of CPR is expected under lower SNR. Here, uncompensated IQ imbalance can be considered as an additional SNR degradation. In the case with no phase noise and CPR, the residual performance penalty is associated with other preceding DSP stages (e.g. clock recovery and equalization) and consequent imperfect post-equalization.

Transmitter MIMO Pre-Emphasis

To reduce complexity and improve robustness of receiver DSP, in the presence of substantial IQ imbalance it is beneficial to apply pre-compensation at the transmitter. A pre-emphasis using 2x2 RV MIMO equalizers is proposed (referred to as MIMO pre-emphasis). MIMO pre-emphasis enables compensation of the IQ coupling effect (e.g. cross-talk and quadrature error), as well as conventional IQ skew and frequency response compensation. The MIMO pre-emphasis structure is shown in Fig. 3.20, where each polarization is processed separately as for receiver-side post-equalization.
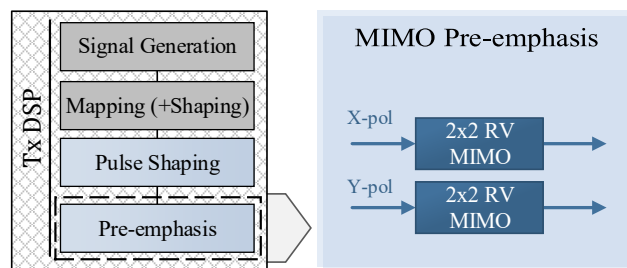
Fig. 3.20. Transmitter MIMO pre-emphasis.

Originally, MIMO pre-emphasis was suggested in [104] to pre-compensate for IQ cross-talk only. However, the IQ cross-talk was characterized by cutting one of the modulator arms and performing manual IQ cross-talk response measurements. Here, the pre-converged state of the adaptive 2x2 MIMO post-equalizer filters is proposed to be used for pre-emphasis at the transmitter. The post-equalizer converges to the inverse of the IQ imbalance response, hence, receiver-side post-equalizer filters can be directly used for pre-emphasis at the transmitter. The training stage can be performed in back-to-back under high OSNR using a QPSK training signal, which is highly robust to IQ impairments.

First, the accuracy of the IQ imbalance estimation by comparing the inverse response of the 2×2 RV MIMO adaptive post-equalizer filters with the modelled IQ imbalance response was investigated. Fig. 3.21 shows good agreement between the simulated and estimated IQ imbalance. I and Q filter pair represent frequency response mismatch and skew response, while Q-I and I-Q filters pair reflects cross-talk response (also, affected by frequency response mismatch and skew). Note that this approach allows estimation of individual impairments separately by decoupling the four filter responses, and it is particularly attractive for IQ cross-talk characterization, since both magnitude and phase response can be measured digitally without the use of special apparatus.

Second, pre-trained post-equalizer filters were applied for 2×2 RV MIMO pre-emphasis at the transmitter and the system performance under the same conditions as in Fig. 3.19 (b)
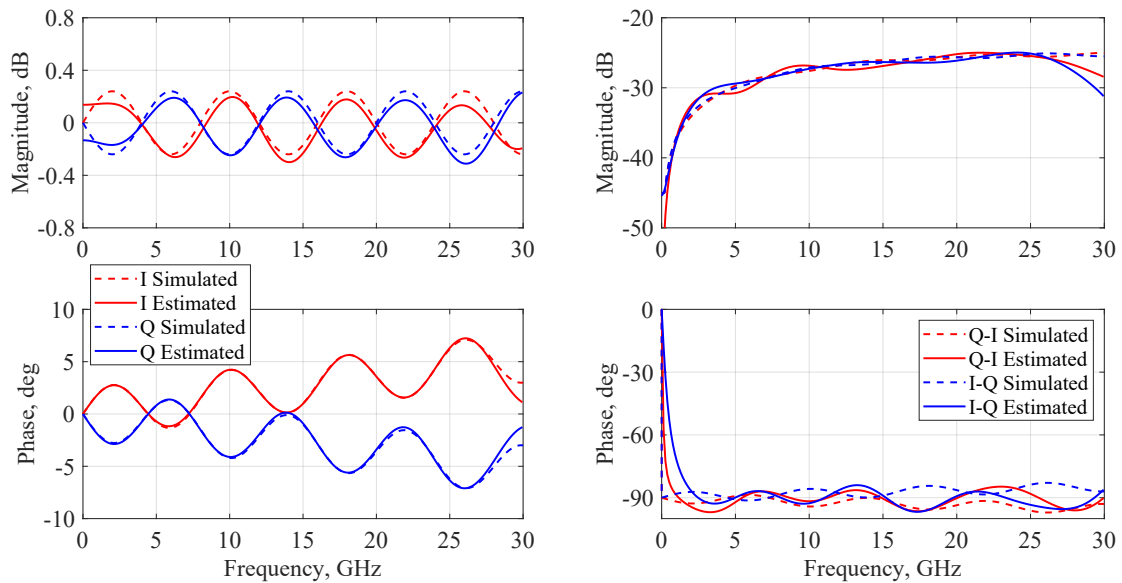
(a) Magnitude and phase response for I and Q filters (b) Magnitude and phase response for I-Q and Q-I filters

Fig. 3.21. Modelled response vs. estimated response (based on post-equalizer filters): (a) magnitude and phase response for I and Q filters, (b) magnitude and phase response for I-Q and Q-I filters
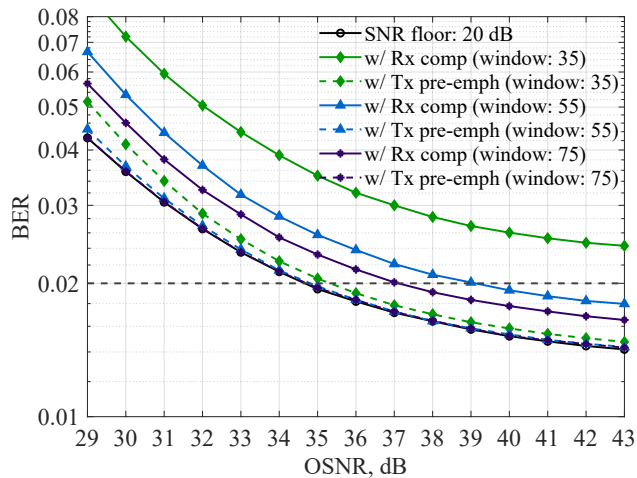
Fig. 3.22. BER vs. OSNR for combined multiple impairments with receiver compensation and transmitter pre-emphasis.

was studied. Fig. 3.22 shows the comparison of receiver-side post-equalization and transmitter MIMO pre-emphasis. It can be observed that transmitter pre-emphasis is superior to receiver-side compensation — for CPR averaging window length of 35 symbols, performance penalty is a few tenths of a dB compared to the case with no imbalance, while for window lengths of 55 and 75 symbols the penalty is negligible.

Summary

A practical case of transceiver operation under the impact of multiple frequency-dependent IQ impairments was studied via numerical simulations. It was shown that it is essential to compensate for IQ imbalance to enable system operation at high modulation order and high symbol rate, e.g. 64-QAM 64 GBd. A low-complexity MIMO pre-emphasis approach based on pre-trained adaptive filters from the receiver side was proposed and its superiority over receiver-side compensation under the impact of severe impairments was demonstrated.

3.4   Chapter Summary

In this Chapter, the importance of transceiver impairments compensation to enable the system operation with high-order modulation formats at high symbol rates was demonstrated. Multiple techniques to compensate for key transceiver impairments were investigated. These techniques may potentially relax the requirements for transceiver design and factory calibration.

In the first part, transceiver skew calibration techniques were demonstrated. First, the calibration algorithm for both transmitter-side and receiver-side skews based on receiver-side DSP was proposed. Two conditions are required for this algorithm: presence of frequency offset between transmitter and receiver, and SOP rotation. Sub-picosecond accuracy for IQ skew and picosecond accuracy for XY skew of the proposed algorithm were shown in numerical simulations. Then, the alternative calibration technique for transmitter IQ skews based on signal image spectrum measurement was proposed. Sub-picosecond accuracy of the technique was shown in numerical simulations and experiment.

In the second part, the impact of transmitter IQ impairments was considered and compensation techniques were demonstrated. First, advanced equalization structure within receiver DSP, which provides high tolerance to transmitter IQ impairments, was proposed. Two-fold tolerance improvement to gain and quadrature error, bias offsets and IQ skew was demonstrated both numerically and experimentally. Then, performance degradation due to transmitter electrical IQ cross-talk inherent in photonic integrated circuits was characterized. The application of the receiver-side post-equalizer was extended for IQ cross-talk compensation. It was demonstrated that the IQ cross-talk level requirement for 64QAM 64 GBd is reduced from -30dB to -24dB. Finally, the detrimental effect of multiple frequency-dependent IQ imbalance was analyzed via numerical simulations and the application of the post-equalizer was generalized. MIMO pre-emphasis based on pre-trained adaptive filters was proposed to compensate for joint impact of IQ cross-talk, IQ skew and frequency response mismatch.

Chapter 4

Advanced Coded Modulation: Probabilistic Constellation Shaping

In Chapter 3 transceiver performance optimization via DSP-based transceiver impairments mitigation was studied. This Chapter focuses on system performance optimization through application of advanced coded modulation techniques. In particular, some finite-length probabilistic constellation shaping techniques are introduced and system performance in the nonlinear fibre channel is investigated.

This Chapter is based on the original published contributions: [**P.6**], [**P.7**]. Also, original unpublished material is included.

4.1   Introduction

In recent years, probabilistic constellation shaping became an important part of the coded modulation (CM) paradigm. It has evolved from a topic of academic interest [68] to a realizable technology [105], [106]. The drivers of this adoption have been partly increased noise tolerance and partly the increased rate flexibility that can be provided by tuning the shaping rate, while maintaining constant FEC code rates and symbol rates of the system [107]. More recently, short-length shaping [108], [109], low-complexity shaping [110], [111] and nonlinearity mitigating shaping architectures [112] have become active research topics.

In general, constellation shaping may be considered as the optimization of transmitted symbols distribution in terms of either location (geometrical constellation shaping) or probability (probabilistic constellation shaping) in the signal space, such that the transmitted signal has improved power efficiency or nonlinear tolerance for an optical channel. In the

additive white Gaussian noise (AWGN) channel, constellation shaping provides a gain of up to 1.53 dB in power efficiency over uniform signaling [67].

Probabilistic constellation shaping is of interest in this Chapter. In particular, the focus is on system nonlinear performance analysis of the specific class of practical probabilistic constellation shaping algorithms – namely, sphere shaping – in long-haul multi-span links and extended-reach single-span links.

First, Section 4.2 introduces the concept of probabilistic amplitude shaping (PAS), and then gives the overview of shaping schemes under investigation, multi-dimensional symbol mapping strategies, associated energy efficiency and rate loss of shaping/mapping schemes. In Section 4.3 the nonlinear performance of the system employing sphere shaping was investigated in long-haul multi-span transmission and extended-reach single-span transmission. Section 4.4 provides the analysis of Huffman-coded sphere shaping (HCSS) in extended-reach single-span links.

4.2   Probabilistic Constellation Shaping

Since coherent optical communication systems allow utilization of all physical properties of the optical field, 4D signal space is inherently available for modulation. The most common approach is to treat those dimensions independently — 4D signal space can be decomposed into lower dimensional components. For instance, DP QAM formats can be treated as two independent QAM formats in both polarizations or four amplitude-shift keying (ASK) formats in each quadrature.

By considering the optical field as a 4D signal space, power efficiency may be improved in a number of ways (e.g., by considering constellation points on an optimal lattice bound by a maximum power) [113], [114]. High-dimensional modulation based on utilization of multiple time-slots (consequent transmitted symbols) or multiple carriers to utilize more efficient lattices in larger numbers of dimensions can provide further improvement in power efficiency [115], [116]. However, coded performance using binary FEC codes and bit-interleaved coded modulation (BICM) implementation for such systems may be challenging due to their lack of Gray-coded bit labeling. Additionally, while much research in this area has focused on power efficiency, several proposed high-dimensional modulation techniques specifically target improved nonlinear tolerance in the optical fiber channel [117]–[119].

Finite-length probabilistic shaping may be considered as high-dimensional modulation — i.e., the mapping of a block of input bits to a point on an high-dimensional constellation (e.g., on a square lattice), where an high-dimensional constellation point is then mapped to a constituent 4D constellation (e.g sequence of DP M-QAM symbols in time) [120]. Note

that such mapping of equiprobable high-dimensional constellation points to a constituent 4D constellation results in non-uniform distribution of transmitted 4D symbols.

The key enabler for active research and adoption of probabilistic constellation shaping in practical systems was the introduction of a PAS framework for QAM [68]. PAS is based on reverse concatenation of the shaping stage and FEC, which allows the use of binary FEC and enables transmission rate adaptivity with fixed FEC code rate. Since the proposal of PAS, many implementations utilizing this structure have been introduced and investigated.

In this Section, first, the overview of the PAS framework is given. Then, common shaping architectures for the PAS framework are briefly discussed followed by a more detailed description of Maxwell-Boltzmann (MB) shaping and sphere shaping schemes. Also, multi-dimensional mapping strategies and energy efficiency and associated rate loss of the shaping schemes are discussed.

4.2.1 Probabilistic Amplitude Shaping

The diagram of PAS architecture at the transmitter and receiver is shown in Fig. 4.1.

(a) Transmitter
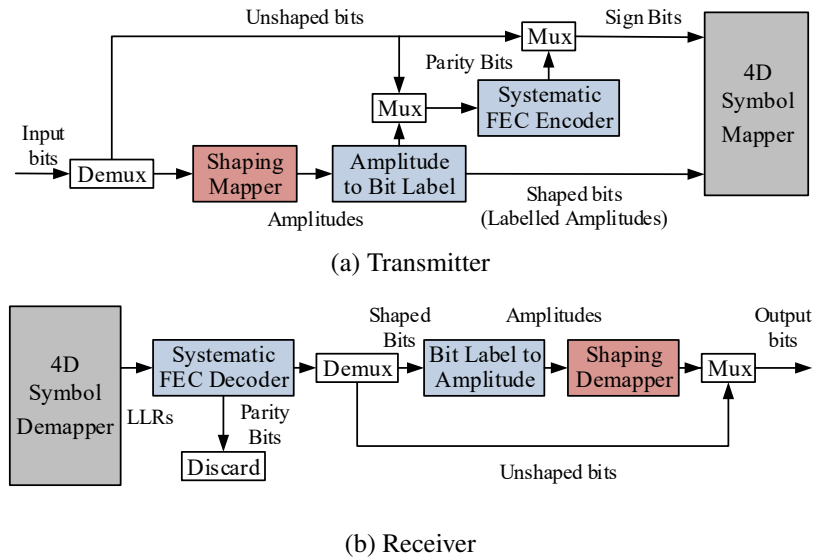
(b) Receiver

Fig. 4.1. PAS architecture at the transmitter and receiver.

The PAS structure calls for blocks of uncoded information bits to be mapped onto probabilistically shaped amplitude sequences [68]. The bits corresponding to the labels of the shaped amplitudes (typically, Gray labelling is used) are then encoded with a systematic FEC code. The parity bits generated by the FEC code are then assigned to the sign bits of the pulse amplitude modulation (PAM) constellation. Some uncoded information bits (referred to as unshaped bits) may be also carried on the signs of the constellation if required. Note

that, parity bits and information bits are uniformly distributed, hence, resulting encoded distribution is symmetric about zero. After that, these signed amplitudes are mapped onto the 4D optical carrier for transmission.

The primary advantage of the PAS architecture is that the FEC decoder operates on the bit labels of the shaped amplitude sequences at the receiver, enabling FEC decoding to be performed before shaping demapping. The demapping is then performed on amplitudes which are presumed to be error free, greatly reducing the complexity of both the demapping procedure and the shaping system design. Also, another useful feature of PAS is that the overall transmission rate may be tuned by adjusting the rate of the shaping algorithms, while the FEC code rate remains the same.

The key elements of the PAS architecture are the shaping mapper at the transmitter-side and shaping demapper at the receiver-side. The set of available unique amplitude sequences, which forms a high-dimensional constellation and can be used for mapping/demapping blocks of bits, is defined by the shaping architecture. Shaping architecture determines the energy efficiency and rate loss of the system. Mapping and demapping algorithms for a shaping architecture determines the implementation complexity.

Shaping Rate

The shaping rate for PAS is defined in bits per amplitude (bits/Amp) as

$$R_{\mathrm{S}} = \frac{k}{L}, \tag{4.1}$$

where k is the number of uniform input bits, and L is the length of the shaped amplitude sequence. Note that shaping rate is defined in 1D (per unsigned amplitude).

Net Data Rate

The net data rate of the system employing uniform signaling is given by

$$R_{\mathrm{Tx,Uni}} = m \cdot R_{\mathrm{FEC}}, \tag{4.2}$$

where R_{FEC} is the FEC code rate; m is the number of bits/symbol, which can be encoded to a constellation symbol (as shown in Chapter 2, Section 2.3.4, $m = \log_2 M$, where M is the modulation order). Note that $R_{\mathrm{Tx,Uni}}$ may represent the data rate per high-dimensional symbol (e.g. 2D- or 4D-symbol).

For the PAS architecture the net data rate can be expressed as [68], [121]

$$R_{\text{Tx,PAS}} = D \cdot (R_{\text{S}} + 1) - m \cdot (1 - R_{\text{FEC}}), \tag{4.3}$$

where D is the symbol dimensionality (e.g. for DP M-QAM, D=4), in the first term "1" accounts for the sign bit per dimension, and the second term accounts for the parity bits of systematic FEC code.

Eq. 4.3 shows that the data rate of the system employing PAS architecture may be varied by adjusting the shaping rate and keeping the fixed FEC code rate. The lower bound on the FEC code rate is given by

$$R_{\text{FEC}} = \frac{m - D}{m}, \tag{4.4}$$

since at most D out of m bits can be used as parity bits for the systematic FEC code. Note that Eq. 4.4 is applicable to M-QAM formats, where $M > 4$.

4.2.2 Shaping Architectures

Significant research has been made in shaping architectures for the PAS framework since its original proposal. Initially, an analysis based on an asymptotically infinite-length shaping approach with an ideal Maxwell-Boltzmann (MB) distribution of amplitudes was commonly performed for transmission over a nonlinear optical channel. However, infinite-length MB shaping is not feasible for hardware implementation, since it requires infinite-length mapping and demapping algorithms.

Recently, research has focused on finite-length shaping architectures which can be realizable in the hardware. One class, referred to as distribution matching (DM), is based on obtaining a fixed target distribution. First, constant-composition DM (CCDM) was introduced [122], whereby all transmitted amplitude sequences are permutations of a single composition, defined by the target distribution. While CCDM can provide asymptotically low rate-loss, and therefore high power efficiency, it requires long sequences (typically on the order of several hundred amplitudes) to achieve it. Multiset-partition DM (MPDM) was proposed in [108], [123] and provides lower rate loss at a fixed shaping sequence length. MPDM is based on multiple complimentary compositions, which on average result in the desired distribution. Other DM implementations were also proposed, such as product DM [124], hierarchical DM [125], prefix-free code DM [122], and parallel-amplitude DM [126].

Another class of shaping algorithms is based on introducing an optimal sphere bound in multi-dimensional signal space, which is referred to as sphere shaping – for a target transmission rate and finite shaping length, sphere shaping offers the optimal energy efficiency

[120], [127]. Sphere shaping-based algorithms include shell mapping (SM) [128], [129], enumerative sphere shaping (ESS) [109], [130], [131], and Huffman-coded sphere shaping (HCSS) [132], [133].

In the following, MB shaping, sphere shaping and HCSS are described. Further, symbol mapping strategies and power efficiency with associated rate loss are discussed.

Maxwell-Boltzmann Shaping

Probabilistic constellation shaping with MB distribution was shown to be capacity-achieving for linear channels [67] – it achieves the maximum power efficiency for a given entropy.

Discrete MB distribution for the amplitudes a is given by

$$P_A(a) = \frac{e^{-\nu|a|^2}}{\sum_{a_j \in \mathscr{A}} e^{-\nu|a_j|^2}} \,, \tag{4.5}$$

where ν is the shaping factor (scaling parameter), which controls the entropy and corresponding resulted distribution of amplitudes. In the context of this Chapter, the entropy of the amplitudes with MB distributions is assumed to be equivalent to the shaping rate in the case of infinite-length MB shaping.

Sphere Shaping

Sphere shaping introduces an optimal sphere bound in multi-dimensional signal space — for a target transmission rate and finite sequence length, the optimal set of constellation points from a fixed lattice is chosen such that the geometry is bounded by a hyper-sphere (introducing a certain energy constraint) [120], [127]. By definition, this scheme achieves optimal power efficiency — for a given rate (i.e. required number of constellation points / amplitude sequences), lattice (e.g. square lattice) and number of dimensions (i.e. amplitude sequence length), a smallest possible sphere, which contains the required number of points, can be defined. Any alternative set of constellation points will contain points outside the sphere, leading to degraded power efficiency. Examples of algorithms, which represent pure sphere shaping, are SM and ESS.

Let us denote the amplitudes by $a_i \in \mathscr{A}$, where $\mathscr{A} = \{a_1, a_2, \ldots, a_{|\mathscr{A}|}\}$ is the alphabet of amplitudes and $|\mathscr{A}|$ is the length of the alphabet. Then, $a_l^L = [a_{l_1}, a_{l_2}, a_{l_3}, \ldots, a_{l_L}] \in \mathscr{A}^L$ denotes the sequence of L amplitudes, where $\mathscr{A}^L$ (L-fold Cartesian product of $\mathscr{A}$ with itself) is the alphabet of amplitude sequence of length L.

The set of constellation points (amplitude sequences a^L) defined by the sphere shaping architecture can be expressed as

$$\mathscr{A}^* = \left\{ a_{l_1}, a_{l_2}, a_{l_3}, \ldots, a_{l_L} \middle| \sum_{i=1}^{L} a_{l_i}^2 \leq P \right\},\tag{4.6}$$

where P is the energy constraint. For a certain target shaping rate $R_S = k/L$, P is chosen as the minimum energy for which at least 2^k sequences are available with energy equal to or less than P.

For simplicity of consideration, each amplitude sequence from $\mathscr{A}^*$ can be seen as a permutation of a composition. The composition represents a multiset of amplitudes — a set of amplitudes where each amplitude can occur more than once. The number of occurrences of each amplitude defines the composition as $C = \{c_1, c_2, \ldots, c_{|\mathscr{A}|}\}$, where c_i is the number of instances of amplitude a_i in the shaped amplitude sequence of length $L = \sum_{i=1}^{|\mathscr{A}|} c_i$. Note that all permutations of the composition have identical energy $E(C) = \sum_{i=1}^{|\mathscr{A}|} c_i a_i^2$.

Since the set of all compositions $\mathscr{C}$ may be generated relatively simply given the fixed length of the amplitudes alphabet (fixed cardinality), construction of the spherical structure may be simplified into the task of finding all compositions under the energy constraint P. This can be expressed as

$$\mathscr{C}^* = \left\{ C_i \middle| E(C_i) \leq P \right\}.\tag{4.7}$$

The number of available sequences for the ith composition in the spherical structure is given by the multinomial coefficient as

$$N_{\text{seq,SS}}^i = N_{\text{perm}}^i = \frac{L!}{\prod_{k=1}^{|\mathscr{A}|} (c_k^i!)},\tag{4.8}$$

where c_k^i is the number of occurrences in the ith composition of the amplitude a_k. Note that $\sum_{C \in \mathscr{C}^*} N_{\text{seq,SS}} \geq 2^k$, hence, only part of the available sequences from the highest energy composition $C \in \mathscr{C}^*$ may be used.

The probability of the ith composition in the spherical structure is given by

$$p_i = \frac{N_{\text{seq,SS}}^i}{2^k}.\tag{4.9}$$

Huffman-Coded Sphere Shaping

HCSS introduces some additional structure into a spherical shaping architecture in exchange for a small reduction in power efficiency. In particular, HCSS restricts the number of constellation points utilized for each unique composition to be a power of two, and then introduces a minimal number of additional compositions with higher power to ensure a

dyadic distribution of compositions [132]. This enables the use of a variable length binary prefix (Huffman code) to uniquely address compositions in the shaping architecture. The remaining payload bits in a binary input word are then used to address a unique permutation (i.e. amplitude sequence) of the specified composition. Therefore, the mapping problem can be divided into two parts: addressing composition by Huffman-coded tree and CCDM mapping/demapping.

(a) HCSS Mapper (b) HCSS Demapper
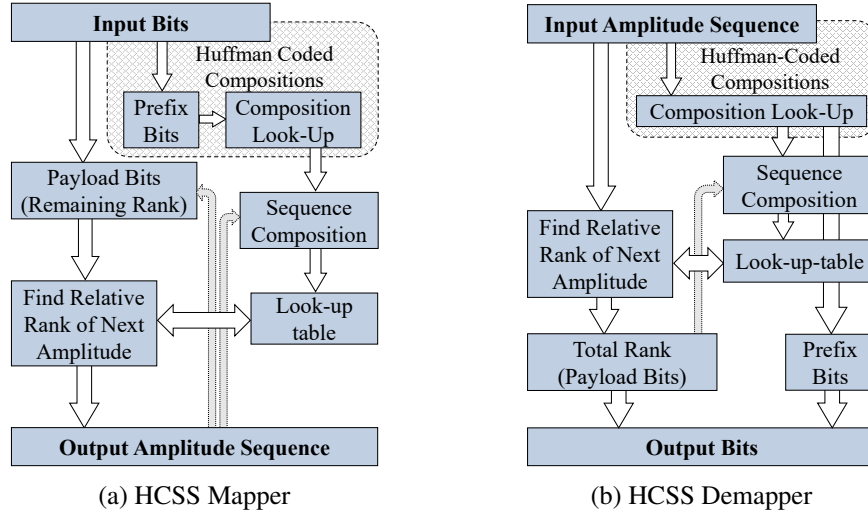
Fig. 4.2. Block diagram of HCSS algorithm using multiset ranking and LUT.

A multiset ranking (MR) algorithm can be used for CCDM mapping/demapping as described in [132], [133] — in that case, the lexicographical rank of the selected sequence corresponds to the payload bits. Additionally, it should be noted that sequence ranks may be computed without multiplication operations by pre-computing multinomial coefficients and storing them in a look-up table (LUT). For short sequence lengths, the coefficients required for MR mapping and demapping can be stored in moderately sized LUTs — for example, the sequence length of 32 requires only 100 kbits of the memory [133]. Therefore, both mapping in Fig. 4.2 (a) and demapping in Fig. 4.2 (b) are performed iteratively on a per-symbol basis, using LUTs, requiring integer comparison and addition operations only.

The number of available sequences for the ith composition in the Huffman-coded spherical structure is

$$N_{\text{seq,HCSS}}^i = 2^{\lfloor \log_2 N_{\text{perm}}^i \rfloor}, \tag{4.10}$$

where N_{perm}^i is the number of possible permutations of the ith composition given by Eq. 4.8. The probability of the ith composition is therefore given by:

$$p_i = \frac{N_{\text{seq,HCSS}}^i}{2^k}. \tag{4.11}$$

Symbol Mapping Strategies

Three strategies for mapping shaped sequences of amplitudes into the modulated 4D symbols of the DP 64-QAM format (referred to as 1D, 2D and 4D mapping) were studied. These mapping strategies are illustrated in Fig. 4.3. Note that a sign is assigned to each amplitude according to the sign bit during the mapping process (see Fig. 4.1 (a)), however, added signs are not reflected in Fig. 4.3 for simplicity of consideration.

In the case of 1D symbol mapping, four independently shaped amplitude sequences of length L are sequentially (on an amplitude-by-amplitude basis) mapped into four simultaneous quadratures (in-phase and quadrature signal components in both polarizations) constructing a single 4D-symbol sequence of length L, as shown in Fig. 4.3 (a).
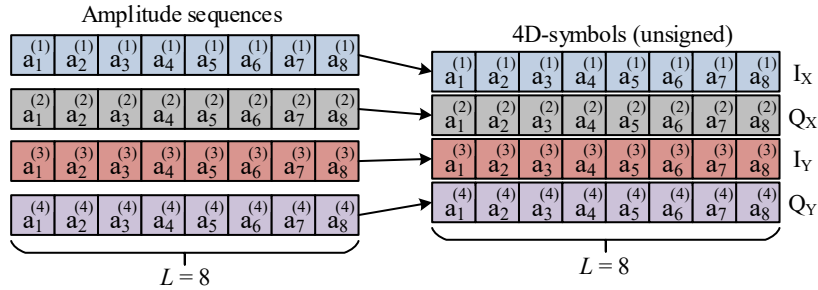
(a) 1D symbol mapping
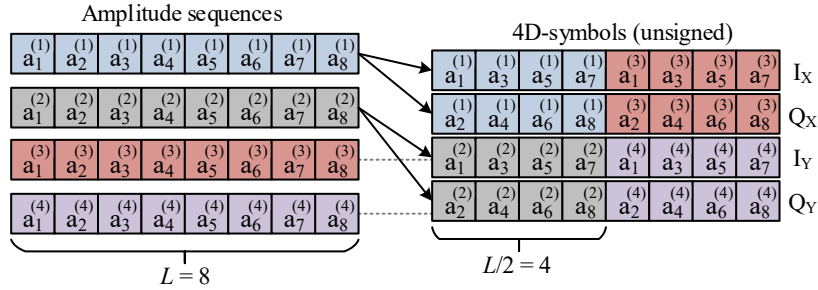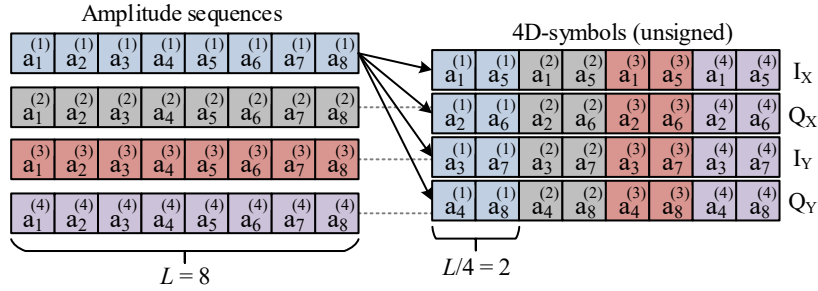
(b) 2D symbol mapping

(c) 4D symbol mapping

Fig. 4.3. Strategies for mapping amplitude sequences into modulated 4D symbols (added signs are not reflected): (a) 1D symbol mapping, (b) 2D symbol mapping, (c) 4D symbol mapping.

In the case of 2D symbol mapping, as shown in Fig. 4.3 (b), two independently shaped amplitude sequences of length L are mapped into a single 4D-symbol sequence of length $L/2$ — two consecutive amplitudes from each amplitude sequence are mapped into four simultaneous quadratures.

In the case of 4D symbol mapping, as shown in Fig. 4.3 (c), a single shaped amplitude sequence of length L is mapped in a single 4D-symbol sequence of length $L/4$ — four consecutive amplitudes are mapped into four simultaneous quadratures.

By increasing symbol mapping dimensionality, the time-domain length of the output 4D-symbol sequence and the number of simultaneously interacting sequences can be effectively reduced, while the power efficiency is kept constant. The derivation of the resulting multi-dimensional PMF for different symbol mapping strategies is described in detail in Appendix A.1. It is important to note that 1D, 2D and 4D mapping strategies result in 1D, 2D and 4D distributions, respectively.
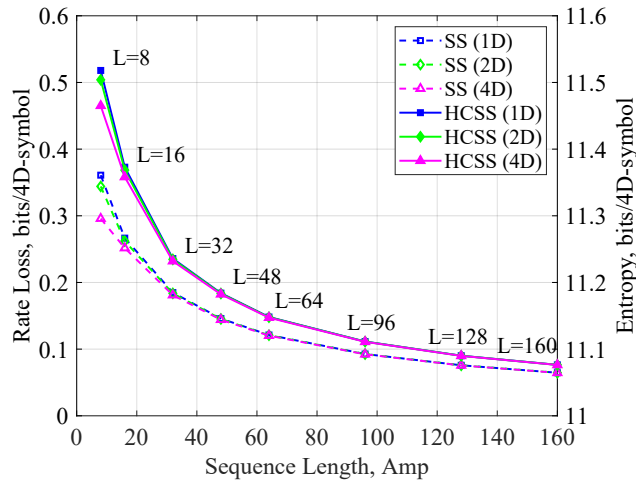
Fig. 4.4. Rate loss and entropy vs. shaping sequence length ($R_S = 1.75$) for 1D, 2D and 4D symbol mapping strategies.

Rate Loss and Power Efficiency

Rate loss due to the use of a finite-length shaping scheme is calculated in bits per 4D-symbol (bits/4D-symbol) as

$$R_{\text{loss}} = \text{H}(X) - D \cdot (R_S + 1), \tag{4.12}$$

where $\text{H}(X)$ denotes the entropy of the 4D output signal X (calculated according to PMF in Appendix A.1), D accounts for mapping dimensionality ($D = 4$) and "1" accounts for the sign bit per dimension. Note that for infinite-length MB shaping there is no rate loss ($R_{\text{loss}} = 0$).
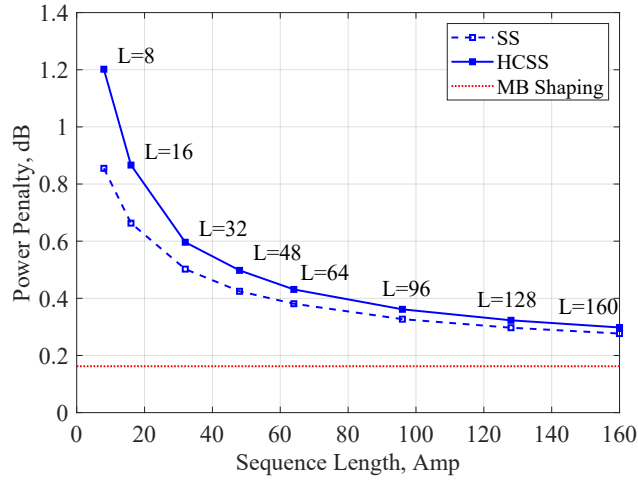
Fig. 4.5. Power penalty vs. shaping sequence length ($R_S = 1.75$). Reference level is the MB shaping with unconstrained cardinality.

Fig. 4.4 demonstrates the rate loss and corresponding entropy for sphere shaping and HCSS with 1D, 2D and 4D mapping strategies based on DP 64-QAM at the shaping rate of $R_S = 1.75$. As mentioned previously, HCSS has slightly higher rate loss compared to the conventional sphere shaping due to additional constraints introduced in the spherical structure. This difference becomes negligible at long shaping lengths. Also, note that higher dimensional mapping offers slightly reduced rate loss at short shaping lengths both for sphere shaping and HCSS.

Fig. 4.5 shows the power penalty for sphere shaping, HCSS and infinite-length MB shaping (also, using DP 64-QAM) at the shaping rate of $R_S = 1.75$. The power penalty was calculated with respect to the MB distribution with unconstrained cardinality, which provides the maximum power efficiency for a given entropy [127]. HCSS and sphere shaping demonstrate the similar trend as for the rate loss — the difference in power penalty becomes negligible at long shaping lengths. Note that for HCSS and sphere shaping power efficiency does not depend on symbol mapping dimensionality.

4.3 Nonlinear System Performance Analysis in Numerical Simulations

As mentioned in Section 4.2.2, an analysis based on infinite-length MB shaping was commonly performed for transmission over a nonlinear optical channel. MB shaping achieves the maximum power efficiency for a given entropy, which is therefore the optimal distribution in the AWGN channel [127]. However, for an optical channel, MB shaping can enhance fibre

Kerr nonlinearities, leading to a decrease in shaping gain, which was shown for long-haul transmission [134] and unrepeated transmission [135]. Importantly, while considerable performance improvement can be achieved using infinite-length MB shaping, as mentioned previously, this approach is fundamentally impossible to implement.

Recently, the nonlinear performance of finite-length shaping algorithms was an active research topic. The dependence of nonlinear tolerance on shaping length was investigated using CCDM [136], [137] and ESS [131], [138] for multi-span long-haul links. Also, the advantage of 2D symbol mapping for nonlinearity tolerance has been mentioned previously [137], while the advantage of the short-length shaping regime for a nonlinear optical channel was theoretically investigated in [139], [140]. Significant shaping gain exceeding the theoretical gain for the AWGN channel was demonstrated in numerical simulations for single-span links by optimally combining linear and nonlinear shaping gains using SM with very short shaping lengths [140]. In [141], [142] the authors investigated shaping of a single 4D quadrant using SM and demonstrated increased nonlinear tolerance in single-span links.

In this Section, an extensive nonlinear performance analysis for sphere shaping is performed via numerical simulations. Multi-span long-haul transmission links and extended-reach single-span links are considered.

4.3.1   Numerical Simulations Framework

Fibre-optical transmission links were numerically simulated using a full-field split-step Fourier method (SSFM) [143], [144]. The SSFM is a numerical approach for solving the Manakov model equations [145], [146], which were used to represent signal transmission through the optical fiber with linear and nonlinear impairments discussed in Chapter 2, Section 2.2.2. The Manakov model serves as the approximation of generalized coupled nonlinear Schrödinger equations with the averaged impact of the polarization-related effect (i.e. modal birefringence).

The general parameters of the simulated systems are listed in Table 4.1. WDM transmission of 9 DP 64-QAM channels over standard SMF (SSMF) was numerically simulated. The channel under test was the central channel. All channels were generated randomly and independently using the same signaling scheme under test.

At the receiver side, first, chromatic dispersion (CD) was digitally compensated. Then, the central channel was selected with the matched filter and bulk phase compensation was applied (to compensate for the constant phase shift, which may occur in the system). Note that laser phase noise and PMD effects were excluded from the simulated model, since these effects have negligible impact on the nonlinear performance of the system under consideration.

Table 4.1. Simulation Parameters

Parameter	Value
Modulation Format	DP 64-QAM
Symbol Rate	28 GBd
Pulse Shaping	Nyquist
Number of Channels	9
Channel Spacing	30 GHz
Nonlinear Coefficient	1.3 1/W/km
Dispersion Coefficient	16 ps/nm/km
Fiber Attenuation	0.2 dB/km
Amplification	Lumped (EDFA)
Noise Figure	4 dB
SSFM Step-size	0.1 km
Oversampling Factor	32

Lumped amplification (e.g. EDFA) was assumed for the transmission links, ASE noise was added according to the specified noise figure. Two types of links were simulated — a long-haul multi-span link and an extended-reach single-span link.

Performance Metrics

The system performance analysis was performed using two metrics: effective SNR and AIR.

The effective SNR [134] of the received signal is calculated as

$$\text{SNR}_{\text{eff}} = \frac{\text{Var}[X]}{\text{Var}[Y-X]},\qquad(4.13)$$

where $\text{Var}[\cdot]$ denotes the variance, transmitted signal and received signal are denoted by X and Y. Note that effective SNR accounts for both linear and nonlinear noise contributions accumulated during signal propagation over an optical fiber.

The AIR for BICM impacted by the rate loss associated with finite-length shaping [108] is calculated in bits/4D-symbol as

$$\text{AIR} = \underbrace{\left[\text{H}(X) - \sum_{i=1}^{m} \text{H}(B_i|Y) \right]}_{\text{GMI}} - R_{\text{loss}},\qquad(4.14)$$

where GMI is calculated using Monte-Carlo approach according to Eq. 2.41 (Chapter 2, Section 2.5.3). Note that for both uniform signaling and infinite-length MB shaping $R_{\text{loss}} = 0$ and AIR is given by the GMI only.

LLRs for binary labels B_i $(i = 1, \ldots, m)$ are calculated by the soft-demapper as

$$\text{LLR}_i = \log \frac{\sum_{x \in \mathscr{X}_{1,i}} f_{Y|X}(y|x) P_X(x)}{\sum_{x \in \mathscr{X}_{0,i}} f_{Y|X}(y|x) P_X(x)}, \tag{4.15}$$

where $\mathscr{X}_{1,i}$ and $\mathscr{X}_{0,i}$ are the subsets of constellation $\mathscr{X}$, which represent B_i being equal to 1 or 0, respectively; $f_{Y|X}(y|x)$ is the transition probability density function of the auxiliary channel used for mismatched decoding; $P_X(x)$ is the 4D PMF (calculated according to Appendix A.1).

A memoryless 4D circularly symmetric Gaussian auxiliary channel is considered and it is assumed that the noise in each dimension is independent and identically distributed [147]. In this case, the channel can be described as

$$f_{Y|X}(y|x) = \frac{1}{(\pi\sigma^2)^2} \exp\left(-\frac{\|y - x\|^2}{\sigma^2}\right), \tag{4.16}$$

where σ^2 is the noise variance. Note that lower-dimensional soft-demapping can be done analogously for the case of 1D and 2D mapping.

4.3.2 Performance of Sphere Shaping in Long-Haul Multi-Span Links

In the following, the nonlinear performance of sphere shaping in long-haul transmission was studied in comparison with uniform signaling and infinite-length shaping with an ideal MB distribution. In particular, the impact of shaping length, dimensionality of symbol mapping, and shaping rate on nonlinear tolerance was investigated.

Simulated System

A long-haul transmission link consisting of 30 spans of 100 km SSMF (in total 3000 km) was simulated. After each span the loss of the fiber was ideally compensated (i.e. lumped amplification with zero noise figure). The equivalent accumulated ASE noise, which is equal to the sum of individual EDFA ASE noise contributions (according to Chapter 2, Section 2.2.2, Eq. 2.3 and using the noise figure in Table 4.1), was added at the end of the transmission link.

The performance of the system employing sphere shaping was investigated in comparison with uniform signaling and infinite-length MB shaping. For sphere shaping, the shaping sequence length L was varied in the range of 10–500, the shaping rate R_S was varied in the range of 1.54–2 bits/Amp. By default, simulations were done with 2D symbol mapping. Also, the impact of the dimensionality of symbol mapping (i.e. 1D, 2D and 4D) was studied.

For the MB shaping case, as discussed in Section 4.2.2 signals were drawn from an MB distribution with the entropy matching the shaping rate for sphere shaping. Note that symbols in the transmitted signal were drawn independently and identically on the underlying PMF. This method may be considered to give a finite-length sample of an infinite-length shaped sequence, which incurs no rate loss.

Results

For analysis of the simulated data, data fitting based on Gaussian noise (GN)-model [28] was performed. A detailed explanation of the data fitting approach can be found in Appendix A.2. Note that transceiver noise term is excluded from the fitting model, since transceiver impairments are not considered in the simulation model.
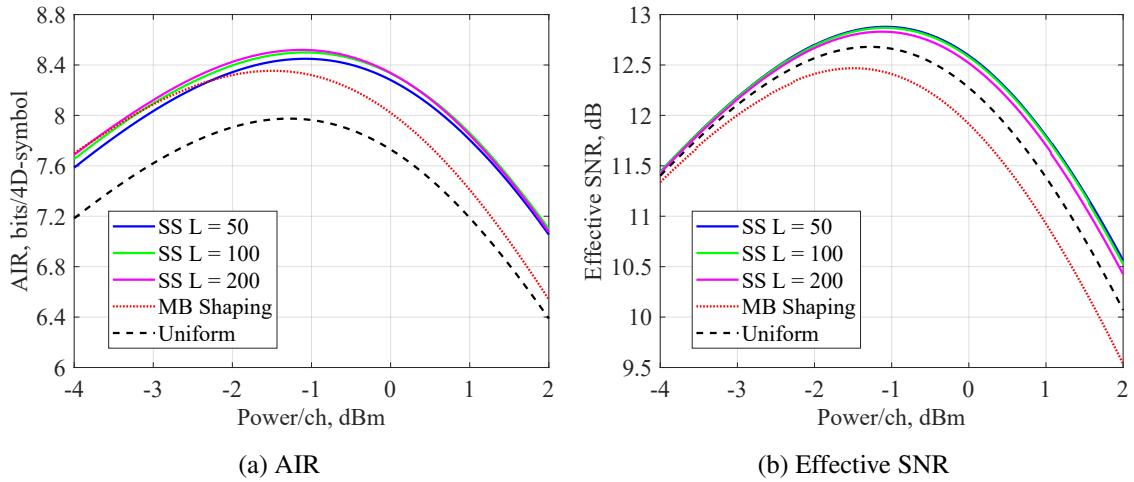
Fig. 4.6. Performance vs. optical launch power for 30 spans transmission in numerical simulations ($R_S = 1.70$, $L = 50, 100, 200$; 2D symbol mapping): (a) AIR, (b) Effective SNR.

Optical Launch Power Sweep: Fig. 4.6 (a) and (b) demonstrate system performance in terms of AIR and effective SNR as a function of optical launch power for uniform signaling, sphere shaping (with $L = 50, 100, 200$ and 2D symbol mapping) and MB shaping at $R_S = 1.70$. At the optimal launch power MB shaping provides 0.38 bits/4D-symbol AIR gain over uniform signaling, while sphere shaping offers higher AIR gain of $0.48, 0.53, 0.55$ bits/4D-symbol for $L = 50, 100, 200$. Corresponding effective SNR gains over uniforms signaling for sphere shaping are $0.2, 0.17, 0.1$ dB for $L = 50, 100, 200$, for MB shaping the effective SNR is degraded by 0.23 dB. This demonstrated that MB shaping exhibits nonlinear performance degradation. This effect is more pronounced at higher launch power (e.g. 2 dBm) — effective
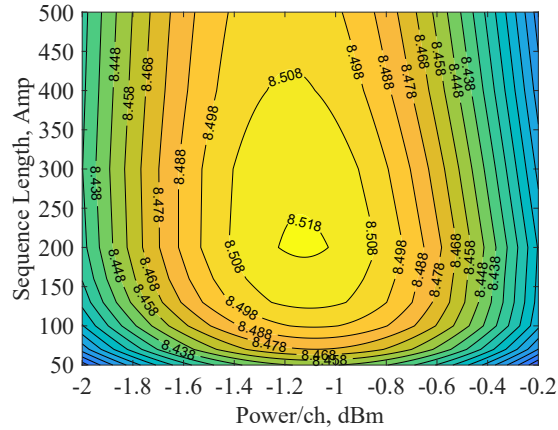
Fig. 4.7. Contour plot for AIR vs. shaping length and optical launch power for 30 spans transmission ($R_{\mathrm{S}} = 1.70$, 2D symbol mapping)

SNR degradation is more significant, while at lower input power (e.g. -4 dBm) SNR degradation is negligible, since this operation regime is close to linear channel.

Fig. 4.7 shows the contour plot for AIR at the optimum launch power as a function of shaping length and launch power for sphere shaping. Here, the shaping length L was varied in the range of 50–500. The optimal shaping length, which maximizes the AIR, can be identified to be close to $L = 200$. The performance of $L = 500$ is approximately equal to $L = 100$. The optimal launch power changes slightly with the shaping length — at shorter shaping length, the optimal launch power is slightly increased. Intuitively, this can be explained by the increased nonlinear tolerance at shorter shaping length.

(a) AIR

(b) Effective SNR

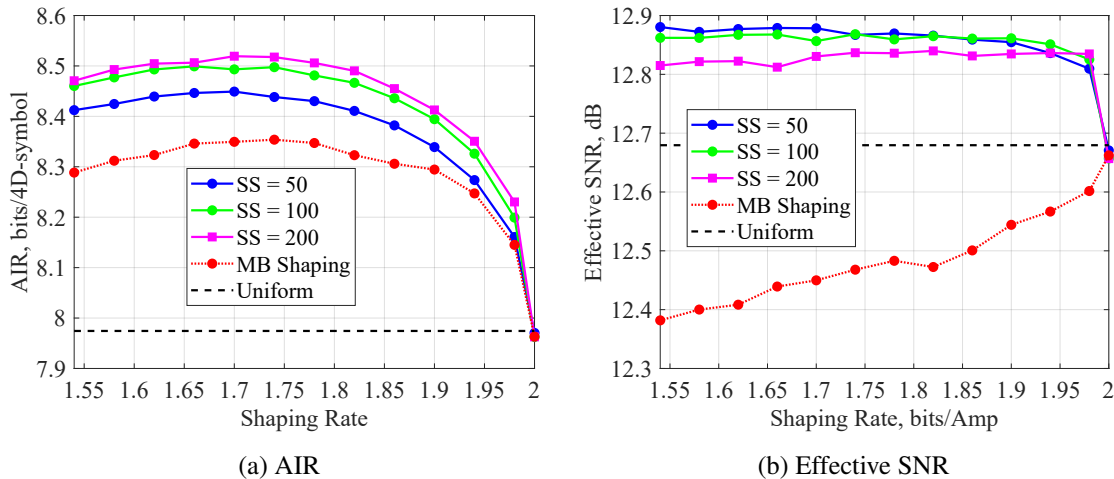Fig. 4.8. Performance vs. shaping rate for 30 spans transmission ($L = 50, 100, 200;$ 2D symbol mapping): (a) AIR, (b) Effective SNR.
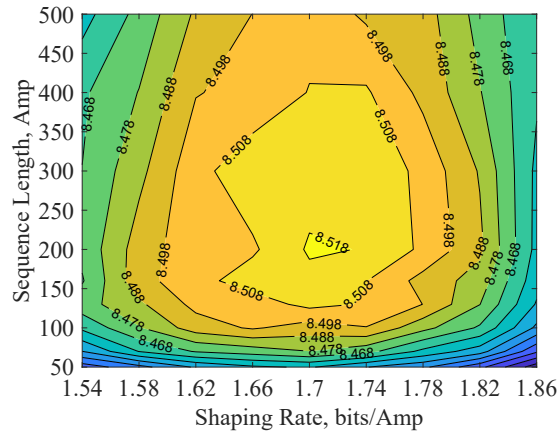
Fig. 4.9. Contour plot for AIR vs. shaping length and shaping rate for 30 spans transmission (2D symbol mapping)

Optimal Shaping Rate: Fig. 4.8 shows characterization of the AIR and effective SNR at the optimal launch power as a function of the shaping rate. According to Fig. 4.8 (a), the shaping rate $R_S = 1.70$ bits/Amp can be identified to be optimal for sphere shaping with $L = 50, 100, 200$ and MB shaping, since it maximizes the AIR. In general, the dependence of AIR on the shaping rate is relatively small. The variation in the shaping rate within 0.15–0.2 bits/Amp around the optimal value does not introduce significant change in AIR — the corresponding variation in AIR is 0.02–0.03 bits/4D-symbol. Note that $R_S = 2$ is equivalent to uniform signaling. In terms of effective SNR in Fig. 4.8 (b), in general, sphere shaping does not demonstrate significant dependence on the shaping rate — within the shaping rate R_S range of 1.54–1.98 the SNR variation is less then 0.05 dB (then, for $R_S > 1.98$ a sharp decrease in effective SNR is observed). On the contrary, the effective SNR for MB shaping demonstrates strong dependence on the shaping rate – for more shaped distributions the SNR degradation is increased (e.g. for $R_S = 1.54$ SNR degradation is 0.3 dB, while for $R_S = 1.9$ it is 0.15 dB). For infinite-length shaping this behaviour is supported by the observations in [134], where the dependence of nonlinear impairment on the symbols distribution was discussed — i.e. the larger statistical 4th moment (Kurtosis) of the stronger shaped signal (i.e. smaller shaping rate) leads to degraded effective SNR.

Fig. 4.9 shows the contour plot for AIR at the optimum launch power as a function of shaping length (in the range of 50–500) and shaping rate for sphere shaping. This plot extends the observations from Fig. 4.8 (a) that the optimal shaping rate is approximately $R_S = 1.70$ for a broader range of shaping lengths. It should be noted that the optimal shaping rate does not change significantly within the considered range of the shaping length.
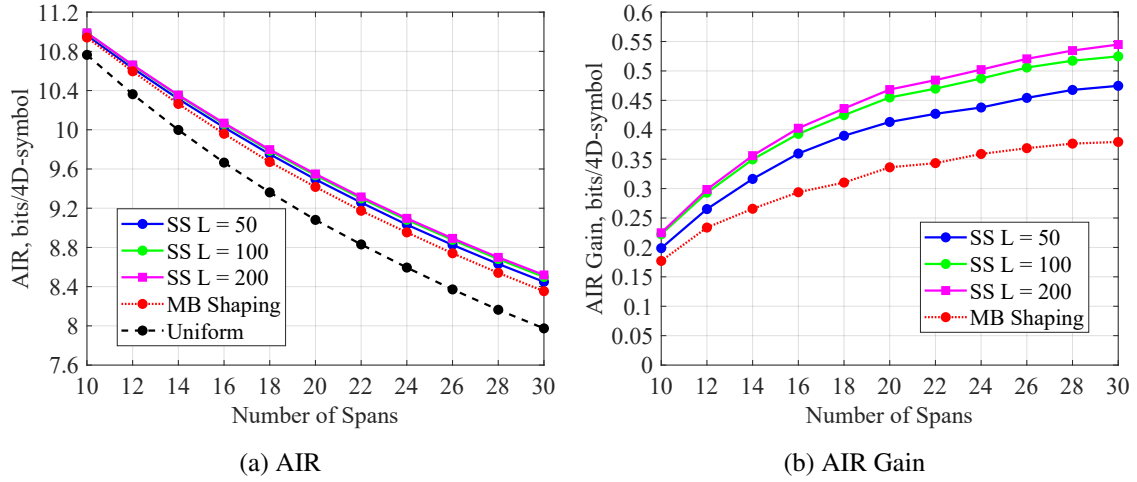
Fig. 4.10. AIR vs. number of spans (optimal shaping rate; $L = 50, 100, 200$; 2D symbol mapping): (a) AIR, (b) AIR Gain.

Transmission Distance Sweep: In Fig. 4.10 maximum AIRs and corresponding AIR gains (over uniform signaling) at optimum launch powers (defined per span) are demonstrated as a function of the number of transmission spans (equivalent to transmission distance sweep of 1000–3000 km). For each number of transmission spans, the shaping rates both for MB shaping and sphere shaping were optimized to maximize the corresponding AIRs. For transmission over 24–30 spans (2400–3000 km), the transmission reach increase is approximately 4 spans (400 km) for MB shaping and 5 spans (500 km) for sphere shaping with $L = 50, 100, 200$. As expected, at shorter transmission distance the reach increase in reduced — e.g. for 10–12 span, the reach increase is around 1 span (100 km) for both MB shaping and sphere shaping. The corresponding AIR gains are 0.38 bits/4D-symbol for MB shaping and $0.48, 0.53, 0.55$ bits/4D-symbol for sphere shaping with $L = 50, 100, 200$ for 30 spans transmission. For 10 spans transmission, the AIR gains are 0.17 bits/4D-symbol for MB shaping and $0.20, 0.22, 0.23$ bits/4D-symbol for sphere shaping with $L = 50, 100, 200$. Note that the advantage of sphere shaping over MB shaping in terms the shaping gain is more significant at longer transmission distance — intuitively, this is due to larger amount of accumulated nonlinear noise.

Symbol Mapping Dimensionality: In Fig. 4.11 the impact of symbol mapping dimensionality (1D, 2D, 4D) for sphere shaping with fixed shaping length $L = 200$ and shaping rate $R_S = 1.70$ was studied using launch power sweep measurements. At optimal launch power the variation in performance among 1D, 2D and 4D symbol mapping is relatively small — 2D symbol mapping provides the best performance with the AIR of 8.53 bits/4D-symbol, while AIRs for 4D and 1D symbol mapping are 8.51 and 8.48 bits/4D-symbol. At higher input

(a) AIR
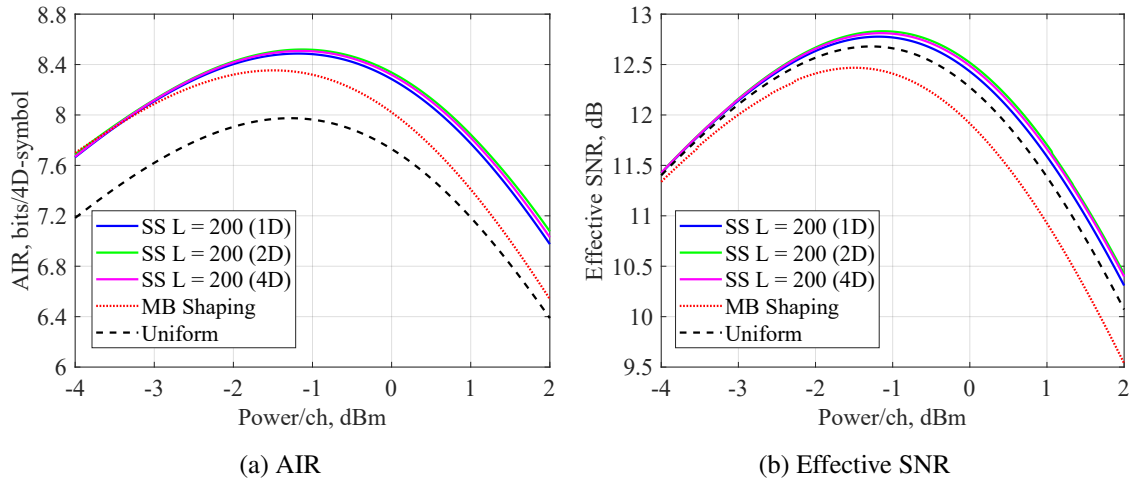
(b) Effective SNR

Fig. 4.11. Performance vs. optical launch power for 30 spans transmission in numerical simulations ($R_S = 1.70$, $L = 200$; 1D, 2D, 4D symbol mapping): (a) AIR, (b) Effective SNR.

power (i.e. in highly nonlinear regime) the variation in performance is more pronounced, while at lower input power (close to linear regime) the difference in performance vanishes.

(a) AIR
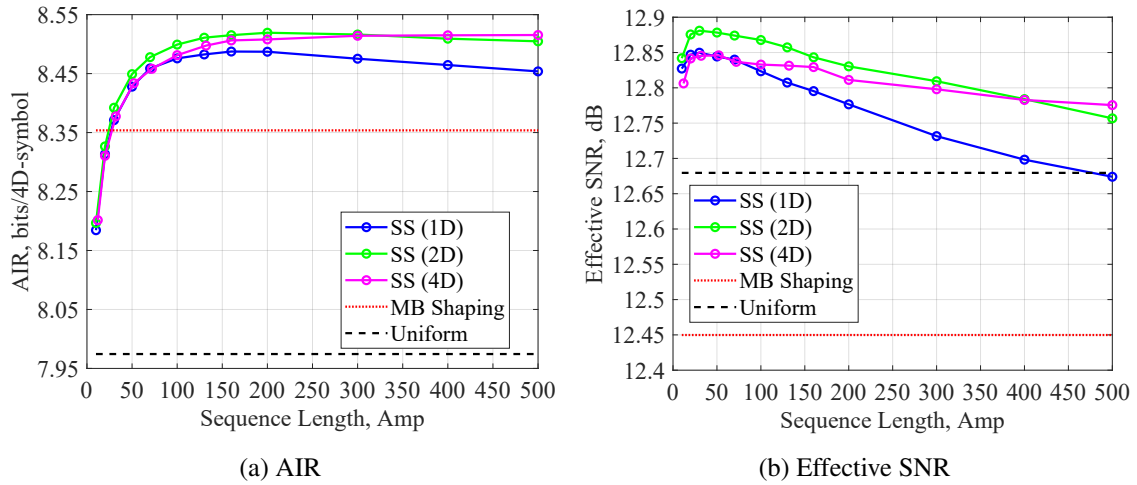
(b) Effective SNR

Fig. 4.12. Performance vs. shaping sequence length for 30 spans transmission ($R_S = 1.70$; 1D, 2D and 4D symbol mapping): (a) AIR, (b) Effective SNR.

Optimal Shaping Length: The impact of shaping length of sphere shaping on the system performance was studied for the fixed shaping rate $R_S = 1.70$ and 1D, 2D, 4D symbol mapping. Fig. 4.12 shows AIR and effective SNR at the optimal launch power as a function of shaping length. In general, at short shaping lengths AIR grows sharply with the shaping length reaching a peak in the region of $L = 200$, then, AIR starts to decrease gradually. AIR

gains are supported by the gains in terms of effective SNR. Note that the peaks for AIR and effective SNR are not matched in terms of the corresponding shaping length — SNR gain is maximized at shorter shaping length. The optimal shaping length, which maximizes the AIR, is defined by the optimal combination of SNR gain and rate loss (with corresponding energy efficiency). It is expected that performance of sphere shaping asymptotically approaches that of MB shaping at very long shaping lengths.

Regarding symbol mapping dimensionality, 2D symbol mapping provides slightly improved performance for $L < 300$. For longer shaping length 4D symbol mapping demonstrates a small advantage over 2D mapping. For 1D symbol mapping the performance is inferior for the whole range of considered shaping lengths.

Summary

For linear channels, power efficiency of the signaling scheme at the fixed transmission rate is the key criterion, which defines the available shaping gain. As mentioned previously in Section 4.2.2, infinite-length MB shaping offers optimal power efficiency and is expected to achieve the highest shaping gain for linear channels. Sphere shaping provides inferior power efficiency in finite-length shaping regime and, hence, a smaller shaping gain is expected.

Here, it was shown that in the nonlinear fibre channel finite-length sphere shaping can achieve higher shaping gain than that of infinite-length MB shaping, while being less power efficient. This is due to the improved nonlinear tolerance, which was observed as the improvement in effective SNR.

The performance can be maximized using the shaping sequence length of $L = 200$. It should be noted that most of shaping gain can be achieved with more modest shaping sequence lengths (e.g. $L = 50$–100).

4.3.3 Performance of Sphere Shaping in Extended-Reach Single-Span Links

In the following, the nonlinear performance of sphere shaping in extended-reach single-span transmission was studied in comparison with uniform signaling and infinite-length shaping with an ideal MB distribution. In particular, the impact of shaping length, dimensionality of symbol mapping, and shaping rate on nonlinear tolerance was investigated.

Simulated System

An extended-reach single-span transmission link consisting of 220 km SSMF was simulated. The loss of the fiber was compensated at the end of the transmission link by an EDFA and

the ASE noise was added (according to Chapter 2, Section 2.2.2, Eq. 2.3 and using the noise figure in Table 4.1).

Similarly to the long-haul transmission case, the performance of the system employing sphere shaping was investigated in comparison with uniform signaling and infinite-length MB shaping. For sphere shaping, the shaping sequence length L was varied in the range of 10–100, the shaping rate R_S was varied in the range of 1.54–2 bits/Amp. By default, simulations were done with 2D symbol mapping. Also, the impact of dimensionality of symbol mapping (i.e. 1D, 2D and 4D) was studied.

Results

As above in Section 4.3.2, data fitting based on Gaussian noise (GN)-model [28] was performed for analysis of the simulated data. A detailed explanation of the data fitting approach can be found in Appendix A.2.
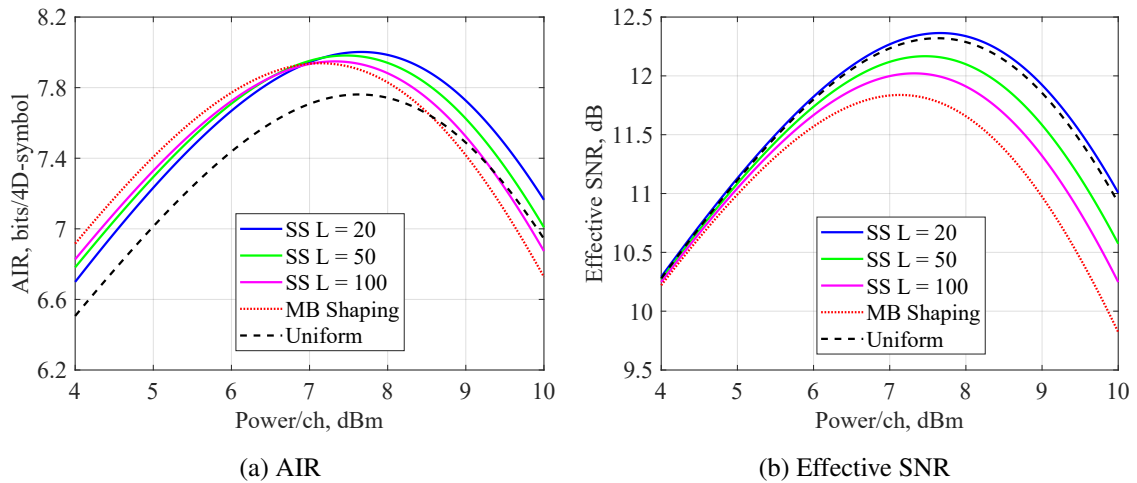
Fig. 4.13. Performance vs. optical launch power for single-span transmission ($R_S = 1.82$, $L = 20, 50, 100$; 2D symbol mapping): (a) AIR, (b) Effective SNR.

Optical Launch Power Sweep: Fig. 4.13 (a) and (b) demonstrate system performance in terms of AIR and effective SNR as a function of optical launch power for uniform signaling, sphere shaping (with $L = 20, 50, 100$ and 2D symbol mapping) and MB shaping at $R_S \approx 1.82$ (expected to be close to optimal). Note that due to finite granularity of the shaping rate, the actual shaping rate value might be slightly mismatched for specific shaping sequence lengths (in particular, for short ones). At the optimal launch power MB shaping provides 0.27 bits/4D-symbol AIR gain over uniform signaling, while sphere shaping offers higher AIR gain of 0.34, 0.32, 0.29 bits/4D-symbol for $L = 20, 50, 100$. In terms of effective SNR,
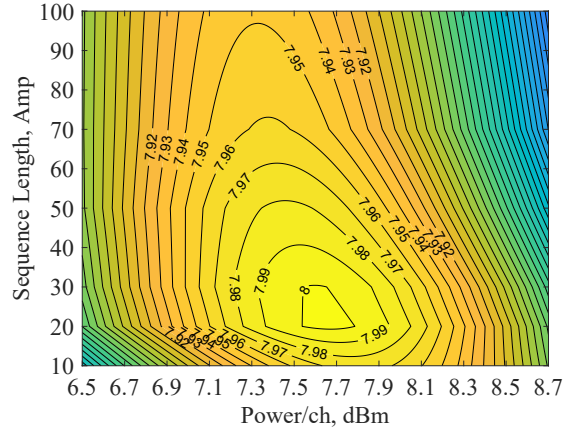
Fig. 4.14. Contour plot for AIR vs. shaping length and optical launch power for single-span transmission ($R_S \approx 1.82$, 2D symbol mapping)

sphere shaping with $L = 20$ exhibits small gain of 0.05 dB over uniform signaling, while for $L = 50, 100$ effective SNR is degraded by 0.15 dB and 0.3 dB. For MB shaping the SNR degradation is 0.5 dB. In the highly nonlinear regime SNR degradation is more significant (e.g. for MB shaping it is 1.2 dB), while in the linear regime SNR degradation is negligible.

Fig. 4.14 shows the contour plot for AIR at the optimum launch power as a function of shaping length and launch power for sphere shaping. Here, the shaping length L was varied in the range of 10–100. In contrast to the long-haul transmission case, the optimal shaping length can be identified to be close to $L = 20$, which is a significantly shorter shaping length operation regime. Also, the optimal launch power changes more significantly with the shaping length — at shorter shaping length, the optimal launch power is increased. These observations suggest that in single-span transmission the increased nonlinear tolerance at short shaping length is more pronounced.

Note that, in general, in extended-reach single-span transmission, shaped signals exhibit stronger nonlinear performance degradation in comparison to the long-haul transmission case (the effective SNR operation range is similar to the long-haul transmission case) due to highly correlated short-memory nature of nonlinear interactions — hence, the observed AIR gains for shaping schemes are smaller.

Optimal Shaping Rate: Fig. 4.15 shows characterization of the AIR and effective SNR at the optimal launch power as a function of the shaping rate. According to Fig. 4.15 (a), the optimal shaping rate is approximately 1.82 bits/Amp for sphere shaping with $L = 20, 50$, while for $L = 100$ and MB shaping it is slightly higher ($\sim$ 1.86 bit/Amp). The dependence of AIR on the shaping rate is slightly stronger compared to the long-haul transmission

(a)

(b)
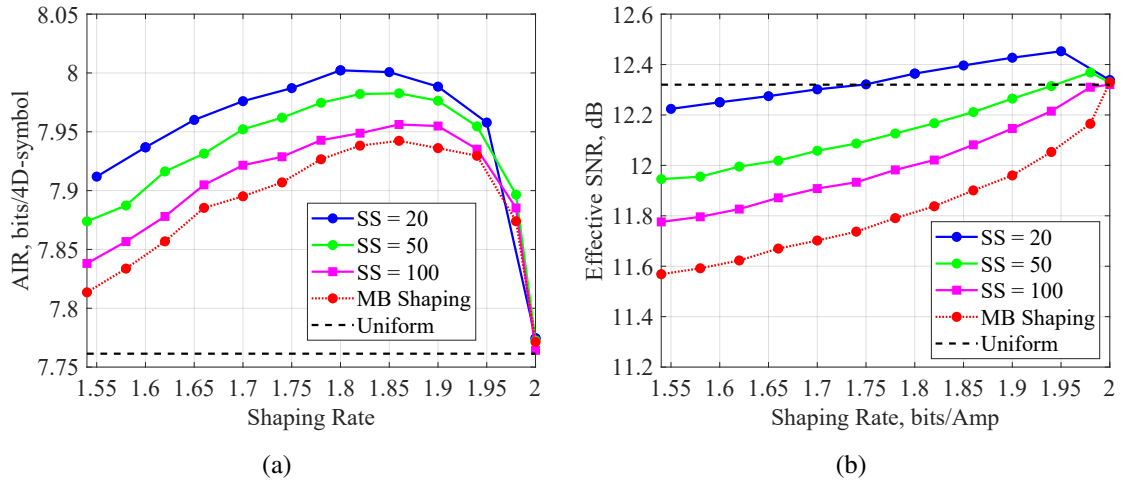
Fig. 4.15. Performance vs. shaping rate for single-spans transmission ($L = 20, 50, 100$; 2D symbol mapping): (a) AIR, (b) Effective SNR.
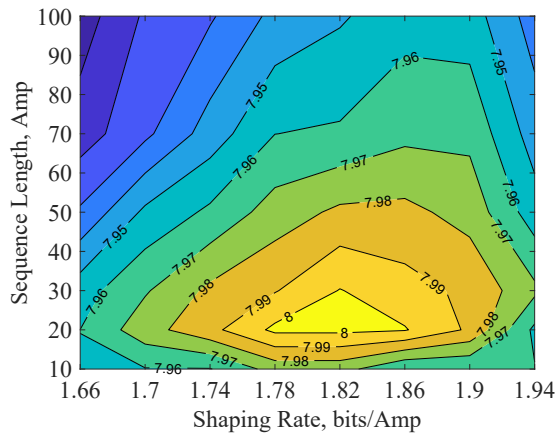
Fig. 4.16. Contour plot for AIR vs. shaping length and shaping rate single-span transmission (2D symbol mapping)

case. The variation in the shaping rate within 0.1 bits/Amp around the optimal value does not introduce significant change in AIR — the corresponding variation in AIR is 0.02–0.03 bits/4D-symbol. In terms of effective SNR in Fig. 4.15 (b), again, shaped signals demonstrate stronger dependence on the shaping rate compared to the long-haul transmission case — effective SNR steadily increases with the shaping rate; sphere shaping with longer shaping length exhibits larger SNR variation, while MB shaping demonstrates the largest SNR dependence. Overall, the stronger dependence of the performance on the shaping rate in comparison to the long-haul transmission case may be associated with a stronger performance dependence on the 4th moment of the signal distribution [134] in the case of correlated short-memory nonlinear interactions.

103

Fig. 4.16 shows the contour plot for AIR at the optimum launch power as a function of shaping length (in the range of 10–100) and shaping rate for sphere shaping. This plot extends the observations from Fig. 4.15 (a) — the optimal shaping rate is approximately $R_S = 1.82$ for short shaping lengths (i.e. $L = 10$–50) and increases with the shaping length.

(a) AIR	(b) Effective SNR
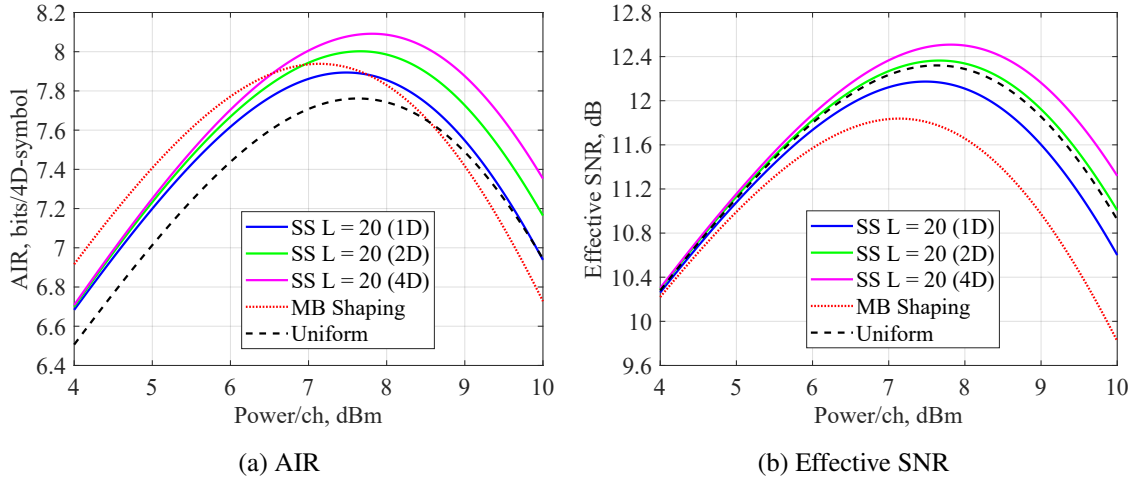
Fig. 4.17. Performance vs. optical launch power for single-span transmission ($R_S = 1.82$; $L = 20$; 1D, 2D and 4D symbol mapping): (a) AIR, (b) Effective SNR.

Symbol Mapping Dimensionality: In Fig. 4.17 the impact of symbol mapping dimensionality (1D, 2D, 4D) for sphere shaping with fixed shaping length $L = 20$ and shaping rate $R_S = 1.82$ was studied using launch power sweep measurements. In contrast with long-haul transmission, the variation in performance at optimal launch power among 1D, 2D and 4D symbol mapping for sphere shaping is very significant — 4D symbol mapping provides the best performance with the AIR of 8.1 bits/4D-symbol, while AIRs for 2D and 1D symbol mapping are 8 and 7.9 bits/4D-symbol, respectively. In terms of effective SNR, 4D symbol mapping provides a gain of 0.2 dB, while for 2D mapping the gain is only 0.05 dB. For 1D symbol mapping effective SNR is degraded by 0.14 dB. In the highly nonlinear regime the variation in performance is more pronounced, while in the linear regime the difference in performance vanishes. Note that the performance of 1D symbol mapping is worse than that of MB shaping.

Optimal Shaping Length: The impact of shaping length of sphere shaping on the system performance was studied for the fixed shaping rate $R_S = 1.82$ and 1D, 2D, 4D symbol mapping. Fig. 4.18 shows AIR and effective SNR at the optimal launch power as a function of shaping length. As mentioned previously, in contrast to the long-haul transmission case,
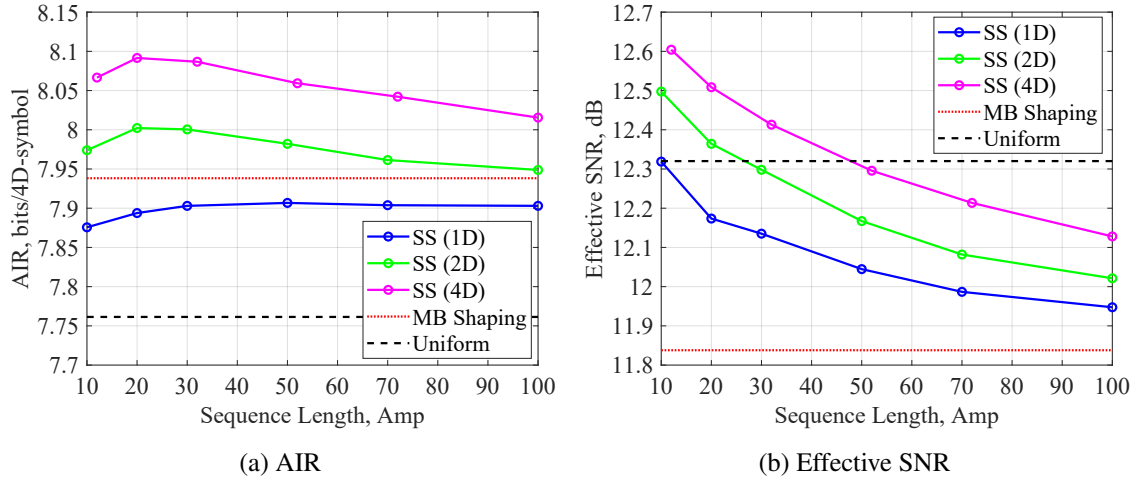
Fig. 4.18. Performance vs. shaping sequence length for single-span transmission ($R_S = 1.82$; 1D, 2D and 4D symbol mapping): (a) AIR, (b) Effective SNR.

short shaping length provides the optimal performance — the AIR is maximized at the shaping length $L = 20$. AIR gains are supported by the gains in terms of effective SNR — effective SNR increases at short shaping lengths. Similarly to the long-haul transmission case, it is expected that performance of sphere shaping asymptotically approaches that of MB shaping at very long shaping lengths.

As opposed to the case of long-haul transmission, symbol mapping dimensionality has very significant impact on the system performance. 4D symbol mapping offers the highest performance gain over the range of considered shaping lengths — at the optimal shaping length the AIR gain is 0.1 bits/4D-symbol over 2D symbol mapping and 0.2 bits/4D-symbol over 1D mapping. Effectively, sphere shaping with 4D symbol mapping doubles the shaping gain of MB shaping using the shaping length $L = 20$. For 1D symbol mapping the performance is inferior for the whole range of considered shaping lengths.

Summary

Similarly to the long-haul transmission case, for the extended-reach single-span transmission link, finite-length sphere shaping also demonstrates improved nonlinear tolerance and higher shaping gain than MB shaping. However, some important differences should be noted.

First, available shaping gains are smaller both for sphere shaping and MB shaping — stronger nonlinear impairment is observed for shaped inputs. Note that the transmission distance was chosen such that the system operates within the same effective SNR range as for the long-haul transmission case.

Second, a shaping sequence length of tens of amplitudes is sufficient to maximize the AIR of the system. In contrast with long-haul transmission case, where the optimal shaping length is $L = 200$, here, the optimal shaping length is $L = 20$.

Third, the symbol mapping dimensionality has much stronger impact on the system performance. In contrast to the long-haul transmission case, here, 4D symbol mapping offers significant performance improvement over 2D and 1D symbol mapping strategies.

In general, in extended-reach single-span transmission links with low accumulated CD, signals may suffer from strong highly correlated short-memory nonlinearities as opposed to the long-haul transmission links, where nonlinearities turn into more Gaussian-like noise due large accumulated CD [140]. Hence, the temporal structure of the signal (e.g., ordering of transmitted symbols) has a stronger impact on nonlinear performance. By shortening the shaping sequence length, it is possible to introduce some advantageous changes in the temporal structure — e.g. reduced concentration of high-power symbols [137]. Also, by increasing the dimensionality of symbol mapping, the effective shaped symbol sequence length can be reduced as well as the number of simultaneously interacting independent shaped sequences, which leads to reduced probability of high peak power values.

4.4 Nonlinear System Performance Analysis in Experiment

Previously, in Section 4.3, it was shown that nonlinearity tolerant shaping is of particular interest for short-distance transmission with low accumulated CD. Low CD leads to highly correlated short-memory nonlinear interactions. Also, when increasing the transmission reach of the single-span system, these nonlinearities become very strong due to increased optimal launch power. For extended-reach single-span systems improved nonlinear tolerance can be achieved with short-length shaping, which is attractive in terms of implementation complexity.

In this Section, the nonlinear system performance was analyzed experimentally in extended-reach single-span link. HCSS was chosen as the shaping technique under test.

4.4.1 Performance of Huffman-Coded Sphere Shaping in Extended-Reach Single-Span Links

In the following, the nonlinear performance of HCSS in extended-reach single-span transmission was studied in comparison with uniform signaling and infinite-length shaping with an ideal MB distribution. In particular, the impact of shaping length, dimensionality of symbol

mapping, and shaping rate on nonlinear tolerance was investigated. Also, coded performance is analyzed using low-density parity-check (LDPC) codes, which provide matching data rate for shaping schemes and uniform signaling.

Transmission Experiment

Similarly to the numerical simulations case, transmission of 9 DP 64-QAM channels over an extended-reach single span link consisting of 200 km SSMF was carried out. The performance of the system employing HCSS was investigated in comparison with uniform signaling and infinite-length MB shaping. For HCSS, the shaping sequence length (L in the range of 8–160), dimensionality of amplitude-to-symbol mapping (1D, 2D and 4D) and shaping rate (R_S in the range of 1.625–1.875 b/Amp) were varied.

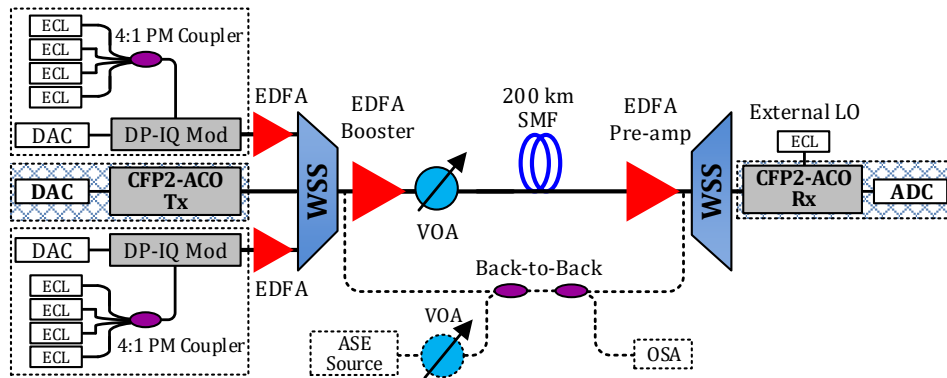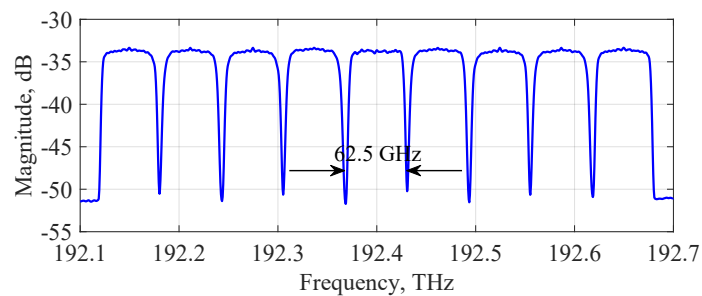Fig. 4.19. Block diagram of transmission experimental setup.

Fig. 4.20. Signal spectrum (measured with 2 GHz resolution). 9 channels (root-raised cosine pulse shaping with 10% roll-off factor) at 56 GBd on a 62.5 GHz grid.

Experimental Setup: The experimental setup is shown in Fig. 4.19. WDM transmission of 9 DP 64-QAM channels operating at 56 GBd (with root-raised cosine pulse shaping with

10% roll-off factor) on a 62.5 GHz grid was carried out over a 200 km single-span link of SSMF. All channels used the same shaping scheme under investigation.

The central channel-under-test (CUT) was generated using a 92 GSa/s DAC, followed by a pluggable CFP2-ACO transceiver [16] (integrated laser with nominal 100 kHz linewidth). The 8 interfering channels were divided into two groups of 4 channels, and generated by two pairs of DP Mach–Zehnder IQ modulators and DACs, where 4 external cavity lasers with 100 kHz linewidth combined with a polarization maintaining coupler were used for each modulator/DAC pair. The two groups of interfering channels were then pre-amplified by EDFAs, and spectrally interleaved and combined with the CUT via a programmable wavelength selective switch (WSS). The resulting spectrum of the generated WDM signal is shown in Fig. 4.20.

At the link input the WDM signal was amplified by a booster EDFA, then a variable optical attenuator (VOA) was used to control the total launched power. After transmission over 200 km of SSMF, the WDM signal was pre-amplified by an EDFA with a noise figure of 5.5 dB and the CUT was filtered by a WSS. Finally, the CUT was received by a CFP2-ACO transceiver (an external laser with 100 kHz linewidth was used as a local oscillator) and its analog output was sampled and digitized by a 92 GSa/s ADC.

In back-to-back configuration, the output of the transmitter-side WSS was connected to the receiver-side WSS via a pair of couplers used for noise loading. An ASE noise source and VOA were used for varying OSNR, while an optical spectrum analyzer (OSA) was used for OSNR measurement.

Digital Signal Processing: DSP was performed offline according to the generic flow introduced in Chapter 2, Section 2.4. At the transmitter-side, firstly, random signals were generated according to the shaping and mapping scheme under consideration. Then, root-raised cosine pulse shaping was applied followed by transmitter pre-emphasis (to compensate for frequency response and skews). Finally, the signals were uploaded to the DACs.

At the receiver-side the signal recovery was implemented as follows. Firstly, the received data was extracted from the ADC and receiver pre-compensation was applied (compensation of frequency response, skews and IQ imbalance). Then, CD was compensated, clock recovery was performed by a frequency-domain Gardner algorithm, conventional complex-valued DD-LMS 2×2 MIMO equalization (35 filter taps) was performed in conjunction with CPR in fully data-aided mode, and post-equalization was done using real-valued DD-LMS 2×2 MIMO equalizers (5 filter taps) to enable compensation of residual transmitter IQ impairments (see Chapter 3, Section 3.3.1). Soft-demapping assumed a circularly symmetric

Gaussian channel, and transmission performance metrics were averaged over approximately 5×10^6 symbols.

Performance Metrics

Analogously to the numerical simulations case, the system performance analysis was performed using two metrics: effective SNR and AIR. However, metrics were refined by calculating the centroids of the received symbols.

Transmitted signal and received signal after DSP algorithms are denoted by X and Y. The transmitted signal X takes values from the 4D-constellation $\mathscr{X} = \{x_1, \ldots, x_M\}$. The adjusted transmitted signal X' is defined to take values from $\mathscr{X}' = \{x'_1, \ldots, x'_M\}$, such that the new constellation points x'_i represent the centroids of the received symbols y corresponding to the original constellation points x_i, which can be expressed as

$$x'_i = \mathrm{E}[y|x_i], \tag{4.17}$$

where $\mathrm{E}[\cdot]$ denotes the expectation.

The adjusted constellation $\mathscr{X}'$ is subsequently used for estimation of effective SNR and soft-demapping. This reduces the impact of impairments, which represent geometrical distortions of the constellation (e.g., transceiver nonlinearity and uncompensated modulation impairments).

The effective SNR of the received signal is calculated as

$$\mathrm{SNR}_{\mathrm{eff}} = \frac{\mathrm{Var}[X']}{\mathrm{Var}[Y - X']}, \tag{4.18}$$

where $\mathrm{Var}[\cdot]$ denotes the variance. In that case, effective SNR accounts for both linear and nonlinear noise contributions accumulated during signal propagation over an optical fiber, as well as transceiver noise floor (i.e., implementation penalty and DSP imperfections).

The soft-demapper calculates LLRs for binary labels B_i ($i = 1, \ldots, m$) as

$$\mathrm{LLR}_i = \log \frac{\sum_{x \in \mathscr{X}'_{1,i}} f_{Y|X'}(y|x') P_{X'}(x')}{\sum_{x \in \mathscr{X}'_{0,i}} f_{Y|X'}(y|x') P_{X'}(x')}, \tag{4.19}$$

where $\mathscr{X}'_{1,i}$ and $\mathscr{X}'_{0,i}$ are the subsets of constellation $\mathscr{X}'$, which represent B_i being equal to 1 or 0, respectively; $f_{Y|X'}(y|x')$ is the transition probability density function of the auxiliary channel used for mismatched decoding; $P_{X'}(x')$ is the 4D PMF (calculated according to Appendix A.1).

A memoryless 4D circularly symmetric Gaussian auxiliary channel is considered and it is assumed that the noise in each dimension is independent and identically distributed [147]. In this case, the channel can be described as

$$f_{Y|X'}(y|x') = \frac{1}{(\pi\sigma^2)^2} \exp\left(-\frac{\|y-x'\|^2}{\sigma^2}\right), \tag{4.20}$$

where σ^2 is the noise variance. Lower-dimensional soft-demapping can be done analogously for the case of 1D and 2D mapping.

As for numerical simulations, the AIR for BICM impacted by the rate loss associated with finite-length shaping [108] is calculated in b/4D-symbol as

$$AIR = GMI - R_{loss}, \tag{4.21}$$

where GMI is calculated using Monte-Carlo approach according to Eq. 2.41 (Chapter 2, Section 2.5.3). Note that for both uniform signaling and infinite-length MB shaping $R_{loss} = 0$ and AIR is given by GMI only.

Coded performance was analyzed based on normalized GMI (nGMI), which can be calculated for a uniform signal as

$$nGMI = \frac{GMI}{m} = \frac{AIR}{m}, \tag{4.22}$$

while for shaped signals it is calculated as

$$nGMI = 1 - \frac{H(X) - GMI}{m} = 1 - \frac{4 \cdot (R_S + 1) - AIR}{m}, \tag{4.23}$$

For the shaped signals, an inner LDPC code with rate 0.72 and length 52,800 was used, and decoding was performed over 32 iterations of the sum-product algorithm. Uniform signals were encoded with an LDPC code with rate 0.64 and length 52,800, and decoded in the same manner. In both cases, it is assumed that an outer Bose–Chaudhuri–Hocquenghem (BCH) code with rate 0.9922 is used, which achieves an output BER below 10^{-15} given an input BER of 5×10^{-5} [148].

Back-to-Back Transmission Results

Fig. 4.21 shows a back-to-back characterization of the system under consideration. Uniform signaling, MB shaping at $R_S = 1.75$ bits/Amp, and HCSS with $L = 16, 32, 48$ and 4D symbol mapping at the same shaping rate are compared. Fig. 4.21(a) illustrates the variation of AIR

(a) AIR
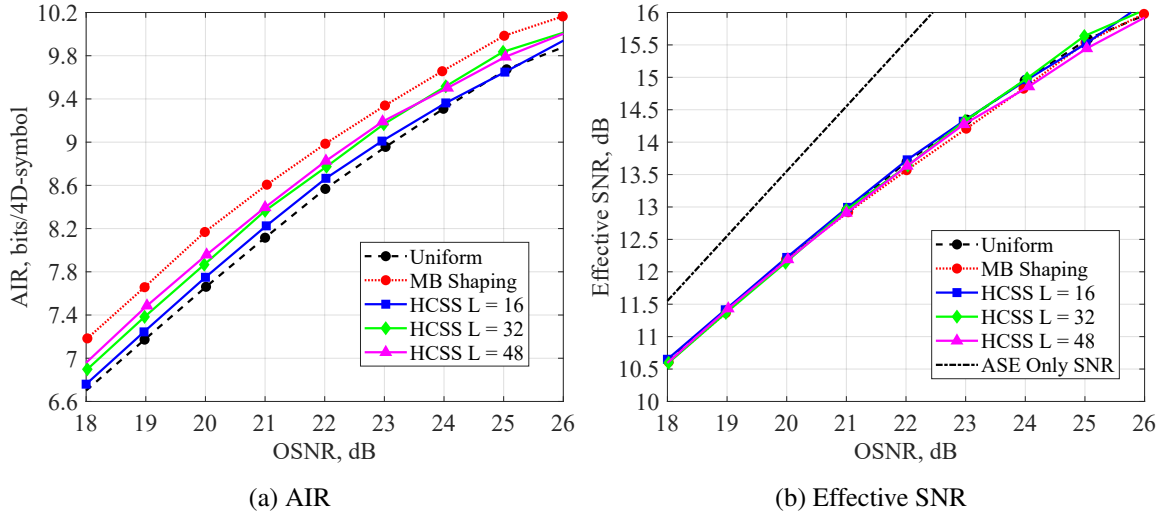
(b) Effective SNR

Fig. 4.21. Performance vs. OSNR in back-to-back configuration ($R_S = 1.75$; $L = 16, 32, 48$; 4D symbol mapping): (a) AIR, (b) Effective SNR.

(a) Uniform   (b) MB Shaping   (c) HCSS
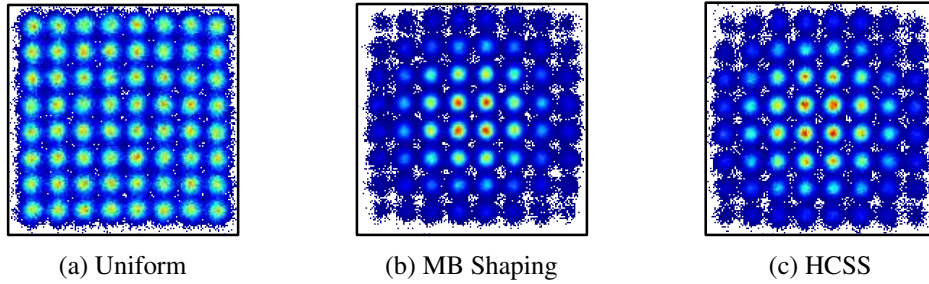
Fig. 4.22. Experimental constellations in back-to-back under high OSNR (~ 35 dB): (a) Uniform, (b) Maxwell–Boltzmann shaping, (c) Huffman-coded sphere shaping ($L = 32$).

with OSNR. Infinite-length MB shaping achieves superior performance with a 0.48 bits/4D-symbol AIR gain compared with uniform signaling over an operating OSNR range of 18–21 dB. HCSS achieves gains of 0.08, 0.22 and 0.32 bits/4D-symbol for $L = 16, 32, 48$, respectively. This shows the trend that longer length shaping achieves better performance (eventually, approaching that of MB shaping), as is expected for linear channels. Note that for higher OSNR values, shaping gain reduces both for HCSS and MB shaping.

Fig. 4.21(b) illustrates the variation of effective SNR with OSNR. There is no noticeable difference in terms of effective SNR over an operating OSNR range of 18–21 dB (SNR range of 10.5–13 dB) for the shaping schemes under consideration. Therefore, this demonstrates that shaping algorithms do not introduce additional implementation penalty over uniform signaling over the range of SNRs under consideration. Also, note that shaping sequence length and symbol mapping strategy do not impact the SNR in back-to-back.

111

(a)

(b)
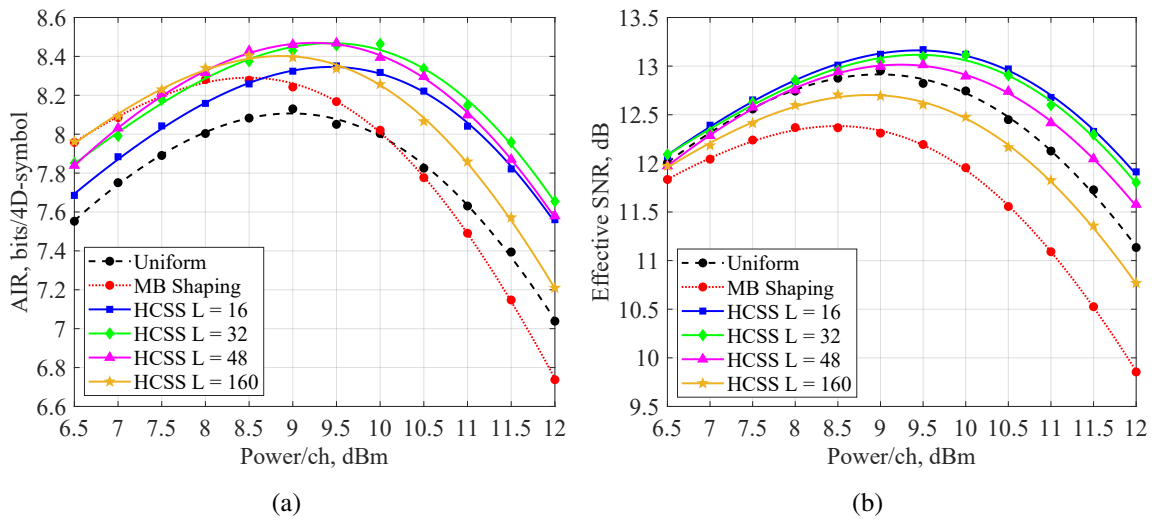
Fig. 4.23. Performance vs. optical launch power for single-span transmission ($R_S = 1.75$; $L = 16, 32, 48, 160$; 4D symbol mapping): (a) AIR, (b) Effective SNR.

(a)

(b)
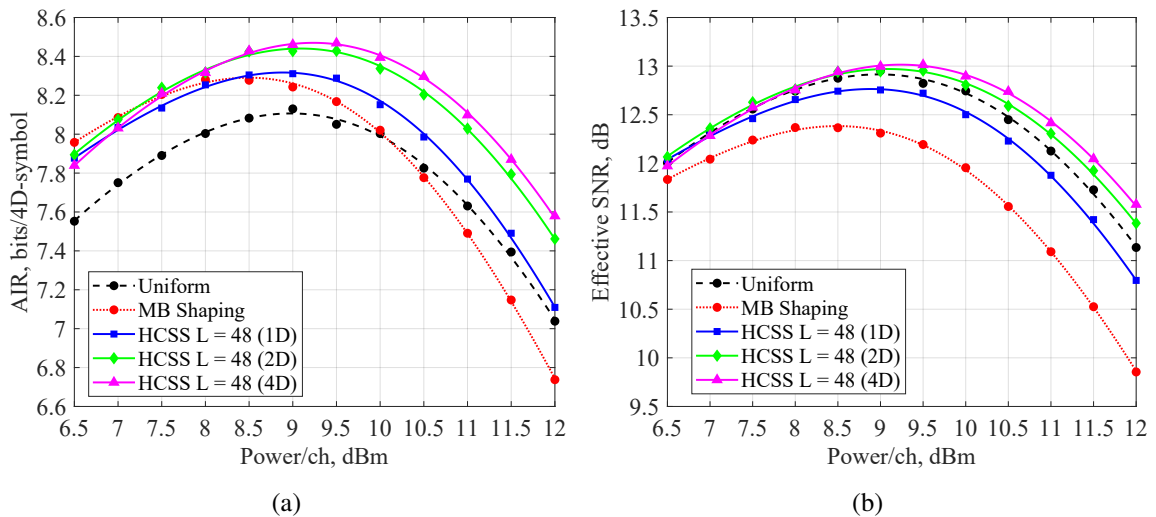
Fig. 4.24. Performance vs. optical launch power for single-span transmission ($R_S = 1.75$; $L = 48$; 1D, 2D and 4D symbol mapping): (a) AIR, (b) Effective SNR.

Fig. 4.22 (a)–(c) shows constellation diagrams for uniform signaling, MB shaping and HCSS ($L = 32$, 4D symbol mapping) at $R_S = 1.75$ bits/Amp under high OSNR (~ 35 dB, which is the highest achievable in the considered experimental setup). No notable visual difference between HCSS and MB shaped constellations can be observed.
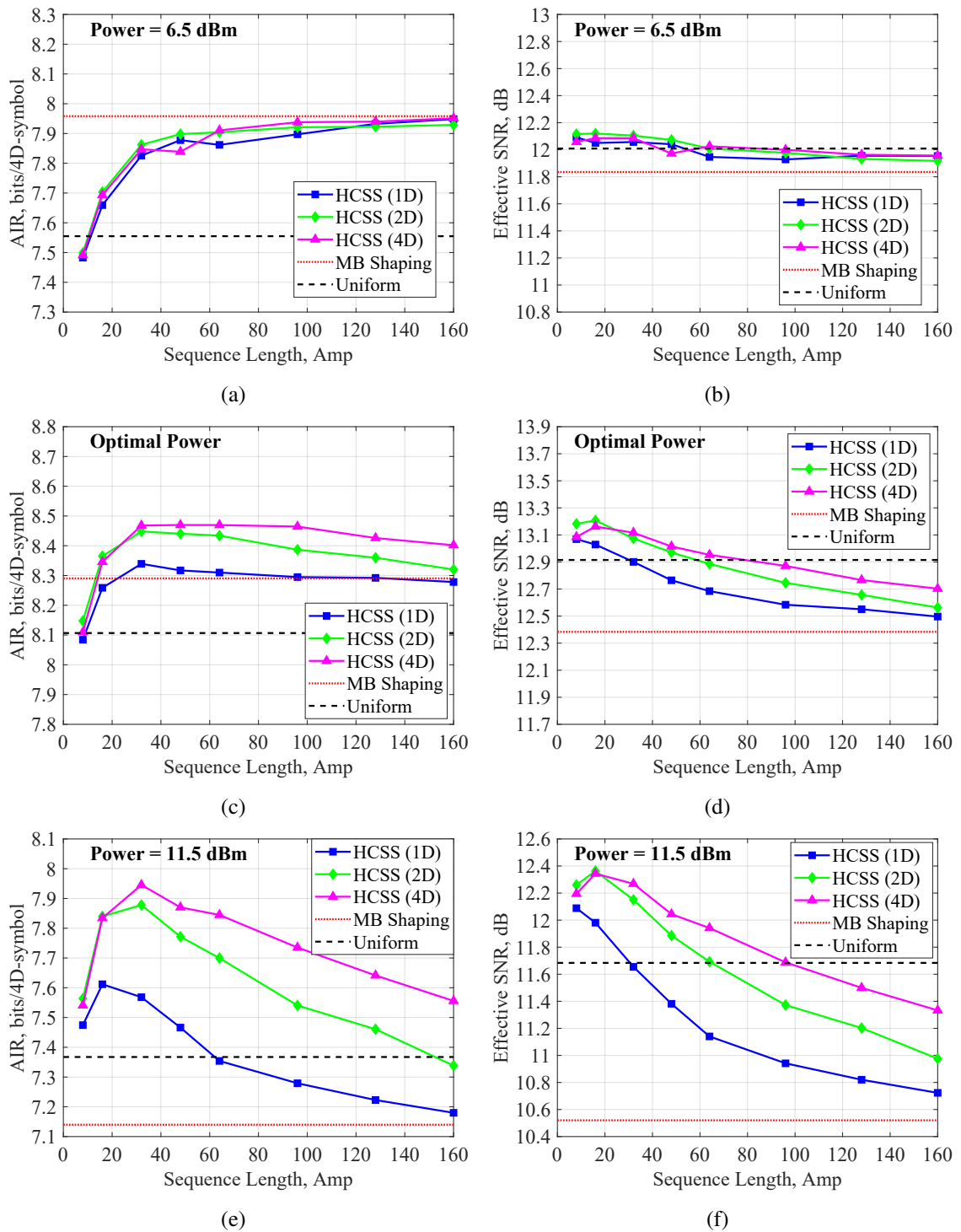
Fig. 4.25. Performance vs. shaping sequence length ($R_S = 1.75$; 1D, 2D and 4D symbol mapping): (a) and (b) AIR and effective SNR for launch power of 6.5 dBm, (c) and (d) AIR and effective SNR for optimal launch power, (e) and (f) AIR and effective SNR for launch power of 11.5 dBm.
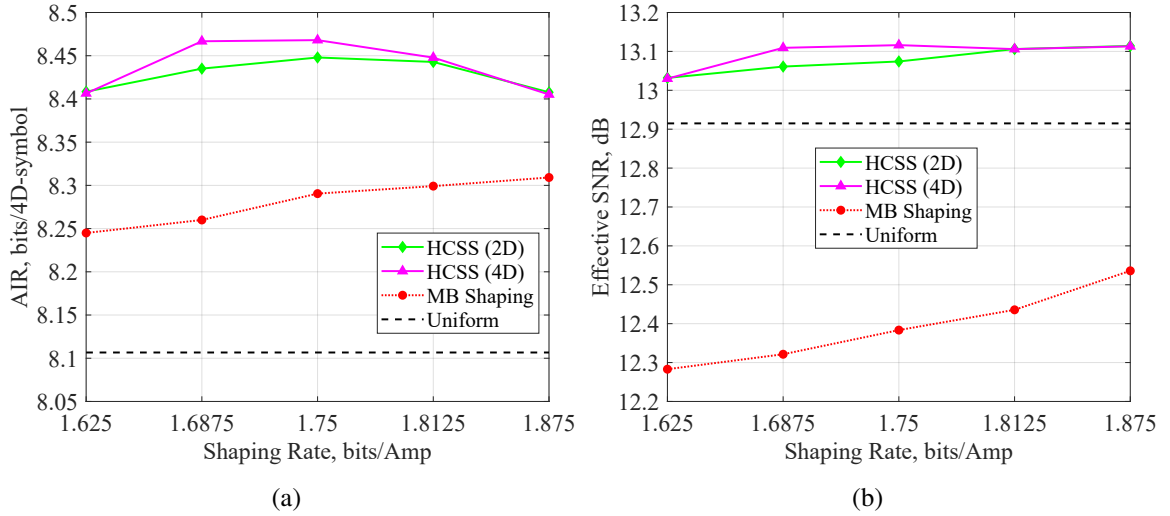
Fig. 4.26. Performance vs. shaping rate ($L = 32$; 2D and 4D symbol mapping): (a) AIR, (b) Effective SNR.

Single-Span Transmission Results

For analysis of the experimental data for single-span transmission, data fitting based on a Gaussian noise (GN)-model [28] was performed. A detailed explanation of the data fitting approach can be found in Appendix A.2. Note that an additional term, which is responsible for transceiver noise floor, is included in the fitting model.

Optical Launch Power Sweep: Figs. 4.23 and 4.24 demonstrate system performance characterization in terms of AIR and effective SNR as a function of optical launch power for uniform signaling, MB shaping and HCSS at $R_S = 1.75$ bits/Amp. Individual data points represent measured experimental data, while corresponding smooth lines represent the data fit. Note that the model described in Appendix A.2 provides a very good fit to the measured experimental data.

Fig. 4.23 (a) and (b) show AIR and effective SNR for uniform signaling, MB shaping and HCSS using $L = 16, 32, 48, 160$ with 4D symbol mapping. In the linear regime, performance is consistent with that of the back-to-back measurements. HCSS with longer sequence length achieves higher AIR (approaching the performance of MB shaping with $L = 160$), while variation in effective SNR is relatively small. At the optimal launch power, MB shaping achieves a gain over uniform signaling of 0.18 bits/4D-symbol, while HCSS exhibits gains of $0.24, 0.37, 0.38, 0.30$ bits/4D-symbol for $L = 16, 32, 48, 160$, respectively. MB shaping suffers from severe nonlinear impairment, which can be seen as effective SNR degradation of 0.52 dB compared to uniform signaling at optimum power, while HCSS demonstrated

114

improved nonlinearity tolerance. HCSS with $L = 16, 32, 48$ elicits SNR gains of 0.3, 0.17, 0.06 dB compared to uniform signaling at optimal power, while for $L = 160$ the effective SNR is reduced by 0.2 dB. In the highly nonlinear regime (launch power above ~ 11 dBm), the performance degradation for MB shaping and HCSS with $L = 160$ is more significant, whereas the gain for HCSS with shorter shaping length is increased.

Fig. 4.24 (a) and (b) show AIR and effective SNR for uniform signaling, MB shaping and HCSS using $L = 48$ with 1D, 2D and 4D symbol mapping strategies. HCSS with higher-dimensional symbol mapping achieves better performance in the nonlinear regime. At the optimal launch power, HCSS with 4D symbol mapping achieves AIR gains of 0.04, 0.15 bits/4D-symbol with corresponding SNR gain of 0.05, and 0.25 dB compared to 2D and 1D symbol mapping, respectively. In the linear regime, the performance difference is negligible among all symbol mapping strategies.

Note that in Figs. 4.23 and 4.24 the general performance trends of HCSS are in good agreement with the performance of conventional sphere shaping in numerical simulations shown in Figs. 4.13 and 4.17.

Optimal Shaping Length: Fig. 4.25 demonstrates the performance in terms of AIR and effective SNR when varying the shaping sequence length of HCSS ($L = 64, 96, 128$ are added into consideration) with 1D, 2D and 4D symbol mapping strategies in linear, optimal launch power and highly nonlinear regimes. Note that the results shown in Fig. 4.25 are based on fitting of launch power sweep measurements.

As discussed previously, in the linear regime, which is shown in Fig. 4.25 (a) and (b), HCSS with longer shaping sequence length provides higher AIR and closely approaches MB shaping performance with $L = 160$. No significant difference is observed among all symbol mapping strategies. Effective SNR also varies insignificantly — there is minor SNR gain at shorter sequence lengths due to weak presence of nonlinearities.

In the optimal launch power regime, which is shown in Fig. 4.25 (c) and (d), HCSS using 2D and 4D symbol mapping demonstrates significant performance gain in terms of AIR with the shaping sequence length L in the range of 32–96, while HCSS using 1D symbol mapping provides performance close to MB shaping (with $L \geq 16$). The sequence length $L = 32$ can be considered optimal (achieving the highest AIR) for all symbol strategies — AIR gain over uniform signaling is 0.37, 0.34, 0.22 bits/4D-symbol (and 0.19, 0.16, 0.06 b/4D over MB shaping) for 4D, 2D and 1D symbol mapping, respectively. AIR gain is supported by the improvement in effective SNR — 4D mapping provides the highest SNR gain compared to 1D and 2D mapping with $L \geq 32$, while 2D mapping slightly outperforms with $L \leq 16$. For
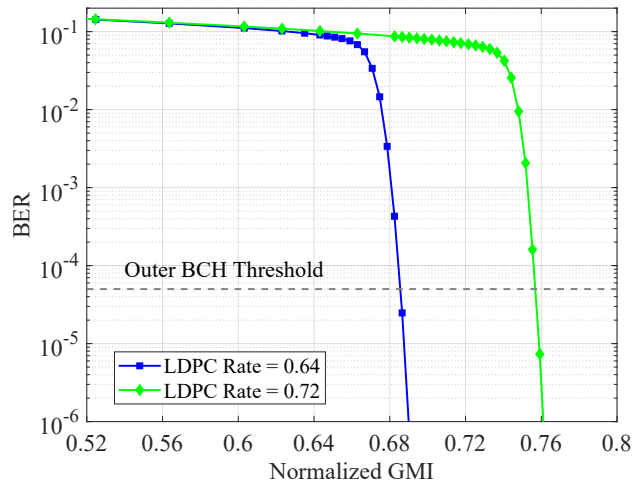
Fig. 4.27. Characterization of LDPC codes: BER vs. normalized GMI.

optimal sequence length of $L = 32$, SNR gain over uniform signaling is 0.2, 0.16, 0 dB (and 0.72, 0.68, 0.52 dB over MB shaping) for 4D, 2D and 1D symbol mapping, respectively.

In the highly nonlinear regime, which is shown in Fig. 4.25 (e) and (f), a similar performance trend can be observed as for optimal launch power regime, however, the gain (both in AIR and SNR) with short shaping length is exaggerated. For instance, 0.58 bits/4D-symbol AIR gain and 0.6 dB SNR gain over uniform signaling (0.83 bits/4D-symbol and 1.75 dB over MB shaping) can be observed with $L = 32$ and 4D symbol mapping.

Similarly to the conventional sphere shaping, HCSS with longer shaping sequence length can achieve better power efficiency for a fixed rate, and therefore provide higher shaping gain in a linear channel. This is clearly seen in the back-to-back case and linear regime of single-span transmission. In the presence of significant fiber nonlinearities, shorter shaping sequences provide higher nonlinear tolerance by improving the effective SNR in the received signal. By choosing appropriate shaping length for the operating regime, an optimal trade-off of shaping gain and effective SNR gain can be achieved. Also, increasing the dimensionality of the symbol mapping improves nonlinear performance by shortening the shaped symbol sequence length in the time-domain and reducing probabilities of high peak power values, while maintaining the same power efficiency.

Optimal Shaping Rate: Next, the impact of the shaping rate on the transmission performance was studied. Fig. 4.26 shows a characterization of the AIR and effective SNR as a function of the shaping rate. For HCSS we considered shaping sequence length $L = 32$ with 2D and 4D symbol mapping. Each data point is based on the data fit of launch power sweep measurements and represents the performance at the optimal launch power.
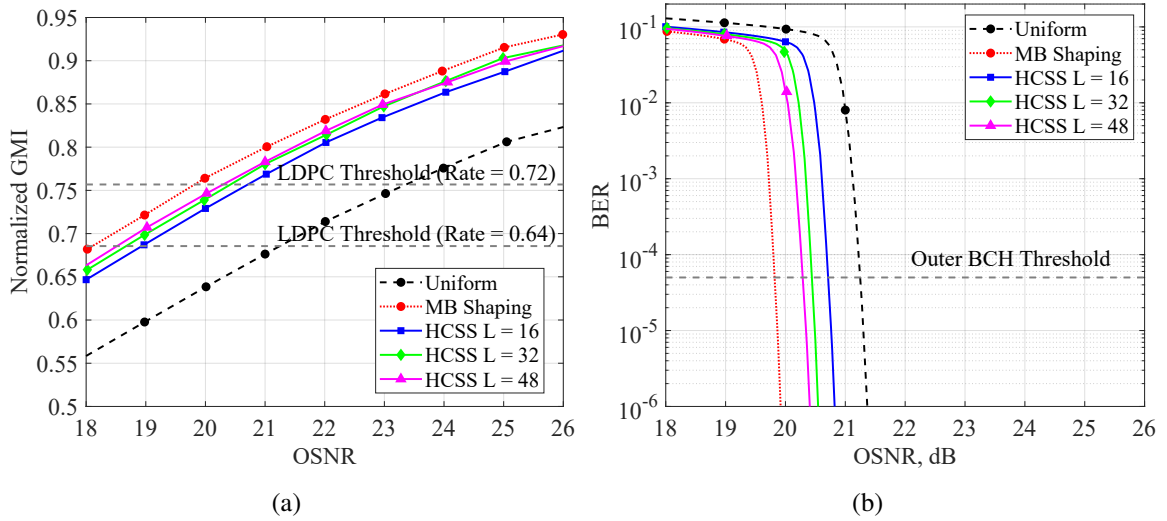
Fig. 4.28. Coded performance analysis in back-to-back configuration: (a) normalized GMI vs. OSNR, (b) predicted BER after LDPC vs. OSNR.

From Fig. 4.26 (a) we observe that $R_S = 1.75$ b/Amp is the optimal shaping rate for HCSS — AIR varies over 0.07 b/4D in R_S range of 1.625–1.875 bits/Amp achieving the highest value at $R_S = 1.75$ bits/Amp, the corresponding variation in effective SNR is 0.1 dB. For MB shaping, the AIR increases with the shaping rate by 0.06 bits/4D-symbol (within R_S of consideration), which is supported by the corresponding increase in effective SNR of 0.25 dB.

In the case of HCSS with fixed shaping sequence length, the optimal effective SNR does not depend significantly on the shaping rate. Therefore, it can be assumed that the optimal shaping rate is mostly affected by the linear shaping gain contribution. Conversely, MB shaping demonstrates stronger dependence of both effective SNR and AIR on the shaping rate, indicating that the increase in AIR with shaping rate is associated with nonlinear transmission gain. Note that with increasing shaping rate, MB shaping will converge to uniform signaling, while HCSS will exhibit some rate loss due to the dyadic distribution of compositions constraint.

Coded Performance: For coded performance analysis MB shaping and HCSS with 4D symbol mapping at $R_S = 1.75$ bits/Amp were considered. The net bit rate after shaping and coding was 424.1 Gb/s for both MB shaping and HCSS, while for uniform signaling the net rate was 426.7 Gb/s. BER after LDPC decoding (Fig. 4.28 (b) and Fig. 4.29 (b)) is predicted based on nGMI (Fig. 4.28 (a) and Fig. 4.29 (a)). The individual points represent predicted BER based on measured nGMI values, while corresponding smooth lines represent
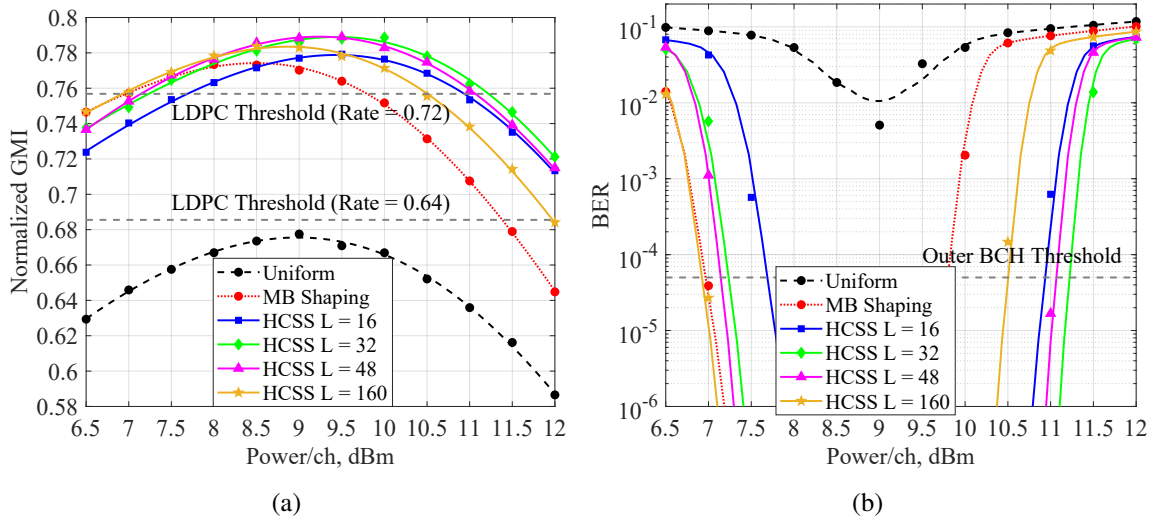
Fig. 4.29. Coded performance analysis for single span transmission: (a) normalized GMI vs. optical launch power, (b) predicted BER after LDPC vs. optical launch power.

predicted BER based on fitted nGMI values (which are calculated from AIR fit using (4.22) and (4.23)).

The characterization of LDPC codes in terms BER as a function of nGMI is shown in Fig. 4.27. The LDPC nGMI thresholds for the outer BCH code (such that the BER at the output of LDPC code is below the BCH code threshold of 5×10^{-5}) are 0.757 and 0.686 for code rates of 0.72 and 0.64, respectively.

Fig. 4.28 demonstrates coded performance for the back-to-back configuration. MB shaping achieves the best sensitivity, while HCSS with longer shaping length achieves better sensitivity than with shorter length — for MB shaping OSNR margin is improved by 1.3 dB, for HCSS the OSNR margin is improved by 0.5, 0.7, 0.7 dB for $L = 16, 32, 48$, respectively.

Coded performance for single-span transmission is shown in Fig. 4.29. In the linear regime the sensitivity shows the similar trend as for back-to-back configuration, while in nonlinear regime $L = 32$ demonstrated the best sensitivity. With $L = 32$ the launch power margin is improved by 1.3 dB compared to the MB shaping. Note that in case of uniform signaling, desired performance is not achievable.

Summary

HCSS was experimentally investigated as a method for probabilistic constellation shaping for application in optical fibre communication systems comprising extended-reach single-span links, subject to strong nonlinearities. In general, the experimental performance behaviour

of the system employing HCSS confirms the trends observed for the conventional sphere shaping in numerical simulations.

The naïve approach of optimizing the signal PMF (i.e. targeting MB distribution) and attempting to achieve this with an infinite-length distribution matcher, while being optimal in the linear channel, is highly suboptimal in this case, significantly reducing the ultimate shaping gain. Such a system, which employs infinite-length MB shaping, can achieve only a maximum 0.18 bits/4D-symbol AIR gain in the considered 200 km single-span link. Conversely, HCSS effectively doubles the shaping gain of infinite-length MB shaping — it achieves an AIR gain of 0.37 bits/4D-symbol with a shaping sequence length of only $L = 32$ and 4D symbol mapping. Also, it should be noted that HCSS algorithms may be implemented without multiplications, and with modest LUT sizes, e.g., for $L = 32$ the size is no more than 100 kbit.

4.5   Chapter Summary

In this Chapter, the advantage of finite-length probabilistic shaping over infinite-length shaping in the nonlinear fiber channel was demonstrated in numerical simulations and experiment. Two transmission links were considered: a multi-span long-haul link and an extended-reach single-span link.

First, conventional finite-length sphere shaping was investigated in extensive numerical fiber simulations. Effects of shaping sequence length, dimensionality of symbol mapping and shaping rate were investigated and optimal shaping parameters were defined for both multi-span long-haul and extended-reach single-span links. It was shown that finite-length sphere shaping provides higher shaping gains and improved nonlinear tolerance than infinite-length Maxwell–Boltzmann (MB) shaping, which is optimal for linear channels. In general, available shaping gains are smaller in extended-reach single-span transmission links due to the stronger impact of nonlinearities on the shaped signal inputs. Another important observation is that in extended-reach single span links the performance is maximized using significantly shorter shaping length (i.e. $L = 20$) and nonlinear gains are more pronounced compared to the long-haul transmission case, where the performance is maximized with longer shaping length (i.e. $L = 200$). This is due to that in the short distance links the nonlinear noise is highly correlated and has short memory, hence, temporal effects imposed by the short-length shaping give more significant advantage. In contrast, for long-haul systems nonlinearities become significantly decorrelated (turning into Gaussian-like noise) and longer length shaping is required, as for linear channels.

Second, Huffman-coded sphere shaping (HCSS) was used to experimentally study the nonlinear performance in extended-reach single-span links. HCSS is the algorithm which approximates the spherical structure and provides nearly optimal energy efficiency at low implementation complexity. Analogously to the numerical simulations, the impact of shaping sequence length, dimensionality of symbol mapping and shaping rate was examined. It was shown experimentally, that similarly to the numerical simulation results for conventional sphere shaping, HCSS with short shaping length provides significant nonlinear shaping gains and the naïve approach of infinite-length MB distribution matching is inferior in the nonlinear fiber channel. Coded system performance, with a net data rate of approximately 425 Gb/s for both shaped and uniform inputs, was also analyzed. It should be noted that HCSS can be implemented with LUTs, which allows for low-complexity, multiplier-free shaping. For the optimal shaping length ($L = 32$), the combinatorial mapping and demapping algorithms can be implemented with integer addition and comparison operations only, utilizing an LUT with 100 kbit size.

Chapter 5

Conclusions and Outlook

5.1   Summary and Conclusions

Delivering higher capacity that networks providers are demanding requires critical advancements in fibre-optical technologies. Recent developments enabled widespread deployment of power-efficient and compact transceivers, which offer high data rates and utilize state-of-the-art components, highly-complex DSP and advanced modulation schemes.

This thesis covered some aspects of transceiver performance optimization via DSP-based characterization and mitigation of various transceiver impairments, as well as application of advanced high-dimensional modulation — specifically, finite-length probabilistic constellation shaping.

Chapters 1 and 2 introduced the background, described the fundamental concepts of high-speed coherent fibre-optical systems and prepared the basis for the key results presented in this thesis. The following Chapters presented novel findings and techniques developed throughout the work during the Ph.D program.

Transceiver Impairments Characterization and Mitigation

Chapter 3 presented work on transceiver impairments characterization and mitigation. The importance of compensation of the key transceiver impairments to enable system operation with high-order modulation formats at high symbol rates was demonstrated, and multiple compensation techniques were proposed and investigated.

First, the impact of transceiver skews was considered and two DSP-based calibration techniques were proposed: a calibration technique for both transmitter-side and receiver-side skews based on Gardner timing error detector, and a calibration technique for transmitter

P. Skvortcov, Ph.D Thesis, Aston University, 2020

IQ skews based on signal image spectrum measurement. Good calibration accuracy was demonstrated in numerical simulations and experiment. These techniques can be considered as low-complexity self-calibration solutions, which can be applied prior to normal transmission operation of the transceiver. Only simple additional DSP operations and no additional apparatus are required.

Second, the impact of transmitter IQ impairments was considered and DSP-based post-compensation and pre-emphasis techniques were proposed. The post-compensation technique is based on advanced post-equalization within the receiver DSP. Compensation of various IQ impairments was studied: modulation impairments (gain imbalance, quadrature error and bias offsets), IQ skews, electrical IQ cross-talk and mismatched frequency response. It was shown that receiver-side post-equalization can significantly reduce the impact of those impairments. The key advantage of the receiver-based compensation is real-time operation, which can potentially relax calibration requirements. However, if multiple severe impairments are present simultaneously, a quite substantial performance penalty can still remain. In that case, MIMO pre-emphasis can be used to efficiently pre-compensate these impairments at the transmitter side.

Probabilistic Constellation Shaping

Chapter 4 presented work on application of high-dimensional modulation in the form of finite-length probabilistic constellation shaping for transmission over long-haul multi-span and extended-reach single-span links. It was demonstrated that superior linear and nonlinear performance of the system can be achieved using a finite-length sphere shaping architecture in comparison with infinite-length shaping and conventional uniform multi-level QAM signaling schemes.

First, the impact of shaping parameters (i.e. shaping sequence length, dimensionality of symbol mapping, and shaping rate) was investigated for conventional sphere shaping via extensive numerical simulations and optimal operational regimes were identified. It was shown that the naïve approach of targeting a Maxwell-Boltzmann (MB) distribution and simulating an infinite-length distribution matcher, while being optimal in the linear channel, is suboptimal in the nonlinear fiber channel. Finite-length sphere shaping provides higher shaping gains and improved nonlinear tolerance than infinite-length MB shaping both for long-haul multi-span and extended reach single-span links. However, for extended-reach single-span transmission performance is maximized with the shaping length significantly shorter compared to the long-haul transmission case, which is very attractive in terms of implementation. Then, Huffman-coded sphere shaping (HCSS), which represents an approximation of the spherical structure and can be implemented with look-up tables, was

used to experimentally study the nonlinear performance in extended-reach single-span links. Analogously to the numerical simulations for conventional sphere shaping, it was experimentally shown that short-length HCSS also provides significant performance gain despite its slightly reduced power efficiency.

In general, improved nonlinear performance is observed due to the temporal effects in the signal introduced by the finite-length sphere shaping schemes. In short distance links with low accumulated chromatic dispersion (CD), signals are affected by strong highly correlated short-memory nonlinearities, while in long-haul links nonlinearities become significantly decorrelated due to larger CD and turn into more Gaussian-like noise. Hence, temporal structures in the signal imposed by the short-length shaping is more advantageous for extended-reach single-span transmission, while for long-haul transmission energy efficiency considerations are more important and, hence, longer shaping length is required.

5.2   Future Work Outlook

The work presented in this thesis can be further developed in the following directions:

- One interesting research topic is related to the application of transceiver performance optimization techniques in digital sub-carrier multiplexed (DSCM) systems. Techniques presented in this thesis were primarily designed for single-carrier systems. However, DSCM technology was recently introduced in commercial transceivers offering advantageous performance and flexibility compared to single-carrier transceivers [15]. Hence, transceiver performance optimization approaches should be adopted for DSCM systems:

    - DSCM systems are affected by the same transceiver impairments, however, their impact can be viewed in a different way. For DSCM systems IQ impairments result in mirrored images of single side-band digital sub-carriers, which act as the cross-talk between them. Hence, simplified approaches for IQ impairments compensation potentially may be adopted.
    - DSCM systems expand the number of dimensions available for modulation. Hence, more sophisticated high-dimensional modulation schemes can be used. For instance, finite-length shaping schemes considered in this thesis can be used to jointly shape multiple sub-carriers, which may results in higher tolerance to nonlinear impairments.

- Another research topic is related to the development of nonlinearity-aware shaping schemes. As discussed previously, sphere shaping offers improved nonlinear tolerance

due to advantageous temporal structures introduced in the signal in the short-length shaping regime. However, these temporal effects are more complementary rather than deliberately designed features and come at the expense of reduced power efficiency. Potentially, more optimal solutions can be developed, which can provided simultaneously better energy efficiency and increased nonlinear tolerance [29].

Appendix A

Auxiliary Material

This Appendix contains auxiliary material for Chapter 4. Section A.1 describes an approach for calculation of probability mass function for signals generated using sphere shaping architectures with multi-dimensional symbol mapping. Section A.2 gives a detailed description of data fitting approach performed for analysis of numerical simulation and experimental results.

A.1 Probability Mass Function Calculation

To construct a four-dimensional (4D) DP 64-QAM format, let us consider the alphabet of amplitudes $\mathscr{A} = \{a_1, a_2, a_3, a_4\} = \{1, 3, 5, 7\}$ and the alphabet of signs $\mathscr{S} = \{s_1, s_2\} = \{-1, 1\}$. The alphabet of a 4D-signal (4D-constellation) can be expressed as the Cartesian product $\mathscr{X} = \mathscr{S}^4 \times \mathscr{A}^4$, where $\mathscr{S}^4$ and $\mathscr{A}^4$ are 4-fold Cartesian products with themselves.

A composition is defined as $C_i = \{c_1^i, c_2^i, c_3^i, c_4^i\}$, where i is the index of the composition in the spherical structure, and c_k^i is the number of instances of amplitude a_k in the shaped amplitude sequence of length $L = \sum_{k=1}^{4} c_k^i$.

It is postulated that the probability distribution of signs $P_S(s)$ is uniform. Hence, $P_S(s) = 1/2$ for $\forall s \in \mathscr{S}$ and $P_{S^4}(s^4) = 1/16$ for $\forall s^4 \in \mathscr{S}^4$. The PMF of a 4D-signal can be therefore expressed as

$$P_X(x) = P_{S^4}(s^4) \cdot P_{A^4}(a^4) = 1/16 \cdot P_{A^4}(a^4), \tag{A.1}$$

where $P_{A^4}(a^4)$ can be considered as the PMF of a 4D-quadrant and $a^4 = [a_{k_1}, a_{k_2}, a_{k_3}, a_{k_4}]$ is a 4D-amplitude vector.

1D Symbol Mapping

Since all components of a 4D-amplitude vector are mapped from independent shaped amplitude sequences, the PMF for a 4D-quadrant is a product of 1D-PMFs:

$$P_{A^4}(a^4) = P_A(a_{k_1}) \cdot P_A(a_{k_2}) \cdot P_A(a_{k_3}) \cdot P_A(a_{k_4}). \tag{A.2}$$

The 1D-PMF which results from the ith composition can be calculated as $P_A^i(a_k) = c_k^i/L$, while the total 1D-PMF is

$$P_A(a_k) = \sum_{i=1}^{N} p_i P_A^i(a_k) = \sum_{i=1}^{N} p_i \frac{c_k^i}{L}, \tag{A.3}$$

where p_i is the probability of occurrence of the ith composition, and N is the total number of compositions.

2D Symbol Mapping

In the case of 2D symbol mapping, two consecutive amplitudes from two independent shaped amplitude sequences are used to construct a 4D-amplitude vector. Therefore, the 4D-quadrant PMF can be expressed as the product of 2D-PMFs:

$$P_{A^4}(a^4) = P_{A^2}(a^2) \cdot P_{A^2}(a^{2*}), \tag{A.4}$$

where $a^2 = [a_{k_1}, a_{k_2}]$ and $a^{2*} = [a_{k_3}, a_{k_4}]$ are 2D-amplitude vectors, $a^4 = [a^2, a^{2*}]$.

Since components of 2D-amplitude vectors are mapped from a single sequence and not independent, the 2D-PMF resulting from the ith composition can be calculated as

$$P_{A^2}^i(a^2) = \left[\frac{c_{k_1}^i}{L} \cdot \frac{c_{k_2}^i - \delta}{L-1} \right]^+, \tag{A.5}$$

where $[\cdot]^+$ denotes $\max\{\cdot, 0\}$ operator, δ is

$$\delta = \begin{cases} 0, & k_1 \neq k_2, \\ 1, & k_1 = k_2. \end{cases} \tag{A.6}$$

The total 2D-PMF is

$$P_{A^2}(a^2) = \sum_{i=1}^{N} p_i P_{A^2}^i(a^2), \tag{A.7}$$

4D Symbol Mapping

Since four consecutive amplitudes from a single shaped amplitude sequence are used to produce a 4D-amplitude vector (all components of 4D-amplitude vector are not independent), the 4D-quadrant PMF resulting from the ith composition is given by

$$P_{A^4}^i(a^4) = \left[\frac{c_{k_1}^i}{L} \cdot \frac{c_{k_2}^i - \delta_1}{L-1} \cdot \frac{c_{k_3}^i - \delta_2}{L-2} \cdot \frac{c_{k_4}^i - \delta_3}{L-3} \right]^+, \tag{A.8}$$

where δ_l is

$$\delta_l = \sum_{m=1}^{l} I_{k_{l+1}=k_m}, \tag{A.9}$$

where $I_{k_{l+1}=k_m}$ is the indicator function which equals 1 when the condition $k_{l+1} = k_m$ is true and equals 0 otherwise.

The total 4D-PMF is

$$P_{A^4}(a^4) = \sum_{i=1}^{N} p_i P_{A^4}^i(a^4). \tag{A.10}$$

We note that the 4D-PMF can not be decomposed into the product of lower-dimensional PMFs.

Example

Consider a shaper with a single composition $C = \{6, 5, 3, 2\}$ of length $L = 16$. The probability of 4D-symbol $x_1 = [+7, +7, +7, +7]$ resulting from composition C using 1D, 2D and 4D symbol mapping will be

$$P_X^{1D}(x_1) = \frac{1}{16} \cdot \frac{2}{16} \cdot \frac{2}{16} \cdot \frac{2}{16} \cdot \frac{2}{16} = 0.000015,$$

$$P_X^{2D}(x_1) = \frac{1}{16} \cdot \frac{2}{16} \cdot \frac{1}{15} \cdot \frac{2}{16} \cdot \frac{1}{15} = 0.000004,$$

$$P_X^{4D}(x_1) = \frac{1}{16} \cdot \frac{2}{16} \cdot \frac{1}{15} \cdot \frac{0}{14} \cdot \frac{0}{13} = 0.$$

For $x_2 = [+1, +3, +5, +7]$ the probabilities will be

$$P_X^{1D}(x_2) = \frac{1}{16} \cdot \frac{6}{16} \cdot \frac{5}{16} \cdot \frac{3}{16} \cdot \frac{2}{16} = 0.000172 \,,$$

$$P_X^{2D}(x_2) = \frac{1}{16} \cdot \frac{6}{16} \cdot \frac{5}{15} \cdot \frac{3}{16} \cdot \frac{2}{15} = 0.000195 \,,$$

$$P_X^{4D}(x_2) = \frac{1}{16} \cdot \frac{6}{16} \cdot \frac{5}{15} \cdot \frac{3}{14} \cdot \frac{2}{13} = 0.000258 \,.$$

Note that higher-dimensional mapping reduces the probability of having equal amplitudes and increases the probability of having unequal amplitudes in simultaneous quadratures of a 4D-symbol. This leads to less probable high peak power values in the case of higher-dimensional mapping while maintaining the same power efficiency.

A.2   Data Fitting

Data fitting based on the GN-model [28] was performed for each set of numerically simulated and experimental data points, which measure effective SNR and AIR at a specified optical launch power. Note that an approach presented below is generalized for experimental data — i.e. transceiver noise term is included in the fitting model. For numerical simulations transceiver noise term equals zero and therefore can be excluded from the fitting model.

Effective SNR Fitting

Effective SNR is the combination of ASE, nonlinear and transceiver SNR terms. It can be expressed as

$$\begin{aligned}\frac{1}{\text{SNR}_{\text{eff}}} &= \frac{1}{\text{SNR}_{\text{ASE}}} + \frac{1}{\text{SNR}_{\text{NLin}}} + \frac{1}{\text{SNR}_{\text{Tr}}} \\ &= \frac{a}{P} + \frac{b \cdot P^3}{P} + c \,,\end{aligned} \tag{A.11}$$

where SNR_{ASE} is a linear SNR term due to ASE in EDFAs, SNR_{NLin} is a nonlinear SNR term due to nonlinear fiber Kerr nonlinearity (nonlinear noise power is assumed to have cubic dependence on power [28]) and SNR_{Tr}, which is the constant SNR term due to transceiver electrical noise and component imperfections; P is the launch power; a, b, c are the fitting parameters. Effective SNR can be rewritten as follows:

$$\text{SNR}_{\text{eff}} = \frac{P}{a + c \cdot P + b \cdot P^3} \,. \tag{A.12}$$

Initial estimation of fitting parameters is performed as follows: c is estimated according to (A.13) using BtB measurements, a is estimated using launch power sweep measurements neglecting the nonlinear term at low launch power values (A.14), and finally b is estimated using launch power sweep measurements at high launch power values (A.15).

$$c = \frac{1}{\text{SNR}_{\text{eff}}^{\text{BtB}}} - \frac{1}{\text{SNR}_{\text{ASE}}^{\text{BtB}}}$$
$$= \frac{1}{\text{SNR}_{\text{eff}}^{\text{BtB}}} - \frac{BW}{\text{OSNR} \cdot 12.5 \text{ GHz}}, \tag{A.13}$$

$$a = \frac{P}{\text{SNR}_{\text{eff}}^{\text{Lin}}} - c \cdot P, \tag{A.14}$$

$$b = \frac{1}{\text{SNR}_{\text{eff}}^{\text{NLin}} \cdot P^2} - \frac{a}{P^3} - \frac{c}{P^2}, \tag{A.15}$$

where BW is the signal bandwidth.

Refinement of the estimates of fitting parameters may be carried out, for example, using the least squares method [149].

AIR Fitting

For AIR fitting we use a linear mapping with regard to SNR in a logarithmic scale

$$\text{AIR} = k \cdot \log_{10}(\text{SNR}_{\text{eff}}), \tag{A.16}$$

where k is the fitting parameter. For the range of SNR values considered in this work, linear mapping between AIR and SNR (in logarithmic scale) shows very good agreement. However, note that for very low or very high SNR values (when AIR saturates) this approach might be unsuitable.

References

[1] P. J. Winzer and D. T. Neilson, "From scaling disparities to integrated parallelism: A decathlon for a decade," *IEEE/OSA Journal of Lightwave Technology*, vol. 35, no. 5, pp. 1099–1115, 2017.

[2] P. J. Winzer, D. T. Neilson, and A. R. Chraplyvy, "Fiber-optic transmission and networking: The previous 20 and the next 20 years," *Optics Express*, vol. 26, no. 18, pp. 24 190–24 239, Sep. 2018.

[3] Cisco, *Cisco annual internet report (2018–2023)*. [Online]. Available: https://www.cisco.com/c/en/us/solutions/collateral/executive-perspectives/annual-internet-report/white-paper-c11-741490.pdf.

[4] F. Hamaoka, M. Nakamura, S. Okamoto, K. Minoguchi, T. Sasai, A. Matsushita, E. Yamazaki, and Y. Kisaka, "Ultra-wideband WDM transmission in S-, C-, and L-bands using signal power optimization scheme," *IEEE/OSA Journal of Lightwave Technology*, vol. 37, no. 8, pp. 1764–1771, 2019.

[5] J. Renaudier, A. Arnould, A. Ghazisaeidi, D. L. Gac, P. Brindel, E. Awwad, M. Makhsiyan, K. Mekhazni, F. Blache, A. Boutin, L. Letteron, Y. Frignac, N. Fontaine, D. Neilson, and M. Achouche, "Recent advances in 100+nm ultra-wideband fiber-optic transmission systems using semiconductor optical amplifiers," *IEEE/OSA Journal of Lightwave Technology*, vol. 38, no. 5, pp. 1071–1079, 2020.

[6] A. Ferrari, A. Napoli, J. K. Fischer, N. Costa, A. D'Amico, J. Pedro, W. Forysiak, E. Pincemin, A. Lord, A. Stavdas, J. P. F. .-.-. Gimenez, G. Roelkens, N. Calabretta, S. Abrate, B. Sommerkorn-Krombholz, and V. Curri, "Assessment on the achievable throughput of multi-band ITU-T G.652.D fiber transmission systems," *IEEE/OSA Journal of Lightwave Technology*, vol. 38, no. 16, pp. 4279–4291, 2020.

[7] P. J. Winzer, "Energy-efficient optical transport capacity scaling through spatial multiplexing," *IEEE Photonics Technology Letters*, vol. 23, no. 13, pp. 851–853, 2011.

[8] T. Mizuno, H. Takara, K. Shibahara, A. Sano, and Y. Miyamoto, "Dense space division multiplexed transmission over multicore and multimode fiber for long-haul transport systems," *IEEE/OSA Journal of Lightwave Technology*, vol. 34, no. 6, pp. 1484–1493, 2016.

[9] T. Mizuno, H. Takara, A. Sano, and Y. Miyamoto, "Dense space-division multiplexed transmission systems using multi-core and multi-mode fiber," *IEEE/OSA Journal of Lightwave Technology*, vol. 34, no. 2, pp. 582–592, 2016.

[10] *Nortel launches first 10 Gbit/s transmission system in Asia*. [Online]. Available: https://www.hpcwire.com/1997/06/13/nortel-launches-first-10-gbits-transmission-system-in-asia/.

[11] D. A. Fishman, W. A. Thompson, and L. Vallone, "LambdaXtreme® transport system: R&D of a high capacity system for low cost, ultra long-haul DWDM transport," *Bell Labs Technical Journal*, vol. 11, no. 2, pp. 27–53, 2006.

[12] H. Sun, K.-T. Wu, and K. Roberts, "Real-time measurements of a 40 Gb/s coherent system," *Optics Express*, vol. 16, no. 2, pp. 873–879, Jan. 2008.

[13] E. Yamazaki, S. Yamanaka, Y. Kisaka, T. Nakagawa, K. Murata, E. Yoshida, T. Sakano, M. Tomizawa, Y. Miyamoto, S. Matsuoka, J. Matsui, A. Shibayama, J.-i. Abe, Y. Nakamura, H. Noguchi, K. Fukuchi, H. Onaka, K. Fukumitsu, K. Komaki, O. Takeuchi, Y. Sakamoto, H. Nakashima, T. Mizuochi, K. Kubo, Y. Miyata, H. Nishimoto, S. Hirano, and K. Onohara, "Fast optical channel recovery in field demonstration of 100-Gbit/s ethernet over OTN using real-time DSP," *Optics Express*, vol. 19, no. 14, pp. 13 179–13 184, Jul. 2011.

[14] Y. R. Zhou, K. Smith, R. Payne, A. Lord, G. Whalley, T. Bennett, E. Maniloff, S. Alexander, and D. Boymel, "Real-time gridless 800G super-channel transport field trial over 410km using coherent DP-16 QAM," in *Proceedings of Optical Fiber Communications Conference (OFC)*, Optical Society of America, 2014, Tu2B.3.

[15] H. Sun, M. Torbatian, M. Karimi, R. Maher, S. Thomson, M. Tehrani, Y. Gao, A. Kumpera, G. Soliman, A. Kakkar, M. Osman, Z. A. El-Sahn, C. Doggart, W. Hou, S. Sutarwala, Y. Wu, M. R. Chitgarha, V. Lal, H. Tsai, S. Corzine, J. Zhang, J. Osenbach, S. Buggaveeti, Z. Morbi, M. I. Olmedo, I. Leung, X. Xu, P. Samra, V. Dominic, S. Sanders, M. Ziari, A. Napoli, B. Spinnler, K. Wu, and P. Kandappan, "800g DSP ASIC design using probabilistic shaping and digital sub-carrier multiplexing," *IEEE/OSA Journal of Lightwave Technology*, vol. 38, no. 17, pp. 4744–4756, 2020.

[16] W. Forysiak and D. S. Govan, "Progress toward 100-G digital coherent pluggables using InP-based photonics," *IEEE/OSA Journal of Lightwave Technology*, vol. 32, no. 16, pp. 2925–2934, 2014.

[17] R. Mears, L. Reekie, I. Jauncey, and D. Payne, "Low-noise erbium-doped fibre amplifier operating at 1.54 m," *Electronics Letters*, vol. 23, no. 19, pp. 1026–1028, 1987.

[18] E. Desurvire, J. R. Simpson, and P. C. Becker, "High-gain erbium-doped traveling-wave fiber amplifier," *Optics Letters*, vol. 12, no. 11, pp. 888–890, Nov. 1987.

[19] J. Bromage, "Raman amplification for fiber communications systems," *IEEE/OSA Journal of Lightwave Technology*, vol. 22, no. 1, pp. 79–93, 2004.

[20] M. J. O'Mahony, "Semiconductor laser optical amplifiers for use in future fiber systems," *IEEE/OSA Journal of Lightwave Technology*, vol. 6, no. 4, pp. 531–544, 1988.

[21] G. P. Agrawal, *Nonlinear Fiber Optics*. Academic press, 2013.

[22] ——, *Fiber-optic communication systems*. John Wiley & Sons, 2012.

[23] E. Desurvire, *Erbium-Doped Fiber Amplifiers: Principles and Applications*, ser. Wiley Series in Telecommunications and Signal Processing. Wiley, 2002.

[24] A. E. Willner, S. M. R. M. Nezam, L. Yan, Zhongqi Pan, and M. C. Hauer, "Monitoring and control of polarization-related impairments in optical fiber systems," *IEEE/OSA Journal of Lightwave Technology*, vol. 22, no. 1, pp. 106–125, 2004.

[25] P. M. Krummirich and K. Kotten, "Extremely fast (microsecond timescale) polarization changes in high speed long-haul WDM transmission systems," in *Proceedings of Optical Fiber Communication Conference (OFC)*, vol. 2, 2004.

[26] P. M. Krummrich, E. Schmidt, W. Weiershausen, and A. Mattheus, "Field trial results on statistics of fast polarization changes in long haul WDM transmission systems," in *OFC/NFOEC Technical Digest. Optical Fiber Communication Conference, 2005.*, vol. 4, 2005.

[27] P. M. Krummrich, D. Ronnenberg, W. Schairer, D. Wienold, F. Jenau, and M. Herrmann, "Demanding response time requirements on coherent receivers due to fast polarization rotations caused by lightning events," *Optics Express*, vol. 24, no. 11, pp. 12 442–12 457, May 2016.

[28] P. Poggiolini, G. Bosco, A. Carena, V. Curri, Y. Jiang, and F. Forghieri, "The GN-model of fiber non-linear propagation and its applications," *IEEE/OSA Journal of Lightwave Technology*, vol. 32, no. 4, pp. 694–721, 2014.

[29] K. Roberts, M. O'Sullivan, M. Reimer, and M. Hubbard, "Nonlinear mitigation enabling next generation high speed optical transport beyond 100G," in *Proceedings of Optical Fiber Communications Conference (OFC)*, 2019, pp. 1–3.

[30] R. Dar and P. J. Winzer, "Nonlinear interference mitigation: Methods and potential gain," *IEEE/OSA Journal of Lightwave Technology*, vol. 35, no. 4, pp. 903–930, 2017.

[31] O. Vassilieva, "Enabling technologies for fiber nonlinearity mitigation in high capacity transmission systems," in *Proceedings of Optical Fiber Communications Conference (OFC)*, 2018, pp. 1–52.

[32] A. Chen and E. Murphy, *Broadband Optical Modulators: Science, Technology, and Applications*. Taylor & Francis, 2011, ISBN: 9781439825068.

[33] R. A. Griffin, S. K. Jones, N. Whitbread, S. C. Heck, and L. N. Langley, "InP mach–zehnder modulator platform for 10/40/100/200-Gb/s operation," *IEEE Journal of Selected Topics in Quantum Electronics*, vol. 19, no. 6, pp. 158–166, 2013.

[34] D. Vermeulen, R. Aroca, L. Chen, L. Pellach, G. McBrien, and C. Doerr, "Demonstration of silicon photonics push–pull modulators designed for manufacturability," *IEEE Photonics Technology Letters*, vol. 28, no. 10, pp. 1127–1129, 2016.

[35] F. Kish, V. Lal, P. Evans, S. W. Corzine, M. Ziari, T. Butrie, M. Reffle, H. Tsai, A. Dentai, J. Pleumeekers, M. Missey, M. Fisher, S. Murthy, R. Salvatore, P. Samra, S. Demars, N. Kim, A. James, A. Hosseini, P. Studenkov, M. Lauermann, R. Going, M. Lu, J. Zhang, J. Tang, J. Bostak, T. Vallaitis, M. Kuntz, D. Pavinski, A. Karanicolas, B. Behnia, D. Engel, O. Khayam, N. Modi, M. R. Chitgarha, P. Mertz, W. Ko, R. Maher, J. Osenbach, J. T. Rahn, H. Sun, K. Wu, M. Mitchell, and D. Welch, "System-on-chip photonic integrated circuits," *IEEE Journal of Selected Topics in Quantum Electronics*, vol. 24, no. 1, pp. 1–20, 2018.

[36] J. E. Bowers, "Heterogeneous photonic integration on silicon," in *Proceedings of European Conference on Optical Communication (ECOC)*, 2018, pp. 1–3.

[37] OIF, *Implementation agreement for CFP2 - analog coherent optics module*. [Online]. Available: https://www.oiforum.com/wp-content/uploads/2019/01/OIF-CFP2-ACO-01.0.pdf.

[38] ——, *Implementation agreement for CFP2 - digital coherent optics module*. [Online]. Available: https://www.oiforum.com/wp-content/uploads/2019/01/OIF-CFP2-DCO-01.0.pdf.

[39] K. Kikuchi, "Fundamentals of coherent optical fiber communications," *IEEE/OSA Journal of Lightwave Technology*, vol. 34, no. 1, pp. 157–179, 2016.

[40] Y. Painchaud, M. Poulin, M. Morin, and M. Têtu, "Performance of balanced detection in a coherent receiver," *Optics Express*, vol. 17, no. 5, pp. 3659–3672, Mar. 2009.

[41] D. Rafique, A. Napoli, S. Calabro, and B. Spinnler, "Digital preemphasis in optical communication systems: On the DAC requirements for terabit transmission applications," *IEEE/OSA Journal of Lightwave Technology*, vol. 32, no. 19, pp. 3247–3256, 2014.

[42] A. Napoli, M. M. Mezghanni, T. Rahman, D. Rafique, R. Palmer, B. Spinnler, S. Calabrò, C. Castro, M. Kuschnerov, and M. Bohn, "Digital compensation of bandwidth limitations for high-speed DACs and ADCs," *IEEE/OSA Journal of Lightwave Technology*, vol. 34, no. 13, pp. 3053–3064, 2016.

[43] A. Napoli, P. W. Berenguer, T. Rahman, G. Khanna, M. M. Mezghanni, L. Gardian, E. Riccardi, A. C. Piat, S. Calabrò, S. Dris, A. Richter, J. K. Fischer, B. Sommerkorn-Krombholz, and B. Spinnler, "Digital pre-compensation techniques enabling high-capacity bandwidth variable transponders," *Optics Communications*, vol. 409, pp. 52–65, 2018.

[44] J. Zhang, J. Yu, N. Chi, and H.-C. Chien, "Time-domain digital pre-equalization for band-limited signals based on receiver-side adaptive equalizers," *Optics Express*, vol. 22, no. 17, pp. 20 515–20 529, Aug. 2014.

[45] C. Laperle and M. O'Sullivan, "Advances in high-speed DACs, ADCs, and DSP for optical coherent transceivers," *Journal of Lightwave Technology*, vol. 32, no. 4, pp. 629–643, 2014.

[46] S. Varughese, J. Langston, V. A. Thomas, S. Tibuleac, and S. E. Ralph, "Frequency dependent ENoB requirements for M-QAM optical links: An analysis using an improved digital to analog converter model," *IEEE/OSA Journal of Lightwave Technology*, vol. 36, no. 18, pp. 4082–4089, 2018.

[47] R. A. Griffin, N. I. Whitbread, S. K. Jones, S. C. Heck, P. Firth, D. Govan, and T. Goodall, "Inp coherent optical modulator with integrated amplification for high capacity transmission," in *Proceedings of Optical Fiber Communications Conference (OFC)*, 2015, pp. 1–3.

[48] R. Maher, M. Torbatian, S. Koenig, O. Khayam, A. L. Liepvre, P. Samra, P. Day, M. Missey, Z. Wang, A. Nguyen, R. Going, S. Wolf, S. Nowierski, X. Xie, S. Tremblay, M. Ziari, F. Kish, J. Rahn, and P. Kandappan, "Constellation shaping for high symbol rate SNR limited transceivers," in *Next-Generation Optical Communication: Components, Sub-Systems, and Systems VIII*, vol. 10947, 2019, pp. 36–42.

[49] L. Galdino, D. Lavery, Z. Liu, K. Balakier, E. Sillekens, D. Elson, G. Saavedra, R. I. Killey, and P. Bayvel, "The trade-off between transceiver capacity and symbol rate," in *Proceedings of Optical Fiber Communications Conference (OFC)*, 2018, pp. 1–3.

[50] Cheng-Po Liang, Je-Hong Jong, W. E. Stark, and J. R. East, "Nonlinear amplifier effects in communications systems," *IEEE Transactions on Microwave Theory and Techniques*, vol. 47, no. 8, pp. 1461–1466, 1999.

[51] M. Jacques, A. Samani, D. Patel, E. El-Fiky, M. Morsy-Osman, T. Hoang, M. G. Saber, L. Xu, J. Sonkoly, M. Ayliffe, and D. V. Plant, "Modulator material impact on chirp, DSP, and performance in coherent digital links: Comparison of the lithium niobate, indium phosphide, and silicon platforms," *Optics Express*, vol. 26, no. 17, pp. 22 471–22 490, Aug. 2018.

[52] P. W. Berenguer, M. Nölle, L. Molle, T. Raman, A. Napoli, C. Schubert, and J. K. Fischer, "Nonlinear digital pre-distortion of transmitter components," *IEEE/OSA Journal of Lightwave Technology*, vol. 34, no. 8, pp. 1739–1745, 2016.

[53] I. Fatadin, S. J. Savory, and D. Ives, "Compensation of quadrature imbalance in an optical QPSK coherent receiver," *IEEE Photonics Technology Letters*, vol. 20, no. 20, pp. 1733–1735, 2008.

[54] P. J. Winzer and R. Essiambre, "Advanced optical modulation formats," *Proceedings of the IEEE*, vol. 94, no. 5, pp. 952–985, 2006.

[55] G. Liga, A. Alvarado, E. Agrell, and P. Bayvel, "Information rates of next-generation long-haul optical fiber systems using coded modulation," *IEEE/OSA Journal of Lightwave Technology*, vol. 35, no. 1, pp. 113–123, 2017.

[56] U. Wachsmann, R. F. H. Fischer, and J. B. Huber, "Multilevel codes: Theoretical concepts and practical design rules," *IEEE Transactions on Information Theory*, vol. 45, no. 5, pp. 1361–1391, 1999.

[57] G. Ungerboeck, "Channel coding with multilevel/phase signals," *IEEE Transactions on Information Theory*, vol. 28, no. 1, pp. 55–67, 1982.

[58] L. Szczecinski and A. Alvarado, *Bit-interleaved coded modulation: fundamentals, analysis and design*. John Wiley & Sons, 2015.

[59] J. G. Proakis and M. Salehi, *Digital communications, 5th edition*. New York,: McGraw-Hill, 2007.

[60] ITU, *Rec. G.975.1: Forward error correction for high bit-rate DWDM submarine systems*, 2004. [Online]. Available: https://www.itu.int/rec/T-REC-G.975.1-200402-I/en.

[61] OIF, *100G forward error correction white paper*, 2010. [Online]. Available: https://www.oiforum.com/wp-content/uploads/2019/01/OIF_FEC_100G-01.0.pdf.

[62] T. Richardson, "Error floors of LDPC codes," in *Proceedings of the 41st Annual Conference on Communication, Control and Computing*, vol. 41, 2003, pp. 1426–1435.

[63] D. S. Millar, T. Fehenberger, T. Koike-Akino, K. Kojima, and K. Parsons, "Coded modulation for next-generation optical communications," in *Proceedings of Optical Fiber Communications Conference (OFC)*, 2018, pp. 1–3.

[64] F. Jardel, T. A. Eriksson, C. Méasson, A. Ghazisaeidi, F. Buchali, W. Idler, and J. J. Boutros, "Exploring and experimenting with shaping designs for next-generation optical communications," *IEEE/OSA Journal of Lightwave Technology*, vol. 36, no. 22, pp. 5298–5308, 2018.

[65] Feng-Wen Sun and H. C. A. van Tilborg, "Approaching capacity by equiprobable signaling on the gaussian channel," *IEEE Transactions on Information Theory*, vol. 39, no. 5, pp. 1714–1716, 1993.

[66] B. Chen, C. Okonkwo, H. Hafermann, and A. Alvarado, "Increasing achievable information rates via geometric shaping," in *Proceedings of European Conference on Optical Communication (ECOC)*, 2018, pp. 1–3.

[67] F. R. Kschischang and S. Pasupathy, "Optimal nonuniform signaling for Gaussian channels," *IEEE Transactions on Information Theory*, vol. 39, no. 3, pp. 913–929, 1993.

[68] G. Böcherer, F. Steiner, and P. Schulte, "Bandwidth efficient and rate-matched low-density parity-check coded modulation," *IEEE Transactions on Communications*, vol. 63, no. 12, pp. 4651–4665, 2015.

[69] M. Mazurczyk, "Spectral shaping in long haul optical coherent systems with high spectral efficiency," *IEEE/OSA Journal of Lightwave Technology*, vol. 32, no. 16, pp. 2915–2924, 2014.

[70] R. Schmogrow, S. Ben-Ezra, P. C. Schindler, B. Nebendahl, C. Koos, W. Freude, and J. Leuthold, "Pulse-shaping with digital, electrical, and optical filters — a comparison," *IEEE/OSA Journal of Lightwave Technology*, vol. 31, no. 15, pp. 2570–2577, 2013.

[71] M. S. Faruk and S. J. Savory, "Digital signal processing for coherent transceivers employing multilevel formats," *IEEE/OSA Journal of Lightwave Technology*, vol. 35, no. 5, pp. 1125–1141, 2017.

[72] S. Haykin, "Adaptive filter theory," *Englewood Cliffs, NJ, Prentice-Hall*, 1986.

[73] A. Eghbali, H. Johansson, O. Gustafsson, and S. J. Savory, "Optimal least-squares FIR digital filters for compensation of chromatic dispersion in digital coherent optical receivers," *IEEE/OSA Journal of Lightwave Technology*, vol. 32, no. 8, pp. 1449–1456, 2014.

[74] F. Gardner, "A BPSK/QPSK timing-error detector for sampled receivers," *IEEE Transactions on Communications*, vol. 34, no. 5, pp. 423–429, 1986.

[75] X. Zhou, "Efficient clock and carrier recovery algorithms for single-carrier coherent optical systems: A systematic review on challenges and recent progress," *IEEE Signal Processing Magazine*, vol. 31, no. 2, pp. 35–45, 2014.

[76] F. M. Gardner, "Interpolation in digital modems. I. fundamentals," *IEEE Transactions on Communications*, vol. 41, no. 3, pp. 501–507, 1993.

[77] J. Vesma and T. Saramaki, "Optimization and efficient implementation of FIR filters with adjustable fractional delay," in *IEEE International Symposium on Circuits and Systems (ISCAS)*, vol. 4, 1997, pp. 2256–2259.

[78] E. Ip and J. M. Kahn, "Feedforward carrier recovery for coherent optical communications," *IEEE/OSA Journal of Lightwave Technology*, vol. 25, no. 9, pp. 2675–2692, 2007.

[79] M. Selmi, Y. Jaouen, and P. Ciblat, "Accurate digital frequency offset estimator for coherent PolMux QAM transmission systems," in *Proceedings of European Conference on Optical Communication (ECOC)*, 2009, pp. 1–2.

[80] F. A. Barbosa, S. M. Rossi, and D. A. A. Mello, "Phase and frequency recovery algorithms for probabilistically shaped transmission," *IEEE/OSA Journal of Lightwave Technology*, vol. 38, no. 7, pp. 1827–1835, 2020.

[81] D. Zhao, L. Xi, X. Tang, W. Zhang, Y. Qiao, and X. Zhang, "Digital pilot aided carrier frequency offset estimation for coherent optical transmission systems," *Opt. Express*, vol. 23, no. 19, pp. 24 822–24 832, Sep. 2015.

[82] T. Pfau, S. Hoffmann, and R. Noe, "Hardware-efficient coherent digital receiver concept with feedforward carrier recovery for M-QAM constellations," *IEEE/OSA Journal of Lightwave Technology*, vol. 27, no. 8, pp. 989–999, 2009.

[83] X. Li, Y. Cao, S. Yu, W. Gu, and Y. Ji, "A simplified feedforward carrier recovery algorithm for coherent optical QAM system," *IEEE/OSA Journal of Lightwave Technology*, vol. 29, no. 5, pp. 801–807, 2011.

[84] A. Alvarado, E. Agrell, D. Lavery, R. Maher, and P. Bayvel, "Replacing the soft-decision FEC limit paradigm in the design of optical communication systems*," *IEEE/OSA Journal of Lightwave Technology*, vol. 34, no. 2, pp. 707–721, 2016.

[85] A. Alvarado, T. Fehenberger, B. Chen, and F. M. J. Willems, "Achievable information rates for fiber optics: Applications and computations," *IEEE/OSA Journal of Lightwave Technology*, vol. 36, no. 2, pp. 424–439, 2018.

[86] T. M. Cover, *Elements of information theory*. John Wiley & Sons, 1999.

[87] M. Paskov, D. Lavery, and S. J. Savory, "Blind equalization of receiver in-phase/quadrature skew in the presence of nyquist filtering," *IEEE Photonics Technology Letters*, vol. 25, no. 24, pp. 2446–2449, 2013.

[88] M. S. Faruk and K. Kikuchi, "Compensation for in-phase/quadrature imbalance in coherent-receiver front end for optical quadrature amplitude modulation," *IEEE Photonics Journal*, vol. 5, no. 2, pp. 7 800 110–7 800 110, 2013.

[89] E. P. da Silva and D. Zibar, "Widely linear equalization for IQ imbalance and skew compensation in optical coherent receivers," *IEEE/OSA Journal of Lightwave Technology*, vol. 34, no. 15, pp. 3577–3586, 2016.

[90] B. T. Reyes, V. Gopinathan, P. S. Mandolesi, and M. R. Hueda, "Joint sampling-time error and channel skew calibration of time-interleaved ADC in multichannel fiber optic receivers," in *Proceedings of IEEE International Symposium on Circuits and Systems (ISCAS)*, 2012, pp. 2981–2984.

[91] N. Stojanovic and X. Changsong, "An efficient method for skew estimation and compensation in coherent receivers," *IEEE Photonics Technology Letters*, vol. 28, no. 4, pp. 489–492, 2016.

[92] Y. Yue, B. Zhang, Q. Wang, R. Lofland, J. O'Neil, and J. Anderson, "Detection and alignment of dual-polarization optical quadrature amplitude transmitter IQ and XY skews using reconfigurable interference," *Opt. Express*, vol. 24, no. 6, pp. 6719–6734, Mar. 2016.

[93] J. C. M. Diniz, F. D. Ros, R. T. Jones, and D. Zibar, "Time skew estimator for dual-polarization QAM transmitters," in *Proceedings of European Conference on Optical Communication (ECOC)*, 2017, pp. 1–3.

[94] J. C. M. Diniz, F. Da Ros, E. P. da Silva, R. T. Jones, and D. Zibar, "Optimization of DP-M-QAM transmitter using cooperative coevolutionary genetic algorithm," *IEEE/OSA Journal of Lightwave Technology*, vol. 36, no. 12, pp. 2450–2462, 2018.

[95] G. Khanna, B. Spinnler, S. Calabrò, E. De Man, and N. Hanik, "A robust adaptive pre-distortion method for optical communication transmitters," *IEEE Photonics Technology Letters*, vol. 28, no. 7, pp. 752–755, 2016.

[96] C. R. S. Fludger, T. Duthel, P. Hermann, and T. Kupfer, "Low cost transmitter self-calibration of time delay and frequency response for high baud-rate QAM transceivers," in *Proceedings of Optical Fiber Communications Conference (OFC)*, 2017, pp. 1–3.

[97] C. R. S. Fludger and T. Kupfer, "Transmitter impairment mitigation and monitoring for high baud-rate, high order modulation systems," in *Proceedings of European Conference on Optical Communication (ECOC)*, 2016, pp. 1–3.

[98] Y. Yue, B. Zhang, Q. Wang, R. Lofland, J. O'Neil, and J. Anderson, "Detection and alignment of dual-polarization optical quadrature amplitude transmitter IQ and XY skews using reconfigurable interference," *Optics Express*, vol. 24, no. 6, pp. 6719–6734, Mar. 2016.

[99] J. C. M. Diniz, F. Da Ros, E. P. da Silva, R. T. Jones, and D. Zibar, "Optimization of DP-M-QAM transmitter using cooperative coevolutionary genetic algorithm," *IEEE/OSA Journal of Lightwave Technology*, vol. 36, no. 12, pp. 2450–2462, 2018.

[100] T.-H. Nguyen, P. Scalart, M. Gay, L. Bramerie, O. Sentieys, J.-C. Simon, C. Peucheret, and M. Joindot, "Blind transmitter iq imbalance compensation in M-QAM optical coherent systems," *Journal of Optical Communications and Networking*, vol. 9, no. 9, pp. D42–D50, Sep. 2017.

[101] J. Liang, Y. Fan, Z. Tao, X. Su, and H. Nakashima, "Transceiver imbalances compensation and monitoring by receiver DSP," *IEEE/OSA Journal of Lightwave Technology*, pp. 1–1, 2019.

[102] W. Yao, G. Gilardi, N. Calabretta, M. K. Smit, and M. J. Wale, "Experimental and numerical study of electrical crosstalk in photonic-integrated circuits," *IEEE/OSA Journal of Lightwave Technology*, vol. 33, no. 4, pp. 934–942, 2015.

[103] L. Jiang, X. Chen, K. Kim, G. de Valicourt, Z. R. Huang, and P. Dong, "Electro-optic crosstalk in parallel silicon photonic mach-zehnder modulators," *IEEE/OSA Journal of Lightwave Technology*, vol. 36, no. 9, pp. 1713–1720, 2018.

[104] X. Chen, P. Dong, S. Chandrasekhar, K. Kim, B. Li, H. Chen, A. Adamiecki, A. Gnauck, and P. Winzer, "Characterization and digital pre-compensation of electro-optic crosstalk in silicon photonics I/Q modulators," in *Proceedings of European Conference on Optical Communication (ECOC)*, 2016, pp. 1–3.

[105] J. Cho, X. Chen, S. Chandrasekhar, G. Raybon, R. Dar, L. Schmalen, E. Burrows, A. Adamiecki, S. Corteselli, Y. Pan, D. Correa, B. McKay, S. Zsigmond, P. Winzer, and S. Grubb, "Trans-atlantic field trial using probabilistically shaped 64-QAM at high spectral efficiencies and single-carrier real-time 250-Gb/s 16-QAM," in *Proceedings of Optical Fiber Communications Conference (OFC)*, Los Angeles, CA, USA, 2017.

[106] J. Li, A. Zhang, C. Zhang, X. Huo, Q. Yang, J. Wang, J. Wang, W. Qu, Y. Wang, J. Zhang, M. Si, Z. Zhang, and X. Liu, "Field trial of probabilistic-shaping-programmable real-time 200-Gb/s coherent transceivers in an intelligent core optical network," in *Proceedings of Asia Communications and Photonics Conference (ACP)*, Guangzhou, China, 2018.

[107] F. Buchali, F. Steiner, G. Böcherer, L. Schmalen, P. Schulte, and W. Idler, "Rate adaptation and reach increase by probabilistically shaped 64-QAM: An experimental demonstration," *IEEE/OSA Journal of Lightwave Technology*, vol. 34, no. 7, pp. 1599–1609, 2016.

[108] T. Fehenberger, D. S. Millar, T. Koike-Akino, K. Kojima, and K. Parsons, "Multiset-partition distribution matching," *IEEE Transactions on Communications*, vol. 67, no. 3, pp. 1885–1893, 2019.

[109] Y. C. Gültekin, W. J. van Houtum, S. Şerbetli, and F. M. J. Willems, "Constellation shaping for IEEE 802.11," in *Proceedings of IEEE PIMRC*, Montreal, QC, Canada, 2017.

[110] Y. Koganei, K. Sugitani, H. Nakashima, and T. Hoshida, "Optimum bit-level distribution matching with at most O(N3) implementation complexity," in *Proceedings of Optical Fiber Communications Conference (OFC)*, San Diego, CA, USA, 2019.

[111] T. Yoshida, M. Karlsson, and E. Agrell, "Hierarchical distribution matching for probabilistically shaped coded modulation," *IEEE/OSA Journal of Lightwave Technology*, vol. 37, no. 6, pp. 1579–1589, 2019.

[112] T. Fehenberger and A. Alvarado, *Analysis and optimisation of distribution matching for the nonlinear fibre channel*, arXiv:1907.02846, 2019. arXiv: 1907.02846 [eess.SP].

[113] E. Agrell and M. Karlsson, "Power-efficient modulation formats in coherent transmission systems," *IEEE/OSA Journal of Lightwave Technology*, vol. 27, no. 22, pp. 5115–5126, 2009.

[114] A. Alvarado and E. Agrell, "Four-dimensional coded modulation with bit-wise decoders for future optical communications," *IEEE/OSA Journal of Lightwave Technology*, vol. 33, no. 10, pp. 1993–2003, 2015.

[115] D. S. Millar, T. Koike-Akino, S. Ö. Arik, K. Kojima, K. Parsons, T. Yoshida, and T. Sugihara, "High-dimensional modulation for coherent optical communications systems," *Optics Express*, vol. 22, no. 7, pp. 8798–8812, Apr. 2014.

[116] D. S. Millar, T. Koike-Akino, K. Kojima, and K. Parsons, "Multidimensional modulation for next-generation transmission systems," in *Next-Generation Optical Communication: Components, Sub-Systems, and Systems VI*, G. Li and X. Zhou, Eds., International Society for Optics and Photonics, vol. 10130, SPIE, 2017, pp. 85–90.

[117] K. Kojima, T. Yoshida, T. Koike-Akino, D. S. Millar, K. Parsons, M. Pajovic, and V. Arlunno, "Nonlinearity-tolerant four-dimensional 2A8PSK family for 5–7 bits/symbol spectral efficiency," *IEEE/OSA Journal of Lightwave Technology*, vol. 35, no. 8, pp. 1383–1391, 2017.

[118] A. D. Shiner, M. Reimer, A. Borowiec, S. O. Gharan, J. Gaudette, P. Mehta, D. Charlton, K. Roberts, and M. O'Sullivan, "Demonstration of an 8-dimensional modulation format with reduced inter-channel nonlinearities in a polarization multiplexed coherent system," *Optics Express*, vol. 22, no. 17, pp. 20 366–20 374, Aug. 2014.

[119] K. Kojima, K. Parsons, T. Koike-Akino, and D. S. Millar, "Mapping options of 4D constant modulus format for multi-subcarrier modulation," in *Proceeding of Conference on Lasers and Electro-Optics (CLEO)*, 2018, pp. 1–2.

[120] R. Laroia, N. Farvardin, and S. A. Tretter, "On optimal shaping of multidimensional constellations," *IEEE Transactions on Information Theory*, vol. 40, no. 4, pp. 1044–1056, 1994.

[121] J. Cho, X. Chen, S. Chandrasekhar, and P. Winzer, "On line rates, information rates, and spectral efficiencies in probabilistically shaped QAM systems," *Optics Express*, vol. 26, no. 8, pp. 9784–9791, Apr. 2018.

[122] P. Schulte and G. Böcherer, "Constant composition distribution matching," *IEEE Transactions on Information Theory*, vol. 62, no. 1, pp. 430–434, 2016.

[123] D. S. Millar, T. Fehenberger, T. Koike-Akino, K. Kojima, and K. Parsons, "Distribution matching for high spectral efficiency optical communication with multiset partitions," *IEEE/OSA Journal of Lightwave Technology*, vol. 37, no. 2, pp. 517–523, 2019.

[124] F. Steiner, P. Schulte, and G. Bocherer, "Approaching waterfilling capacity of parallel channels by higher order modulation and probabilistic amplitude shaping," in *Proceedings of Annual Conference on Information Sciences and Systems (CISS)*, 2018, pp. 1–6.

[125] T. Yoshida, M. Karlsson, and E. Agrell, "Hierarchical distribution matching for probabilistically shaped coded modulation," *IEEE/OSA Journal of Lightwave Technology*, vol. 37, no. 6, pp. 1579–1589, 2019.

[126] T. Fehenberger, D. S. Millar, T. Koike-Akino, K. Kojima, and K. Parsons, "Parallel-amplitude architecture and subset ranking for fast distribution matching," *IEEE Transactions on Communications*, vol. 68, no. 4, pp. 1981–1990, 2020.

[127] R. F. H. Fischer, *Precoding and signal shaping for digital transmission*. New York, New York, USA: John Wiley & Sons, 2005.

[128] A. K. Khandani and P. Kabal, "Shaping multidimensional signal spaces. I. optimum shaping, shell mapping," *IEEE Transactions on Information Theory*, vol. 39, no. 6, pp. 1799–1808, 1993.

[129] P. Schulte and F. Steiner, "Divergence-optimal fixed-to-fixed length distribution matching with shell mapping," *IEEE Wireless Communications Letters*, vol. 8, no. 2, pp. 620–623, 2019.

[130] Y. C. Gültekin, W. J. van Houtum, A. G. C. Koppelaar, and F. M. J. Willems, "Enumerative sphere shaping for wireless communications with short packets," *IEEE Transactions on Wireless Communications*, vol. 19, no. 2, pp. 1098–1112, 2020.

[131] A. Amari, S. Goossens, Y. C. Gültekin, O. Vassilieva, I. Kim, T. Ikeuchi, C. M. Okonkwo, F. M. J. Willems, and A. Alvarado, "Introducing enumerative sphere shaping for optical communication systems with short blocklengths," *IEEE/OSA Journal of Lightwave Technology*, vol. 37, no. 23, pp. 5926–5936, 2019.

[132] D. S. Millar, T. Fehenberger, T. Yoshida, T. Koike-Akino, K. Kojima, N. Suzuki, and K. Parsons, "Huffman coded sphere shaping with short length and reduced complexity," in *Proceedings of European Conference on Optical Communications (ECOC)*, Dublin, Ireland, 2019.

[133] T. Fehenberger, D. S. Millar, T. Koike-Akino, K. Kojima, K. Parsons, and H. Griesser, "Huffman-coded sphere shaping and distribution matching algorithms via lookup tables," *IEEE/OSA Journal of Lightwave Technology*, vol. 38, no. 10, pp. 2826–2834, 2020.

[134] T. Fehenberger, A. Alvarado, G. Böcherer, and N. Hanik, "On probabilistic shaping of quadrature amplitude modulation for the nonlinear fiber channel," *IEEE/OSA Journal of Lightwave Technology*, vol. 34, no. 21, pp. 5063–5073, 2016.

[135] J. Renner, T. Fehenberger, M. P. Yankov, F. Da Ros, S. Forchhammer, G. Böcherer, and N. Hanik, "Experimental comparison of probabilistic shaping methods for un-repeated fiber transmission," *IEEE/OSA Journal of Lightwave Technology*, vol. 35, no. 22, pp. 4871–4879, 2017.

[136] T. Fehenberger, H. Griesser, and J.-P. Elbers, "Mitigating fiber nonlinearities by short-length probabilistic shaping," in *Proceedings of Optical Fiber Communications Conference (OFC)*, San Diego, CA, USA, 2020.

[137] T. Fehenberger, D. S. Millar, T. Koike-Akino, K. Kojima, K. Parsons, and H. Griesser, "Analysis of nonlinear fiber interactions for finite-length constant-composition sequences," *IEEE/OSA Journal of Lightwave Technology*, vol. 38, no. 2, pp. 457–465, 2020.

[138] S. Goossens, S. Van der Heide, M. Van den Hout, A. Amari, Y. C. Gültekin, O. Vassilieva, I. Kim, T. Ikeuchi, F. M. J. Willems, A. Alvarado, and C. Okonkwo, "First experimental demonstration of probabilistic enumerative sphere shaping in optical fiber communications," in *Proceedings of Opto-Electronics and Communications Conference (OECC) and International Conference on Photonics in Switching and Computing (PSC)*, Fukuoka, Japan, 2019.

[139] R. Dar, M. Feder, A. Mecozzi, and M. Shtaif, "On shaping gain in the nonlinear fiber-optic channel," in *IEEE International Symposium on Information Theory*, 2014, pp. 2794–2798.

[140] O. Geller, R. Dar, M. Feder, and M. Shtaif, "A shaping algorithm for mitigating inter-channel nonlinear phase-noise in nonlinear fiber systems," *IEEE/OSA Journal of Lightwave Technology*, vol. 34, no. 16, pp. 3884–3889, 2016.

[141] P. Schulte, F. Steiner, and G. Bocherer, "Four dimensional probabilistic shaping for fiber-optic communication," in *Proceedings of Advanced Photonics 2017 (IPR, NOMA, Sensors, Networks, SPPCom, PS)*, Optical Society of America, 2017, SpM2F.5.

[142] F. Steiner, F. Da Ros, M. P. Yankov, G. Böcherer, P. Schulte, S. Forchhammer, and G. Kramer, "Experimental verification of rate flexibility and probabilistic shaping by 4D signaling," in *Proceedings of Optical Fiber Communications Conference (OFC)*, 2018, pp. 1–3.

[143] O. V. Sinkin, R. Holzlohner, J. Zweck, and C. R. Menyuk, "Optimization of the split-step Fourier method in modeling optical-fiber communications systems," *IEEE/OSA Journal of Lightwave Technology*, vol. 21, no. 1, pp. 61–68, 2003.

[144] Q. Zhang and M. I. Hayee, "Symmetrized split-step Fourier scheme to control global simulation accuracy in fiber-optic communication systems," *IEEE/OSA Journal of Lightwave Technology*, vol. 26, no. 2, pp. 302–316, 2008.

[145] P. K. A. Wai and C. R. Menyak, "Polarization mode dispersion, decorrelation, and diffusion in optical fibers with randomly varying birefringence," *IEEE/OSA Journal of Lightwave Technology*, vol. 14, no. 2, pp. 148–157, 1996.

[146] D. Marcuse, C. R. Manyuk, and P. K. A. Wai, "Application of the Manakov-PMD equation to studies of signal propagation in optical fibers with randomly varying birefringence," *IEEE/OSA Journal of Lightwave Technology*, vol. 15, no. 9, pp. 1735–1746, 1997.

[147] T. A. Eriksson, T. Fehenberger, P. A. Andrekson, M. Karlsson, N. Hanik, and E. Agrell, "Impact of 4D channel distribution on the achievable rates in coherent optical communication experiments," *IEEE/OSA Journal of Lightwave Technology*, vol. 34, no. 9, pp. 2256–2266, 2016.

[148] D. S. Millar, R. Maher, D. Lavery, T. Koike-Akino, M. Pajovic, A. Alvarado, M. Paskov, K. Kojima, K. Parsons, B. C. Thomsen, S. J. Savory, and P. Bayvel, "Design of a 1 Tb/s superchannel coherent receiver," *IEEE/OSA Journal of Lightwave Technology*, vol. 34, no. 6, pp. 1453–1463, 2016.

[149] R. W. Hamming, *Numerical Methods for Scientists and Engineers*. Dover Press, 1986.